



Universität Potsdam

Institut für Erd- und Umweltwissenschaften

Master Thesis

# Source Array and Receiver Array analysis of Vogtland/ West Bohemia earthquake clusters

Submitted by
Gesa Maria Petersen

1. Supervisor: apl. Prof. Frank Krüger
2. Supervisor: Dr. Matthias Ohrnberger

Submission date: October 2, 2017

Published online at the
Institutional Repository of the University of Potsdam:
URN urn:nbn:de:kobv:517-opus4-406671
http://nbn-resolving.de/urn:nbn:de:kobv:517-opus4-406671

# Contents


**1 Zusammenfassung in deutscher Sprache** **4**

**2 Introduction and Motivation** **6**

**3 Area of research: Vogtland/ West Bohemia** **7**

3.1 Geography and tectonics . . . . . 7

3.2 Seismic structure of the crust . . . . . 9

3.3 Observed geological and seismic activity . . . . . 9

3.4 Earthquakes swarms at the Nový Kostel focal zone: Triggering processes and tectonic implications . . . . . 11

**4 Theoretical background** **14**

4.1 Array Seismology . . . . . 14

4.2 Reciprocity of the Green's function . . . . . 15

4.3 Source arrays . . . . . 19

4.4 Double-Beam method . . . . . 21

**5 Set-up of source and receiver array** **23**

5.1 The receiver array at Rohrbach . . . . . 23

5.2 Earthquake data and event catalogue . . . . . 24

5.3 Source array . . . . . 25

5.3.1 Constructing a source array . . . . . 25

5.3.2 Empirical source array transfer function from synthetic data . . . . 28

**6 Development of a source array beam forming method in time domain** **32**

6.1 Development of a first beam forming algorithm . . . . . 32

6.2 Tests with synthetic data . . . . . 34

6.2.1 Preparing synthetic data . . . . . 34

6.2.2 Testing with linear arrays . . . . . 35

6.3 Adaptation of beam forming code to recorded source array data . . . . . 37

6.4 Adaption of beam forming code to receiver array . . . . . 38

**7 Two methods for the determination of conversion locations** **40**

7.1 Analytical determination of conversion locations from beam forming results 40

7.2 Grid search for conversion locations . . . . . 45

**8 Evaluation of prerequisites of source array beam forming** **48**

8.1 Waveform similarity - comparison between source and receiver array . . . . 48

8.2 Origin times and locations . . . 51
8.3 Homogeneous velocities within the source array . . . 53

**9 Source array analysis: Results and Interpretations 55**
9.1 Comparison of theoretical and observed P arrival times . . . 55
9.2 Sensitivity of source array beam forming towards location errors . . . 57
9.3 Source array beam forming results before and after alignment relative to P phase amplitude maxima . . . 58
9.3.1 Beam forming dependent on origin times . . . 59
9.3.2 Improvements of beam forming using P alignment . . . 61
9.4 Interpretation of phases detected with source array beam forming . . . 66
9.5 Beam forming results of deeper events . . . 70
9.6 Comparison of Rohrbach stations based on the source array records . . . 74

**10 Receiver array analysis: Results 76**
10.1 Direct P phase: Comparison of observed and theoretical travel paths . . . 76
10.2 Other phases obtained using beam forming . . . 76

**11 Discussion and concluding remarks 78**
11.1 Summary . . . 78
11.2 Advantages and shortcomings of applied source array techniques . . . 80
11.3 Conclusion and small outlook . . . 81

**Acknowledgements 83**

**Selbstständigkeitserklärung 84**

**References 85**

**Appendix 90**
Supplementary material on CD . . . 90
Python code . . . 90
Source array - residuals of obs. and theor. arrival times . . . 91
Cross-correlation analysis for different frequency ranges . . . 94
Beam forming results . . . 97
Source array . . . 97
Receiver array . . . 101
Poster AG Seismologie . . . 107

# 1 Zusammenfassung in deutscher Sprache

Die Region Vogtland/ West Böhmen im Grenzgebiet zwischen Deutschland und Tschechien ist bekannt für ihre geologische Aktivität. Holozäner Vulkanismus, Gasaustritte an Mofetten und Quellen und wiederkehrende Erdbebenschwärme sind Ausdruck geodynamischer Prozesse im Untergrund (e.g. Fischer et al. [2010]). Wochenlange Erdbebenschwärme, wie bspw. in den Jahren 2008/2009 oder auch ganz aktuell im Frühjahr/Sommer 2017, bestehen aus tausenden kleineren Erdbeben, wobei am 21. Dezember 1985 eine Maximalmagnitude von $M_L$ 4.6 erreicht wurde [Fischer et al., 2014]. Während des Erdbebenschwarms 2008/2009 in Nový Kostel installierte die Universität Potsdam ein temporäres Array mit 11 LE3D-5s Sensoren in Rohrbach, in einer Epizentraldistanz von etwa 10 km und mit einer Aperatur von etwa 0.75 km. Die Daten dieses Arrays wurden im Rahmen der vorliegenden Masterarbeit durch Quell- und Empfängerarray-Methoden untersucht. Dabei lag der Fokus auf der methodischen Entwicklung und Evaluierung der Nutzbarkeit von Quellarrays bestehend aus kleinen Lokalbeben zur Strukturabbildung.

Quellarrays sind örtliche Cluster von Erdbeben, die von einer Empfängerstation aufgezeichnet werden. Wegen der Reziprozität der Green'schen Funktion können diese in ähnlicher Weise genutzt werden wie Empfängerarrays, bei denen mehrere Stationen ein einzelnes Beben aufzeichnen. *Beam forming* ist eine Standard-Methode der Seismologie, bei der die Seismogramme mehrerer Stationen (bei Quellarrays mehrerer Erdbeben) zeitlich verschoben werden und dann aufsummiert werden, um kohärente Phasen zu verstärken und Rauschen zu unterdrücken. Dabei werden Verschiebungszeiten für unterschiedliche Richtungen und Geschwindigkeiten berechnet. Aus den maximalen aufsummierten Energien einer Phase kann auf die Richtung und Geschwindigkeit dieser Phase zurück geschlossen werden. Voraussetzung für die Verwendung von Quellarrays sind genau bestimmte Herdzeiten, Lokationen und ähnliche Wellenformen.

Aus den Daten des 2008/2009 Erdbebenschwarm wurde ein Quellarray aus 22 Erdbeben aufgebaut. Obwohl eine möglichst gleichmäßige räumliche Verteilung angestrebt wurde, ist die Ost-West Ausdehnung im Vergleich zur Nord-Süd- und Tiefenausdehnung gering, da die Beben entlang einer Bruchfläche auftreten. Die Kreuzkorrelationskoeffizienten aller Beben des Quellarrays, aufgezeichnet an einer einzelnen Station, sind in der Regel höher als für einzelne Ereignisse, die an allen Stationen des Empfängerarrays aufgezeichnet wurden. Dies zeigt, dass Quellarrays sich aufgrund ihrer ähnlichen Wellenformen im Vogtland sehr gut für arrayseismologische Untersuchungen des Untergrunds eignen.

Nach verschiedenen synthetischen Tests wurde *beam forming* mit Quell- und Empfängerarrays ausgeführt. Während die theoretische Richtung der direkten P-Welle im Falle der Quellarray-Aufzeichnungen gut übereinstimmt, wird eine Empfängerarray-Missweisung von 15 ° bis 25 ° beobachtet. Im Quellarray sind die direkten P und S Wellen eindeutig

auf den drei Komponenten bestimmbar. Etwa 0.15 s nach der direkten P Phase ist auf den Ost-Komponenten der Quellarray-Aufzeichnungen eine PS Phase zu sehen. In einigen Daten ist zusätzlich eine Phase vor der direkten S Welle zu sehen, die als SP Phase interpretiert wird. Nach Laufzeitbetrachtung geschieht die Konversion in etwa 0.6-0.9 km Tiefe. Ein zweites Quellarray, bestehend aus 12 tieferen Beben wurde zusätzlich analysiert, um eine nach ca. 0.85 s ausschließlich auf den Aufzeichnungen tieferer Beben auftretende Strukturphase zu deuten. Zusätzlich zum *beam forming* wurden zwei Lokalisierungsmethoden von Reflexionen und Konversionen für einfach reflektierte/konvertierte Phasen entwickelt und zur Auswertung verwendet. Während die erste, analytische Methode eine homogene Geschwindigkeit entlang des Laufwegs annimmt, wird in der zweiten Methode eine 3-D-Rastersuche ausgeführt, in der ein 1-D-Geschwindigkeitsmodell verwendet wird.

Zusammenfassend beschreibt vorliegende Arbeit Voraussetzungen, Arbeitsschritte und Ansätze zur Nutzung und Auswertung von Quellarrays bestehend aus Lokalbeben ($M_c \leq 1.7$). Zusätzlich wurden Empfängerarray-Daten betrachtet. Auf Grund der eindeutigen *beam forming* Ergebnisse und der hohen Ähnlichkeit der Wellenformen der Erdbeben, die für das Quellarray genutzt wurden, bieten Quellarrays bestehend aus Mikrobeben aus dem untersuchten Gebiet gute Möglichkeiten zur Untersuchung von Krustenstrukturen.

# 2 Introduction and Motivation

The Vogtland, located at the border region between the Czech Republic and Germany, is known for Holocene volcanism, gas and fluid emissions as well as for reoccurring earthquake swarms, pointing towards a high geodynamic activity. The occurrence of thousands of densely spaced, small earthquakes within weeks or months bear the possibility of using these events as source arrays for structural investigations of the upper crust. In contrast to receiver arrays, source array data is cheap to obtain (only one seismic station is needed) and subsurface effects on the waveforms resulting from different receiver locations and topography are suppressed. However, presumably due to a slightly more complicated work flow associated with the different origin times of the events and the opposite geometry, source array techniques are not very common. When earthquake locations and origin times are well known and the event mechanisms are similar (and hence the waveforms), small scale source arrays are excellent tools for the analysis of crustal structures.

In the course of this thesis, the prerequisites of the usage of source arrays constructed of small Vogtland swarm events are evaluated. One aim of this thesis is to develop, test and apply source array beam forming methods and accompanied methods for the localisation of reflection or conversion sites.

22 events of the 2008/2009 earthquake swarm were selected to set up a source array. The resemblance of waveforms was assured by visual selection of events and quantified with the calculation of cross-correlation coefficients. We observed that the different events recorded at a single station generally show greater resemblances than the recordings of one event at all stations of the receiver array. This indicates a heterogeneous subsurface beneath the receiver array and a comparably homogeneous source array volume with respect to the frequency-dependent resolution of both arrays. Beam forming was applied on the Z, N and E component recordings of the source array events at 11 stations, and the results were analysed with respect to converted or reflected crustal phases. Within the source array, P phase velocities of about 6.2 km/s can be observed. Along the entire travel path, the mean velocity is 5.63 km/s. PS phases, closely following the direct P phase and presumably SP phases, arriving shortly before the direct S phase can be observed on several stations. Based on the time differences to the direct P and S phases we inferred a conversion depth of about 0.8 km. Additionally, 12 deeper events were chosen to set-up a second deeper source array in order to analyse a structural phase which is observed already on single (deep) event's traces.

The results of this thesis were presented as a poster presentation at the annual meeting of the AG Seismologie (Sept. 26-28, 2017) (Appendix p. 107).

# 3 Area of research: Vogtland/ West Bohemia

## 3.1 Geography and tectonics

The Vogtland is located in the border region of Saxony, Bavaria (both Germany) and Bohemia (Czech Republic) as the western part of the Bohemian Massif (Fig. 2). Being the easternmost section of the Variscan Orogenic Belt in Europe, extending from the Iberian peninsula to central Europe, the Variscan Belt arose from the late Palaeozoic collision of the continents Laurentia-Baltica-Avalonia and Gondwana (ca. 500 to 250 Ma ago) [O'Brien and Carswell, 1993].

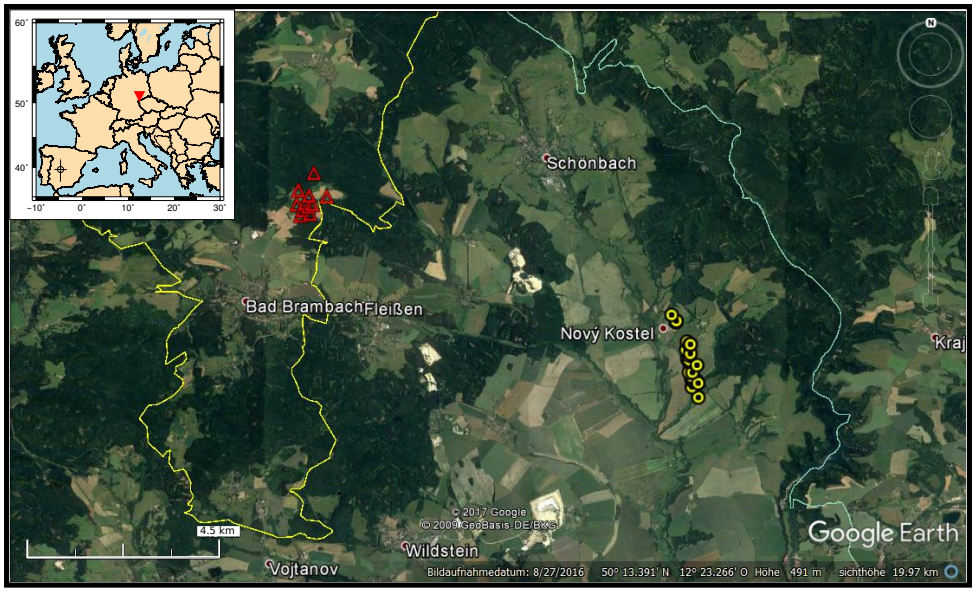


Figure 2: Location of the Vogtland within Europe and satellite image with stations of Rohrbach Array (red triangles) and source array epicentres (yellow circles). Satellite image from Google Earth.

A complex and polyphase tectonic evolution mark the late and post-Variscan deformation [Peterek et al., 1997]: Two brittle deformation stages prior to the intrusion of late-Variscan granites were identified as well as periods of crustal extension in Permo-Carboniferous to Permo-Triassic stages which led to normal faulting [Peterek et al., 1997]. Reverse NNE-SSW faulting during Triassic/Jurassic was followed by normal faulting under NNE-SSW extension in Cretaceous. A rapid uplift of the Bohemian Massif in early Cretaceous to early Paleogene due to the Alpine foreland deformation was accompanied by reverse faulting. Stages of crustal extension during the late Paleogene, Neogene and until recently are described [Peterek et al., 1997]. In Eocene, subsidence processes created the ENE trending Eger Graben [Heinicke et al., 2009], a basin between the Erzgebirge and the Fichtelgebirge. The subsidence was accompanied by extensive volcanism [Heinicke et al., 2009].

Geologically the Vogtland lies in the transition zone between three different Variscan structural units: the Saxothuringian zone in the north-west, the Teplá-Barrandian and Moldanubian zones in the south-east. North-west trending strike slip and normal faults formed during the brittle deformation accompanying the uplift of the Erzgebirge [Heinicke et al., 2009]. Some of these faults were reactivated several times during Mesozoic and Cenocoic.

At the westernmost part of the Eger Graben, younger, still-active NNE to N striking faults cut the older faults. The younger faults belong to the seismoactive Regensburg-Leipzig zone [Heinicke et al., 2009] or Regensburg-Leipzig-Rostock zone [Bankwitz et al., 2003]. The roughly 700 km long and 40 km wide zone is characterised by N-S striking faults which are composed of en echelon segments [Bankwitz et al., 2003]. Today's main focal zone of the Vogtland/ West Bohemia region is located close to Nový Kostel at an intersection of the Eger Rift and the Mariánské Lázně fault [Fischer et al., 2014]. According to the geological (surface) map presented by Heinicke et al. [2009] the focal zone is located partly in metamorphic rocks of the Erzgebirge and partly in Neogene metasediments (Figure 3). Schenk et al. [2012] state that the area of Nový Kostel is located in the crystalline unit of the Erzgebirge.

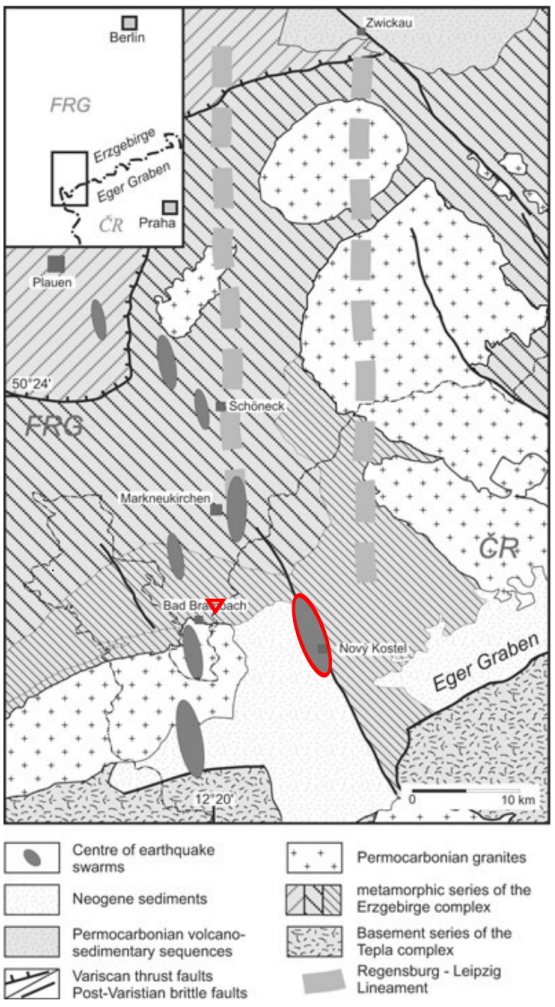


Figure 3: Geological map of NW Bohemia/ Vogtland by Heinicke et al. (2009). The inserted red triangle points towards the location of the Rohrbach array and the ellipse emphasizes the location of the earthquake swarms at the Nový Kostel focal zone.

The structure of the crust in the area was object of seismic and seismological studies (e.g. Fischer et al. [2014], Geissler et al. [2005] and Hrubcova et al. [2005], [2013] and [2016]). Geissler et al. [2007] argue that the upper mantle and middle crust are mostly composed of metasedimentary, granitic and granulitic rocks which are comparable to outcrops in the western and northern Bohemian Massif.

## 3.2 Seismic structure of the crust

The depth of the crust-mantle velocity discontinuity (Mohorovičić discontinuity, short Moho) has been investigated by receiver function analysis and in active seismic experiments. Hrubcová et al. [2005] determined a Moho depth of 27-28 km in active experiments. Using receiver functions Geissler et al. [2005] interpreted Moho depths of 27 to 38 km. Beneath the western part of the Eger Rift a thinning of the crust to 27 km was observed. A reflectivity zone of 2-4 km thickness instead of a single interface with a sharp velocity contrast was proposed in a depth of 27 to 31.5 km [Hrubcová et al., 2013]. In a later study Hrubcová et al. [2016] inferred a reflective layer in the shallow crust (3.5-6.5 km depth) from PPP and SP phases of the 2008/2009 earthquake swarm. This is interpreted as a layer above the focal zone which might act as a barrier for shallower seismicity and a trap for fluids from the mantle. Geissler et al. [2007, p. 54] observed a seismic converter/reflector in the upper mantle at 50-60 km depth, which might be related to the base of a "metasomatic uppermost mantle containing a few percent of melts". The authors state that the uppermost mantle and lowermost crust may have experienced intrusions during Tertiary and Quaternary.

In most studies 1-D velocity models are used. However, directionally varying anisotropy has been observed [Málek et al., 2005]. Shear-wave splitting analysis revealed that the upper crust is anisotropic [Vavryčuk and Bouškova, 2008] as well as residual analysis of 112 events of the 2000 swarm [Rößler, 2006].

## 3.3 Observed geological and seismic activity

The tectonic activity of the Vogtland is for one thing demonstrated by its reoccurring swarm activities with magnitudes usually below 4 [e.g. Fischer et al., 2014]. Seismic activity observations date back to the middle ages and macroseismic data has been recorded since the beginning of the 18th century [Fischer et al., 2014]. The first permanent Czech seismic station was established in 1908 at Cheb as a reaction to three intensive earthquake swarms at the turn of the 20th century. Figure 4 by Bankwitz et al. [2003] shows the *Pocatky-Plesna fault zone (PPZ)* close to Nový Kostel. This fault zone is composed of alternating NNW and NNE striking faults, being Riedel's first order $R_1$ and second order P shears of a sinistral strike-slip along the N-S zone [Bankwitz et al., 2003]. The fault plane solutions of events occurring along the fault zone show sinistral strike-slip movements with a vertical shear component along N-S planes [Bankwitz et al., 2003]. Fischer et al. [2014] argue that the major focal zone has migrated since the first records of seismic activity: The 1824 swarm was observed near Hartenberg and Oloví. Between 1897 and 1962 four swarms occurred north and north-east of the 1824 location and since 1985, sev-

eral earthquake swarms were observed at the Nový Kostel focal zone. The occurrence of recent earthquake swarms along with their triggering mechanisms is discussed in section 3.4.

Evidences of geological activity are additionally seen in local earthquake seismic tomography. In a north-south running $v_p$ and $v_p/v_s$ profile Mousavi et al. [2015] image potential fluid pathways, which are visible through channel-like increased $v_p/v_s$-ratios. These structures start from the surface and run down to 12 km depth. Similar fluid pathways were interpreted from magnetotelluric experiments [Weckmann et al., 2016]. The possible fluid pathways show up as channels of moderate conductivity within an otherwise low-conductive crust. Two mofettes at Bublák and Hartoušov and the Mýtina Maar volcano show up with very high conductivities.

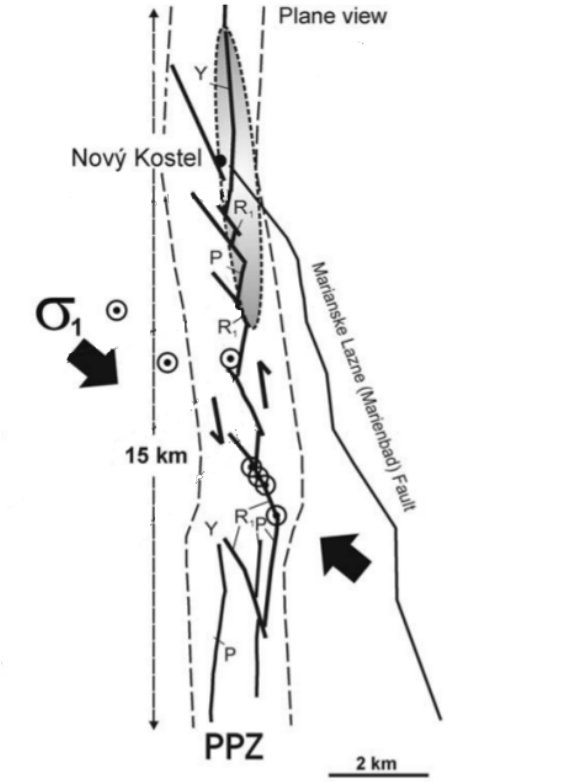


Figure 4: The N-S striking Pocatky-Plesna fault zone (PPZ). The principal stress direction $\sigma_1$ is indicated as well as the sinistral movement along the fault. Circles indicate positions of mofettes or springs. Figure taken from Bankwitz et al. (2003) and slightly simplified.

Other evidences of tectonic activity are $CO_2$ emanations [e.g. Bräuer et al., 2014] and quaternary volcanism [e.g. Mrlina et al., 2009]. $CO_2$ degassing is observed at several mofettes and springs in the Vogtland/ West Bohemia region [e.g. Bräuer et al., 2014]. The degassing might result from ultra-alkaline to alkaline magma, situated between the asthenosphere and basal lithosphere [Geissler et al., 2007]. A three month lasting increase of $^3He/^4He$ ratio in spring 2006 at all degassing locations near Nový Kostel is interpreted by Bräuer et al. [2014] as an indication of hidden magmatic activity, likely a magmatic intrusion process from the upper mantle into the lower crust. From rock samples volcanic activity between Early Oligocene (>31 Ma) and Pleistocene (<0.1 Ma) was inferred [Ulrych et al., 2003]. Evidence of the latest volcanically active period in Pleistocene was found at the western Eger Rift area and the NNW-SSE trending Cheb-Domazlice Graben. The geological activity indicates an ongoing rifting process [Ibs-von Seht et al., 2008].

Crustal deformation was observed at five sites in West Bohemia in five two-day GPS

campaigns between 2007 and 2009 by [Schenk et al., 2012]. In the co-seismic phase a maximum subsidence of 16.7 cm at Kopania, south of Nový Kostel was observed. However, at the epicentral area 4-10 m thick alluvium combined with forested valleys impeded the observation of surface soil effects [Schenk et al., 2012]. The subsidence at Kopania most likely reflects reverse faulting processes resulting from uprising fluids into the upper crust due to deep magmatic processes [Schenk et al., 2012].

## 3.4 Earthquakes swarms at the Nový Kostel focal zone: Triggering processes and tectonic implications

Large earthquake swarms were observed at Nový Kostel in 1985/1986, 1997, 2000, 2008/2009 and 2011 [Fischer et al., 2014]. Seismic activity in 2014 was in contrast interpreted as a classical aftershock sequence, triggered by three main shocks with magnitudes of $M_L$ 3.5, 4.4 and 3.5 [Hainzl et al., 2016]. Swarm earthquakes are earthquakes clustered in time and space which are not associated to a main shock. Shearer [2009] explains that these earthquakes are likely to be triggered by underlying physical processes such as slow creep or fluid movement. According to Fischer et al. [2014] the occurrence of swarm events instead of large single events with fore- and aftershocks can be a consequence of a heterogeneous stress field or a weakened crust without a single well developed fault. In contrast, Dahm et al. [2013, p. 93] state that "nowadays earthquake swarms are typically interpreted as a consequence of fast fluid movement at depth and triggering by fluid-induced effective stress". The triggering of seismic swarms in the Vogtland area has been discussed in several studies.

Hainzl and Fischer [2002] studied the time distribution of the swarm events in 2000. From the temporal behaviour they infer that the swarm was initiated by intruding fluids and kept active by stress field changes. In a later study Hainzl and Ogata [2005] state that fluid pressure driven events occurred mainly in the beginning of the swarm and after more quiet periods. Pore pressure changes trigger only few percent of the total activity, while most of the seismicity pattern is explained by stress triggering. Hainzl [2004] reproduced the temporal distribution and the increase of the seismic moment release of the same swarm. According to the author, the temporal characteristics result from stress-triggering, while the spreading of the hypocentres seems to result from fluid diffusions. The swarm in 2008/2009 ruptured fault patches which border on patches mainly active in 2000, but a significant overlap of 2000 and 2008/2009 fault patches has additionally been observed [Hainzl et al., 2012]. The up-dip migration of activity within the 2008/2009 swarm is explained by the authors through either hydrofracture growth or a diffusion process. An initial fluid pressure increase of up to 30 MPa was estimated. The hypothesis of fluid

driven seismic activity is supported by the isotopic content of $CO_2$ degassing in mofettes and springs close to the Nový Kostel focal zone [Bräuer et al. e.g. 2014]. Heinicke et al. [2009] assume that hydrothermal alteration like the dissolution of rock and mechanical weakening amplifies the weakening of the crust. According to the authors this hypothesis is supported from quartz samples of the fracture zone and from numerical modelling of alteration-induced earthquake swarm triggering.

For this study, data of the earthquake swarm in 2008/2009 was used. This swarm lasted from mid-October 2008 to mid-March 2009. 14.530 events were detected by a local array near Rohrbach [Hiemer et al., 2012]. About 25.000 microearthquakes in depths of 7.6 to 11.7 km with magnitudes larger -0.5 were recorded by the WEBNET array [Hrubcová et al., 2013]. Vavryčuk et al. [2013] analysed focal mechanisms of the 2008 swarm to obtain insight in the fault system. They propose a complex fault system composed of several fault segments with differing orientations (Fig. 5a) with the N-S running faults being most active (marked as 1 and 2 in Fig. 5a). Segments 1 and 2 show similar strike angles of 169° but slightly varying dip angles of 68° and 80°. Segment 3 shows a similar strike but reverse. Segments 4 and 5 cross segment 2 with strike angles of 304°. Fig. 5b by Vavryčuk et al. [2013] shows a tectonic sketch obtained from the focal mechanisms of selected events. The maximum and minimum compressive stresses are displayed as well as focal mechanisms associated with the faults. Fig. 6 shows cross sections of swarms in between 1991 and 2012. The 2001 and 2009 swarms in the southern part of the NK focal zone follow the pattern visible in segments 1 and 2 of Fig. 5a [Fischer et al., 2014]. However, the swarm in 1997 in the northern part of the fault as well as a great part of the 2011 swarm occur at a segment which dips in opposed direction. The northern part of the fault shows a wedge-like shape with a shallower part dipping west and a deeper part dipping east [Fischer et al., 2014].

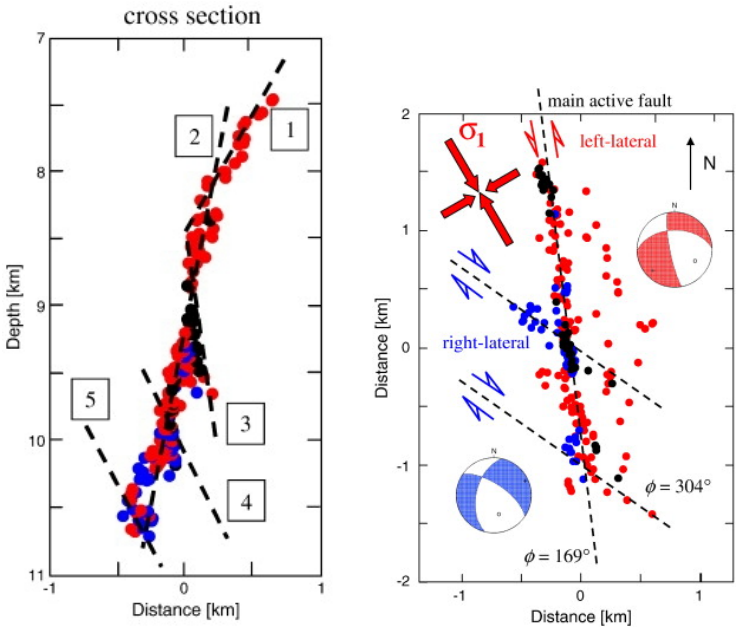


(a) (b)

Figure 5: (a) Cross section of the 2008/2009 earthquake swarm. The complex fault system consists of multiple segments: Segment 1: strike=169°/ dip=68°/ rake=-44°, 2: 169°/80°/-44°, 3: 359°/86°/32°, 4+5: 304°/66°/-137°. (b) Tectonic sketch of the main focal zone. The left-lateral fault striking in north-south direction is most active. Both figures by Vavryčuk et al. [2013].

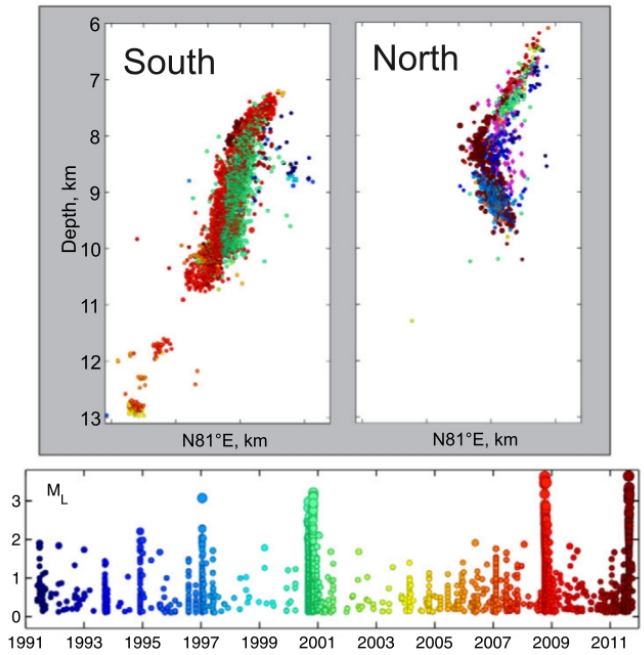


Figure 6: Cross sections of swarm activity from 1997 to 2012 and temporal distribution of events with event magnitudes [Fischer et al., 2014]. The fault plane dips west except for the northern lower part dipping east.

# 4 Theoretical background

## 4.1 Array Seismology

The term array seismology refers to the usage of numerous seismometers in a well-defined configuration instead of single stations. Arrays offer dense spatial sampling of the seismic wavefield and provide directional information [Rost and Thomas, 2002]. The geometry of an array defines its resolution, therefore a good azimuthal coverage should be achieved as well as reasonable interstation distances with respect to the expected wavelengths. For a 2D array the spatial Nyquist sampling theorem requires that the distance between two stations is smaller than half of the (desired) apparent wavelength.

*Delay and sum beam forming* is one common method in the field of array seismology. The method is based on the assumption of plane wave fronts which arrive at the single receivers of an array at different times (Fig. 7). The direction of an approaching wave front can be calculated from the arrival times at the receiver stations. The wave is described as a plane wave front with a normal vector pointing in travelling direction. The normal vector is described by a back azimuth angle $\Theta$ (or *baz*), providing the directional information in a horizontal plane, an incident angle $i$ and a velocity $v$. The slowness vector $\vec{s}$ contains all these information:

$$\begin{aligned} \vec{s} &= (s_x, s_y, s_z) \\ &= (\frac{sin(\Theta)}{v_{app}}, \frac{cos(\Theta)}{v_{app}}, \frac{1}{v_{app}} \cdot tan(i)) \\ &= \frac{1}{v_0}(sin(i)sin(\Theta), sin(i)cos(\Theta), cos(i)). \quad (1) \end{aligned}$$

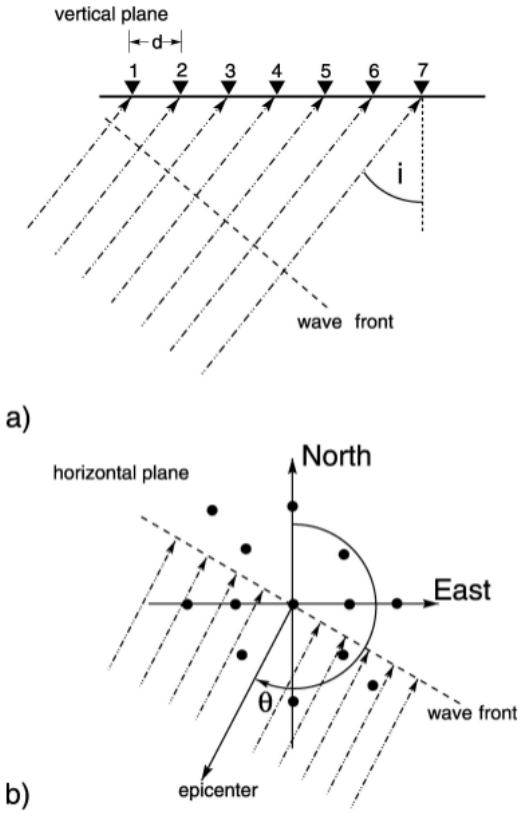


Figure 7: Wavefront crossing an array in vertical (a) and horizontal plane (b). i: incidence angle, $\Theta$ : back azimuth. Figure from [Rost and Thomas, 2002]

From a slowness vector $\vec{s}$ describing the plane wave, delay times $dt$ are calculated for each station with respect to one reference station. If the traces of all stations are shifted by these times, phases with an appropriate back azimuth and slowness are amplified while incoherent noise and phases with different slowness and azimuths are suppressed [e.g. Rost

and Thomas, 2002]. Phases with low amplitudes which are not or hardly visible on single traces can be studied. When beam forming is performed with a number of different time shifts calculated from different slowness vectors and back azimuths, the highest amplitude or power stack of a phase corresponds to the best solution for direction and slowness.

The following mathematical description of the beam forming method follows closely Rost and Thomas [2002]. The recorded wave field at a central station $x_{centre}$ consists of the signal *f(t)* and noise $n_i(t)$:

$$x_{centre}(t) = f(t) + n_i(t). \tag{2}$$

The incident wave front has different travel times to each station. The difference in travel time depends on the velocity of the wave front and the location of each station. The time series recorded by station i with the location $\mathbf{r}_\mathrm{i}$ can be written as:

$$x_i(t) = f(t - \mathbf{r}_i \cdot \mathbf{s}_{hor}) + n_i(t) \tag{3}$$

[Rost and Thomas, 2002].

$\mathbf{s}_\mathrm{hor}$ is the horizontal slowness vector. The removal of the time shift can be represented as

$$\tilde{x}_i(t) = x_i(t + \mathbf{r}_i \cdot \mathbf{s}_{hor}) = f(t) + n_i(t + \mathbf{r}_i \cdot \mathbf{s}_{hor}) \tag{4}$$

[Rost and Thomas, 2002].

The final *delay-and-sum* trace for an array with M components is then computed by

$$b(t) = \frac{1}{M} \sum_{i=1}^{M} \tilde{x}_i(t) = f(t) + \sum_{i=1}^{M} n_i(t + \mathbf{r}_i \cdot \mathbf{s}_{hor}) \tag{5}$$

[Rost and Thomas, 2002].

If $n(t)$ is "white" noise, the variance does not change when the traces are stacked. Coherent signals with the appropriate slowness are amplified through stacking.

## 4.2 Reciprocity of the Green's function

Most generally spoken, the principle of reciprocity states that if the locations of the sources and receivers are exchanged, the same seismogram should be recorded assuming a unidirectional unit impulse source. The following section closely follows the work by Aki and Richards [2002], who derived the reciprocity of the Green's function for unit impulse sources and the publication by Spudich and Bostwick [1987] dealing with the derivation

of the source array concept from the reciprocity theorem for double couple point sources described through the seismic moment.

Based on the Lagrangian description, a constraint on the acceleration, body forces ($\vec{f}$) and tractions acting in a volume V with surface S is expressed by

$$\frac{\partial}{\partial t}\iiint_V \rho\frac{\partial \vec{u}}{\partial t}\ \ dV = \iiint_V \vec{f}\ \ dV + \iint_S \vec{T}(\vec{n})\ \ dS \tag{6}$$

[Aki and Richards, 2002].

The traction $\vec{T}(\vec{n})$ is the force acting per unit area across an (internal) surface and quantifies the contact force with which particles on one side of the surface act upon particles on the other side [Aki and Richards, 2002]. $\vec{n}$ is the normal vector to the surface S. From this equation an equation of motion can be obtained.

Supposing that $\vec{u} = \vec{u}(\vec{x}, t)$ is a displacement field due to body forces $\vec{f}$, boundary conditions on surface $S$ and initial conditions at time t = 0 and $\vec{v} = \vec{v}(\vec{x}, t)$ being another displacement field due to body forces $\vec{g}$ and boundary and initial conditions different from the conditions for $\vec{u}$. $\vec{T}(\vec{u}, \vec{n})$ and $\vec{T}(\vec{v}, \vec{n})$ are tractions on surfaces normal to $\vec{n}$ due to the displacements $\vec{u}$ and $\vec{v}$. Due to Betti's theorem a first reciprocal relation between $\vec{u}$ and $\vec{v}$ is then

$$\begin{aligned}&\iiint_V (\vec{f} - \rho\ddot{\vec{u}}) \cdot \vec{v}\ \ dV + \iint_S \vec{T}(\vec{u}, \vec{n}) \cdot \vec{v}\ \ dS \\ =\ &\iiint_V (\vec{g} - \rho\ddot{\vec{v}}) \cdot \vec{u}\ \ dV + \iint_S \vec{T}(\vec{v}, \vec{n}) \cdot \vec{u}\ \ dS\end{aligned} \tag{7}$$

[Aki and Richards, 2002].

By inserting $T_i = \tau_{i,j}n_j$, $\rho\ddot{\vec{u}} = f_i + \tau_{ij,j}$, $\rho\ddot{\vec{v}} = g_i + \tau_{ij,j}$ and $\tau_{ij} = c_{ijkl}e_{kl}$ and sorting for $V$ and $S$, a vector theorem for the 2nd order spatial derivatives occurring in the wave equation of elasticity is obtained.

$$\iiint_V (v_i(c_{ijkl}u_{kl})_{,j} - u_i(c_{ijkl}v_{kl})_{,j})\ \ dV = \iint_S (v_iT_i(\vec{u}, \vec{n}) - u_iT_i(\vec{v}, \vec{n}))\ \ dS \tag{8}$$

[Aki and Richards, 2002].

This is analogous to the Green's theorem.

Aki and Richards [2002] integrate equation (7) over a temporal range from 0 to $\tau$, leading

to

$$\begin{aligned} &\int_{-\infty}^{\infty} dt \iiint_V (\vec{u}(\vec{x},t)\cdot\vec{g}(\vec{x},\tau-t) - \vec{v}(\vec{x},\tau-t)\cdot\vec{f}(\vec{x},t)) \quad dV \\ &= \int_{-\infty}^{\infty} dt \iint_S (\vec{v}(\vec{x},\tau-t)\cdot\vec{T}(\vec{u}(\vec{x},t),\vec{n}) - \vec{u}(\vec{x},t)\cdot\vec{T}(\vec{v}(\vec{x},\tau-t),\vec{n})) \quad dS. \end{aligned} \tag{9}$$

The Green's function for elastodynamics is used for representing the displacements that occur in seismology. Realistic displacements are approximated from displacements produced by simple unidirectional impulse sources [Aki and Richards, 2002]. The Green's function $G$ gives the displacement at a point $\vec{x}$ resulting from a unit force applied at point $\vec{\xi}$. Most generally it holds that

$$u_i(\vec{x},t) = G_{in}(\vec{x},t;\vec{\xi},\tau)\cdot f_n(\vec{\xi},\tau), \tag{10}$$

where $u(\vec{x},t)$ is the displacement field at position $\vec{x}$ and time $t$, $G$ is the Green's function which describes the displacement at point $\vec{x}$ and time $t$ which results from the force vector $f$ applied at position $\vec{\xi}$ and time $\tau$ [cf. Aki and Richards [2002]].

Under the assumption of initial conditions $\mathbf{G}(\vec{x},t;\vec{\xi},\tau) = 0$ and $\partial\mathbf{G}(\vec{x},t;\vec{\xi},\tau)/\partial t = 0$ for $t \leq \tau$ and $\vec{x} \neq \vec{\xi}$ and for time-independent boundary conditions on surface S, it holds that

$$\mathbf{G}(\vec{x},t;\vec{\xi},\tau) = \mathbf{G}(\vec{x},t-\tau;\vec{\xi},0) = \mathbf{G}(\vec{x},-\tau;\vec{\xi},-t), \tag{11}$$

which is a reciprocal relation for source and receiver times [Aki and Richards, 2002]. If G satisfies homogeneous boundary conditions on the surface a reciprocal relation for source and receiver positions can be obtained: $\vec{f}$ is a unit impulse applied in $m$-direction at $\vec{x} = \vec{\xi_1}$ and time $t = \tau_1$ and $\vec{g}$ respectively in $n$-direction at $\vec{x} = \vec{\xi_2}$ and $t = \tau_2$. By inserting $u_i = G_{im}(\vec{x},t;\vec{\xi_1},\tau_1)$ and $v_i = G_{in}(\vec{x},t;\vec{\xi_2},\tau_2)$ into equation (9) it is deduced that

$$G_{nm}(\vec{\xi_2},\tau+\tau_2;\vec{\xi_1},\tau_1) = G_{mn}(\vec{\xi_1},\tau-\tau_1;\vec{\xi_2},-\tau_2) \tag{12}$$

[Aki and Richards, 2002]. This is a reciprocal relation for source and receiver positions. A homogeneous boundary condition on the surface S means that either the displacement or the traction vanishes at every point of the surface [Aki and Richards, 2002]. If a solution to a homogeneous equation is multiplied by a constant, the result is still a solution [Aki and Richards, 2002].

In case of $\tau_1 = \tau_2 = 0$ the equation can be written as

$$G_{nm}(\vec{\xi_2},\tau;\vec{\xi_1},0) = G_{mn}(\vec{\xi_1},\tau;\vec{\xi_2},0). \tag{13}$$

This represents a purely spatial reciprocity [Aki and Richards, 2002]. Setting $\tau = 0$ results in a space-time reciprocity:

$$G_{nm}(\vec{\xi}_2, \tau_2; \vec{\xi}_1, \tau_1) = G_{mn}(\vec{\xi}_1, -\tau_1; \vec{\xi}_2, -\tau_2) \tag{14}$$

with an impulse applied at position $\vec{\xi}$ and time $\tau$ [Aki and Richards, 2002].

The principle of reciprocity states that if the locations of the sources and receivers are exchanged, the same seismogram should be recorded assuming a unidirectional unit impulse source. In seismology, the Green's function reciprocity means "that the source and receiver positions in a seismic experiment can be exchanged without affecting the observed seismograms" [Spudich and Bostwick, 1987, p. 526]. Spudich and Bostwick derived the source array concept from the reciprocity theorem for double couple point sources described through the seismic moment. The following passage strictly follows their derivation.

May $\vec{f}$ be a point on a fault surface A with a unit normal vector $\vec{n}$ and $\vec{o}$ be the observer location. $\vec{s}(\vec{f}, t)$ is the dislocation on the fault system due to a force applied at point $f$ and time $t$. $G_{kp}(\vec{y}, t; \vec{x}, 0)$ is then the $k$th component of the displacement at position $\vec{y}$ and time t, caused by a unit impulse force applied at position $\vec{x}$ and time $t = 0$ in $p$-direction. Following the reciprocity theorem by Aki and Richards [2002] it holds that

$$G_{kp}(\vec{y}, t; \vec{x}, 0) = G_{kp}(\vec{x}, t; \vec{y}, 0). \tag{15}$$

The $m$ component of the ground displacement $u_m$ at position $\vec{o}$ and time t caused by a dislocation on $A$ (assuming no other body forces) is represented in two ways:

$$u_m(\vec{o}, t) = \int_{-\infty}^{\infty} dt' \int_A s_i(\vec{f}, t') \cdot c_{ijpq}(\vec{f}) \cdot n_j \cdot G_{mp,q}(\vec{o}, t - t'; \vec{f}, 0) dA \tag{16}$$

and

$$u_m(\vec{o}, t) = \int_{-\infty}^{\infty} dt' \int_A s_i(\vec{f}, t') \cdot c_{ijpq}(\vec{f}) \cdot n_j \cdot G_{pm,q}(\vec{f}, t - t'; \vec{o}, 0) dA \tag{17}$$

with

$$G_{mp,q} = \frac{\partial}{\partial x_q} G_{mp} \text{ and } G_{pm,q} = \frac{\partial}{\partial x_q} G_{pm} \tag{18}$$

[Spudich and Bostwick [1987] based on Burridge and Knopoff [1964]].

$c_{ijpq}(\vec{f})$ are the elastic components of the medium. $G_{mp,q}$ is the derivative of the displacement at $\vec{o}$ caused by a force couple applied at $\vec{f}$ (*normal* geometry). $G_{pm,q}$ is the displacement gradient on the fault caused by a point force applied at the observer position

in m direction (reciprocal geometry). $c_{ijpq}n_jG_{pm,q}$ is understood as the ith component of traction T across the fault surface due to a point source applied at the observer location.

$$c_{ijpq}(\vec{f}) \cdot n_j \cdot G_{pm,q} = T_i^m(\vec{f}, t; \vec{o}, 0) \tag{19}$$

[Spudich and Bostwick, 1987].

In case of microearthquakes, it is appropriate to reduce T to a point location at $\vec{f}$:

$$s(\vec{f}, t) = S \cdot \delta(\vec{f} - \vec{f_0}) \cdot H(t). \tag{20}$$

By using (19) and (20) and deriving (17), we get

$$\dot{\vec{u}}(\vec{o}, t) \coloneqq S_i \cdot T_i^m(\vec{f_0}, t; \vec{o}, 0). \tag{21}$$

Introducing a unit vector $\vec{d} \coloneqq \vec{S}|\vec{S}|^{-1}$ lying in the fault plane in direction of the dislocation vector $\vec{S}$ leads to

$$|\vec{S}|^{-1} \cdot \dot{\vec{u}}(\vec{o}, t) = \vec{d} \cdot T^m(\vec{f_0}, t; \vec{o}, 0). \tag{22}$$

Spudich and Bostwick [1987] now introduce the seismic moment $M_0$. The normalized ground velocity can than be expressed as

$$\dot{\vec{\mathcal{U}}}_m(\vec{o}, t) \coloneqq M_0^{-1} \cdot \mu(\vec{f_0}) \cdot \dot{\vec{u}}_m = \vec{d} \cdot T^m(\vec{f_0}, t; \vec{o}, 0). \tag{23}$$

Equation (23) states that the ground velocity time series $\dot{\vec{u}}_m$ at observer location $\vec{o}$ caused by a point dislocation at position $\vec{f_0}$ is, when normalized by rigidity $\mu$ and seismic moment $M_0$, identical to the traction $T$ that is experienced at $\vec{f_0}$ in dislocation direction defined by $\vec{d}$ on the fault when a point source is applied at the surface observer location $\vec{o}$ instantaneously [Spudich and Bostwick, 1987].

## 4.3 Source arrays

Source arrays are cluster of earthquakes which can be used in a similar manner as station clusters (receiver arrays). A variety of array analysis tools like frequency-wavenumber (fk) analysis, stacking and beam forming are routinely used to process data of single earthquakes which are recorded by receiver arrays. Due to the Green's function reciprocity the same array analysis techniques can be applied to single station records of a number of earthquakes.

Niazi [1969] demonstrated that source arrays can provide information about the subsurface. Clusters of underground explosions and earthquakes were used for analysis of

travel time curves with respect to phase velocities and reflection depths. Spudich and Bostwick [1987] derived the theoretical background of using source arrays. Following the reciprocity theorem, the recordings of multiple seismic events by one single station can be treated in the same way as recordings by several stations of one single source. Source arrays can be used for P and S wave coda anlysis: Scherbaum et al. [1991] used source arrays composed of microearthquakes from northern Switzerland to analyse the S-wave coda composition and the directions in which individual coda wavelets leave the source region. Using S wave coda analysis, Dodge and Beroza [1997] found out that coda waves near the 1989 Loma Prieta (California) earthquake are mainly generated near the receiver stations.

Problems in source array methods arise from imprecisely known origin times and epicentre coordinates, differences in waveforms and focal mechanisms [Krüger et al., 1996]. Therefore source arrays are rarely used in global seismology [Rost and Thomas, 2002]. To use source arrays, the studied waveforms of different events must be similar. This can either be reached by using events with very similar mechanisms like explosion sources or by deconvolving with the source wavelet.

In comparison with receiver arrays, one advantage of using source arrays is that the expensive deployment of many stations for an array is not necessary. Source arrays can be constructed whenever suitable earthquakes/ waveforms are recorded by only one receiver station. This makes its application to earthquake swarms appealing. Additionally, since the receiver station remains the same, the instrument response and the subsurface response from beneath the station remains identical [Rost and Thomas, 2002].

Similar to equation (5), the source array beam $S_i(\vec{s};t)$ for a slowness vector $\vec{s}$ and $K$ sources can be written as

$$S_i(u_S,t) = \frac{1}{K}\sum_{k=1}^{K}(a_k(t) * x_{ik}(t-k_k)) \tag{24}$$

with $a_k(t)$ being the source equalization factor and $x_{ik}$ being the seismogram of source $k$ at station $i$. $k_k$ is the time delay due to the different positions of the event. Under the assumption of a plane wave arrival, the time delay can be calculated by

$$k_k = (\vec{x}_k - \vec{x}_0)\cdot\vec{s} \tag{25}$$

## 4.4 Double-Beam method

Combining source and receiver array beam forming is called double-beam method (DBM) [Krüger et al., 1996] or double-array stacking [Hutko et al., 2009]. The double-beam method was presented by Krüger et al. in 1996 as a new array technique using source and receiver array beam forming simultaneously. The simultaneous usage of both beams provides slowness information *both* in the source and receiver region [Krüger et al., 1996 and Scherbaum et al., 1997]. By combining directional information of a wavelet leaving the source array and the same wavelet arriving at the receiver array, the travel path can be traced and scatterers or reflection interfaces can be located [Rietbrock and Scherbaum, 1999].

Figure 8 shows the principle of the double-beam method. Compared to either receiver array or source array methods, the region where the rays turns is sampled more efficiently, improving the resolution of structures in the Earth's interior [Rost and Thomas, 2002].

The exact coordinates, origin times and depths of all earthquakes or sources are needed to use beam forming on source arrays. In double-beam method, both, the source and receiver arrays are used to construct double-beams (Fig. 8). Similar to equation 5 and 24 the receiver array beam can be written as

$$R_k(u_R, t) = \frac{1}{N} \sum_{i=1}^{N} (x_{ik}(t + r_i \cdot u_r)) \qquad (26)$$

with $x_{ik}$ being the seismogram of source $s_k$ recorded at station $r_i$ [Rost and Thomas, 2002].

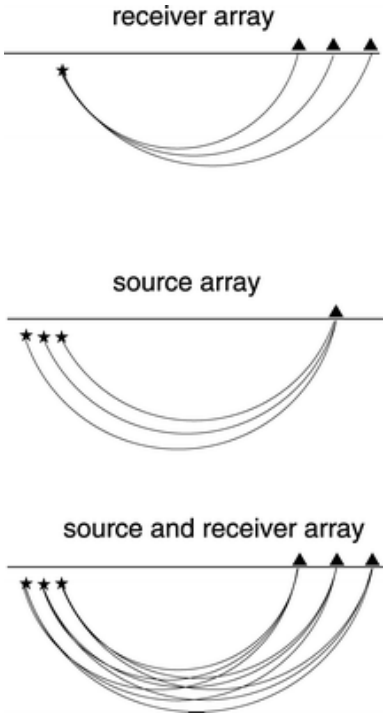


Figure 8: Principle of source array, receiver array and double-beam. Stars denote sources and triangles receiver stations [Rost and Thomas, 2002].

The formulas 24 and 25 describe the source array beam with time delay *dt*. The source delay times *dt* compensate depth and location differences between the sources. They are calculated for a slowness vector $\vec{s}$ assuming plane-wave propagation and a constant medium velocity. To perform double beam forming, the traces are first delayed with *dt* for each station $i$ of the receiver array and summed up to form a source array beam $S_i(v,t)$ for a phase with slowness $\vec{s_s}$ [Rost and Thomas, 2002]. Afterwards the time delays $\tau_i = (r_i - r_0)\vec{s_r}$ are calculated for each station $i$ of the receiver array for a receiver slowness $\vec{s_r}$. The source array beams are then delayed with

$\tau_i$ and summed up to form the double beam:

$$D_i(u_R, u_S, t) = \frac{1}{I} \sum_{i=1}^{I} (S_i(u_S, t - \tau_i)) \tag{27}$$

[Rost and Thomas, 2002].

Until now, the double-beam method has mainly been applied in teleseismic array seismology. Scherbaum et al. [1997] used nuclear-explosion data for detecting structures in the deep mantle. The probability of a region to explain kinematic phase properties is determined with a spatial likelihood distribution method for slowness and azimuth values of source and receiver array and delay times with respect to a reference phase. Information on the scattering strength is obtained by a double beam stack migration with respect to theoretical slowness and azimuth values for potential scatters in a 3-D grid. Scattering volumes within the lower mantle below the Eurasian side of the arctic were observed [Scherbaum et al., 1997]. Krüger et al. [2001] detected scatterers near the Marianna slab using a cluster of deep fore- and aftershocks of the 23-AUG-1995 Mw=7.1 earthquake in the Marianna subduction zone. The events were recorded with the Warramunga array in Australia.

Hutko et al. [2009] used the DBM for analysing the D" layer and an ultra low velocity layer beneath the Cocos Plate, Mexico and the Pacific Ocean using the core reflection phases PcP. Applying the double beam method to induced microearthquakes in the vicinity of the KTB borehole in Oberpfalz, Germany, Rietbrock and Scherbaum [1999] detected reflected phases from the metamorphic Erbendorf body.

# 5 Set-up of source and receiver array

## 5.1 The receiver array at Rohrbach

Fig. 9 shows the set-up of the receiver array which was installed by members of the University of Potsdam in the village of Rohrbach during the 2008/2009 earthquake swarm [Roessler et al., 2008]. The temporary array started monitoring 12 days after the onset of the swarm on the 6th October 2008 and run until January 2009 [Hiemer et al., 2012].

The array consisted of 11 stations with LE-3D/5s seismometers with interstation distances in the order of 0.1 to 0.4 km and an aperture of about 0.75 km (Fig. 9 and Table 1). The Rohrbach array was situated at an epicentral distance of about 10 km west-north-west of the Nový Kostel focal zone. Data was continuously recorded with a sampling frequency of 250 Hz, enabling the registration of weak signals from small earthquakes [Hiemer et al., 2012]. According to Hiemer et al. [2012] the detection threshold of the array is $M_c$=-0.4. The data of the Rohrbach array is available at the GEOFON webpage [http://geofon.gfz-potsdam.de/].

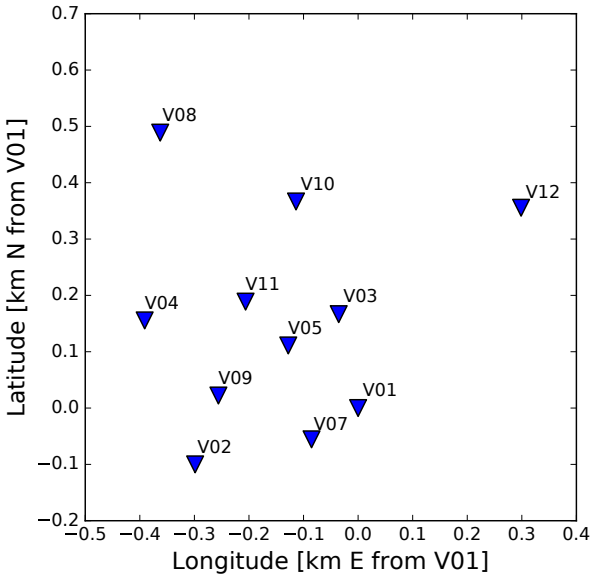


Figure 9: The Rohrbach array installed in 2008 during the earthquake swarm. X- and y- axes show latitude and longitude in km with respect to station V01.

Table 1: Information on receiver array at Rohrbach.

| Station | Latitude (°) | Longitude (°) | Elevation (m) |
|---|---|---|---|
| V01 | 50.2404 | 12.3298 | 635 |
| V02 | 50.2395 | 12.3256 | 649 |
| V03 | 50.2419 | 12.3293 | 633 |
| V04 | 50.2418 | 12.3243 | 643 |
| V05 | 50.2414 | 12.328 | 639 |
| V07 | 50.2399 | 12.3286 | 638 |
| V08 | 50.2448 | 12.3247 | 645 |
| V09 | 50.2406 | 12.3262 | 645 |
| V10 | 50.2437 | 12.3282 | 637 |
| V11 | 50.2421 | 12.3269 | 639 |
| V12 | 50.2436 | 12.334 | 624 |

## 5.2 Earthquake data and event catalogue

Waveform data of the Rohrbach Array of the 2008/2009 swarm was downloaded from the GEOFON webpage [Roessler et al., 2008]. An event catalogue with a location accuracy of 100 m was compiled by T. Fischer using the WEBNET seismic network with a relative master-event localization based on precise arrival-time picking [Fischer et al., 2010].

A typical event of the source array is presented in Fig. 10. The associated frequency spectrum in Fig. 11 is shown to emphasize the high frequency content of the P and S wave signals between 10 and 50 Hz.

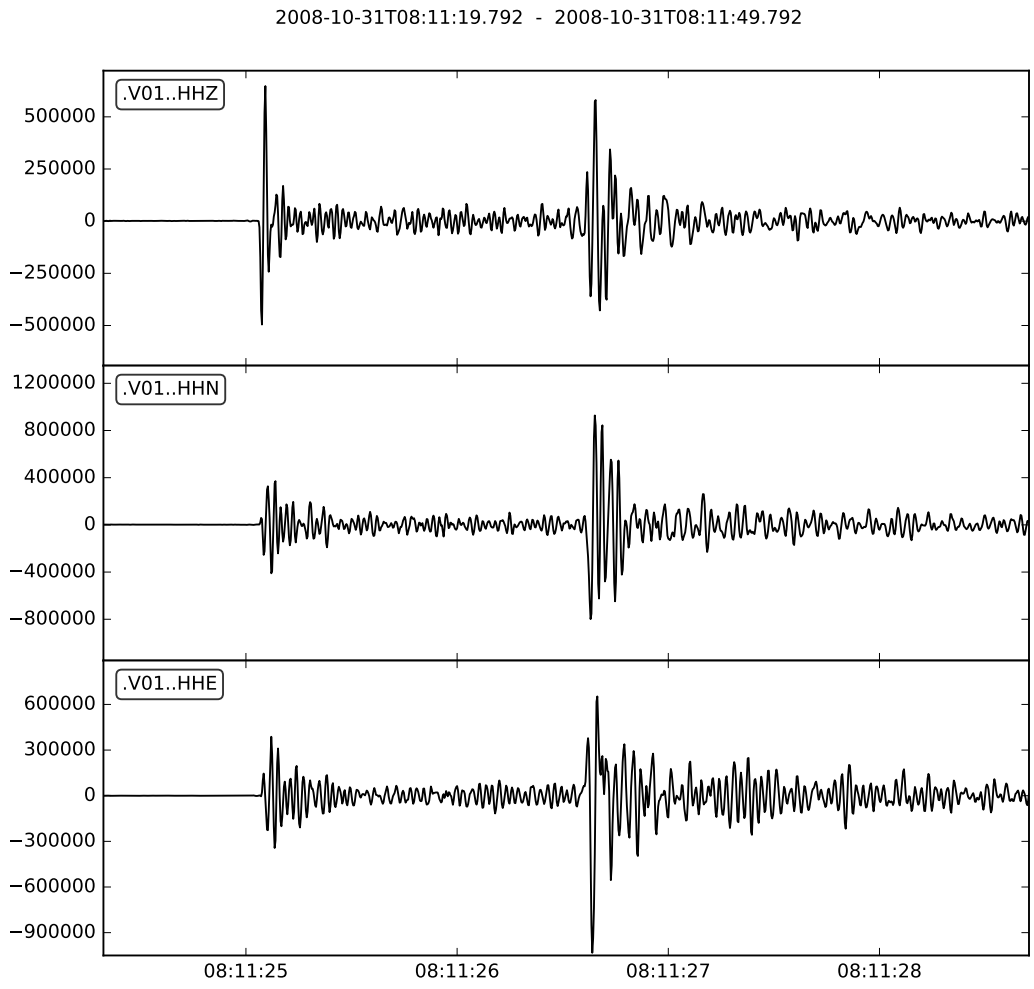


Figure 10: Example event (88004906 - 2008-10-31 08:11:22.890, M 1.4) of the source array, recorded at station V01. High-pass filtered with 1 Hz corner frequency. Sampling frequency = 250 Hz.

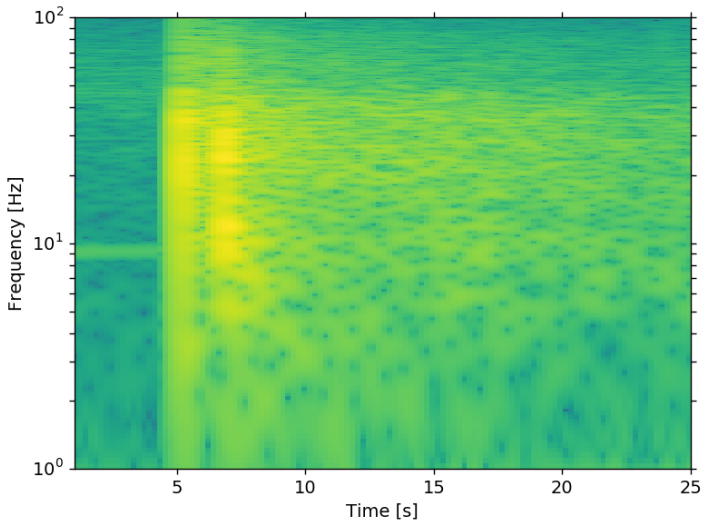


Figure 11: Spectrogram of Z-component of sample event from previous figure 10. Both, P and S waves mainly contain frequencies between 10 and 50 Hz.

## 5.3 Source array

Due to more than 5500 earthquakes in the 2008-swarm catalogue, the source array can be configured in countless ways. To obtain a optimal 3-D coverage, an array with event locations distributed in all directions would be favourable. Being composed of 19 elements the events could be located on spherical shells of different radius like in Fig. 12.

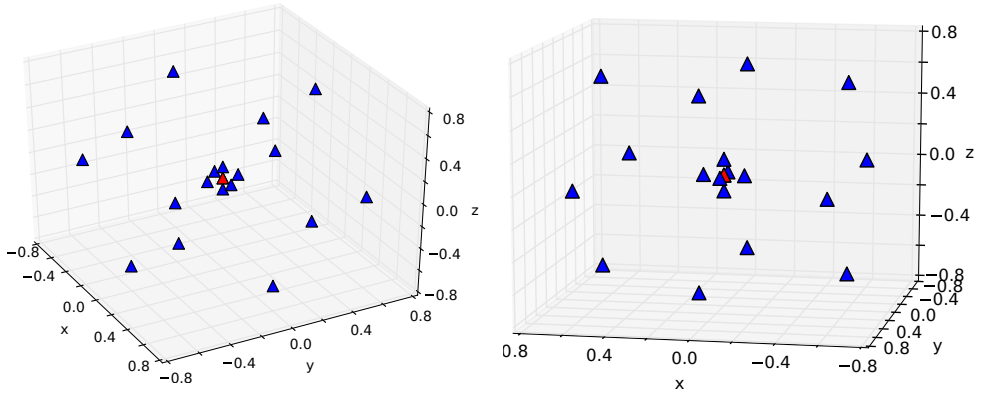


Figure 12: Source array with good 3-D coverage composed of 19 events on two spherical shells, shown in two perspectives.

### 5.3.1 Constructing a source array

However, the earthquakes at the Nový Kostel focal zone are not distributed evenly in space but located on the north-south striking and west dipping fault plane (Fig. 13). Therefore the best achieved source array is clearly more elongated in directions of the

fault plane than perpendicular to it. This leads to less resolution of phases travelling perpendicular to the fault plane.

The design of any array depends on the studied wavelengths. Havskov and Alguacil [2010] summarize the relation of the set-up and the apparent wavelength $\lambda_{app}$ for receiver arrays in the equation $2d < \lambda_{app} < D$ where D is the array size and d the station spacing. This formula results from the Nyquist theorem, which states that for an apparent wavelength $\lambda_{app}$ to be sampled the station spacing in ray direction must be less than $\lambda_{app}/2$ [Havskov and Alguacil, 2010]. On the other hand, the resolution of a wavenumber $k = 2\pi/\lambda_{app}$ requires that the array size is at least $\lambda_{app}$. With smallest interstation spacings of about 100 m in a 3-D array and a maximum aperture of 2 km, frequencies of 3-30 Hz ($v_p$=6.2 km/s) and 2-18 Hz ($v_s$=3.6 km/s) can be resolved, assuming that $\lambda = \lambda_{app}$ for a direction that is covered by event locations in the mentioned distances. In directions with less locations and other distances, the resolution of wavelengths/ frequencies is restricted. For comparison, the receiver array resolves frequencies of 5 to 20 Hz for $v_p$= 4 km/s and 3-10 Hz for $v_s$= 2.4 km/s in case of horizontally travelling waves. More general for receiver arrays it holds that $\lambda = \lambda_{app} sin(i)$.

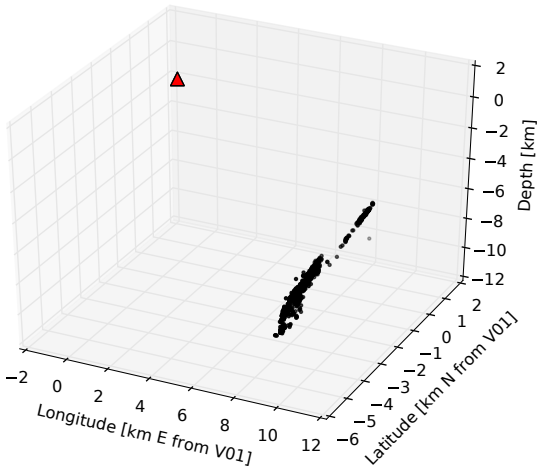


Figure 13: The earthquakes of the 2008 swarm are located on a fault surface, elongated in north-south direction and dipping slightly towards west. Locations from T. Fischer [Fischer et al., 2010]. The red triangle indicates the location of station V01.

As stated above, the basic idea of designing an 3-D source array was to create an array which is composed of event locations on spherical shells around a centre event. The centre event was defined by selecting an event with latitude, longitude and depth values close to the medians of all events. Then the distances of all other events to that centre event were calculated and earthquakes in distances of 0.1-0.15 km, 0.35-0.4 km and 0.65-0.7 km were collected as potential candidates for the source array. Smaller interstation distances than the location accuracy of the catalogue (100 m) were mostly avoided. Out of these events for each spherical shell the six events with maximum and minimum latitude, longitude and depth were plotted as reference. Some events were removed and others added after visual control to obtain the best possible coverage of all directions and distances. Events with too little waveform similarity and low signal-to-noise ratio were removed based on visual impression. To enhance the resolution of the array, some events were added manually at

open spots or favourable positions. The obtained source array is presented in Fig. 14. It consists of 22 earthquakes (Table 2). The obtained interstation distances are not very evenly distributed (Fig. 14d). Different set-ups of the source array, leaving out single event locations and adding others, were tested by comparing beam forming results and the stability of the beam forming process.

Table 2: Information on source array events. Based on information from event catalogue of T. Fischer [Fischer et al., 2010].

| Event | Origin time | Lat. (°) | Long. (°) | Magn. | Depth (m) |
|---|---|---|---|---|---|
| 88004344 | 2008-10-20 11:17:56.380 | 50.218844 | 12.449793 | 0.9 | 7879 |
| 88004405 | 2008-10-21 02:28:53.930 | 50.218587 | 12.449654 | 1.2 | 7896 |
| 88004488 | 2008-10-27 21:53:57.440 | 50.205798 | 12.457312 | 0.7 | 7426 |
| 88004510 | 2008-10-28 02:21:35.540 | 50.20675 | 12.455114 | 0.2 | 7814 |
| 88004513 | 2008-10-28 02:45:06.770 | 50.213961 | 12.454527 | 0.6 | 7170 |
| 88004607 | 2008-10-28 09:43:40.640 | 50.213953 | 12.454294 | 0.5 | 7499 |
| 88004621 | 2008-10-28 10:08:05.020 | 50.208036 | 12.454249 | 1.5 | 8127 |
| 88004739 | 2008-10-28 15:50:54.370 | 50.210628 | 12.455345 | 1.3 | 7479 |
| 88004762 | 2008-10-28 17:11:39.700 | 50.207084 | 12.45536 | 0.6 | 7795 |
| 88004906 | 2008-10-31 08:11:22.790 | 50.206311 | 12.454029 | 1.4 | 7737 |
| 88005050 | 2008-11-03 13:23:26.310 | 50.212785 | 12.453159 | 0.4 | 7894 |
| 88005074 | 2008-11-05 20:51:34.880 | 50.210893 | 12.453606 | -0.5 | 7914 |
| 88005085 | 2008-11-07 14:13:58.650 | 50.210612 | 12.454374 | 0.1 | 7456 |
| 88005106 | 2008-11-08 23:11:55.240 | 50.210274 | 12.454226 | 0.4 | 7831 |
| 88005274 | 2008-11-24 07:20:55.300 | 50.212036 | 12.454545 | -0.1 | 7739 |
| 88005410 | 2008-12-09 04:49:16.120 | 50.211719 | 12.454077 | -0.1 | 7845 |
| 88004724 | 2008-10-28 15:02:40.070 | 50.209587 | 12.456846 | 1.3 | 7282 |
| 88004348 | 2008-10-20 11:36:21.800 | 50.206323 | 12.456096 | -0.1 | 7368 |
| 88004803 | 2008-10-28 23:58:46.000 | 50.214478 | 12.453442 | -0.4 | 7511 |
| 88004447 | 2008-10-24 07:04:25.010 | 50.202974 | 12.457467 | 0.9 | 7548 |
| 88004947 | 2008-11-01 04:22:41.120 | 50.220133 | 12.448163 | -0.4 | 7937 |
| 88004600 | 2008-10-28 09:20:02.460 | 50.20496 | 12.455252 | 0.7 | 8276 |

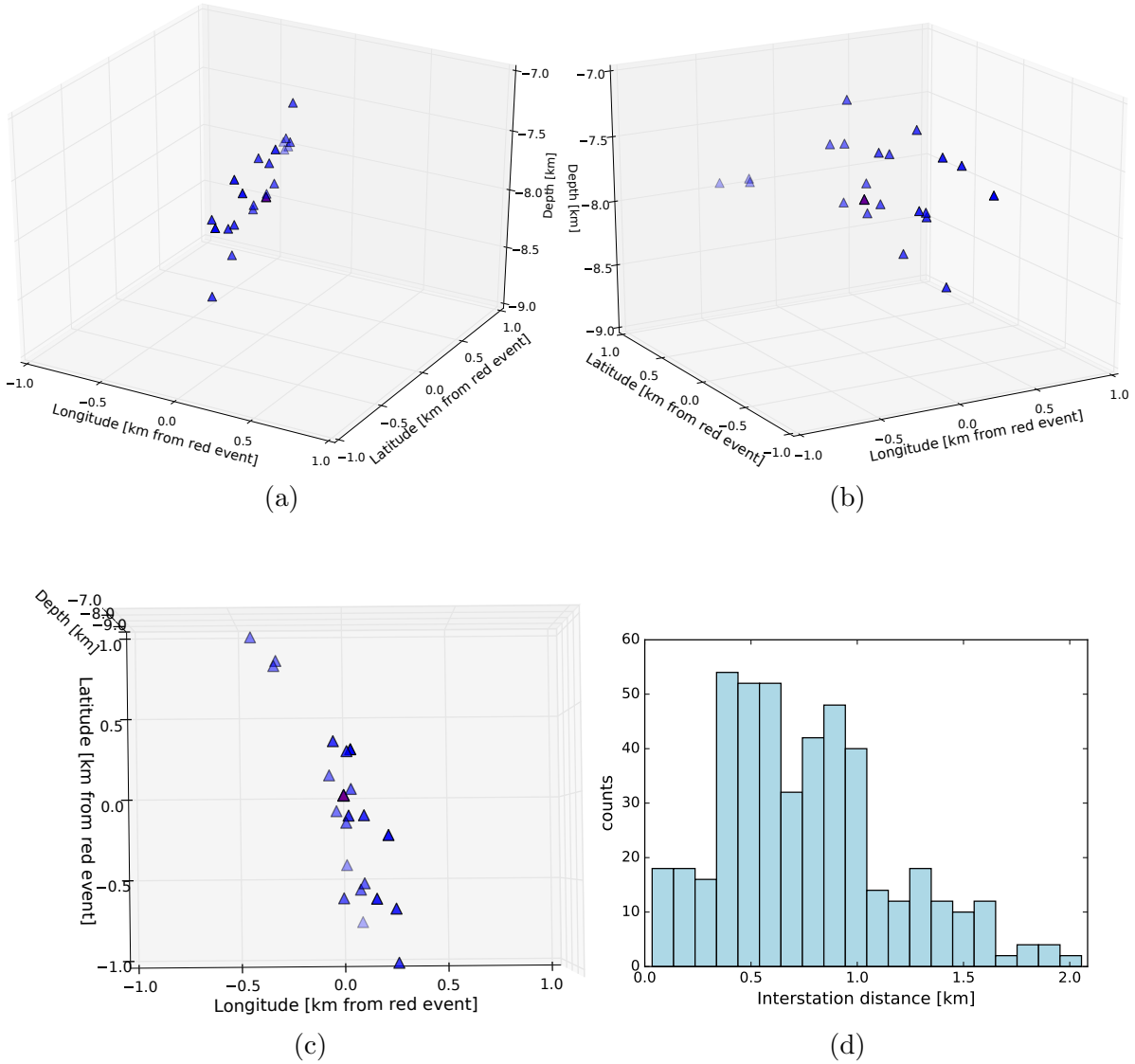


Figure 14: (a), (b), (c): Source array set up from 22 earthquake locations in three perspectives. A spherical shape with similar resolution of all directions could not be achieved. The source array is elongated in north-south direction with limited east-west resolution. (d): Distribution of interstation distances of the source array.

### 5.3.2 Empirical source array transfer function from synthetic data

Array transfer functions are a tool for analysing the sensitivity and the resolution of an array for different slowness and frequency contents. Instead of calculating a 3-D transfer function analytically an empirical transfer function was obtained from synthetic data. Beam forming was performed following the procedure described in section 6. Beams were calculated for a grid of $s_x$ and $s_y$ values and $s_z$ was obtained assuming a constant material velocity.

Synthetic traces were next calculated with a double couple source using *Fomosto* [Heimann et al., 2017]. The strike, dip and rake angles were set to 169°, 80° and -44° following

[Vavryčuk et al., 2013]. As a source location the receiver station V01 of the Rohrbach array was used and as receiver locations 17 of the 22 source array hypocentres (Fig. 14). The traces were bandpass-filtered from 1-20 Hz and normalized. The same velocity model as in section 6 was used for the calculation of the synthetic data (Fig. 19).

The semblance and maximum amplitudes of the stacked traces of the source array show a clear maximum for the direct P-phase (Fig. 15a). The best fitting result ($s_x$ = 0.13 s/km, $s_y$ = -0.05 s/km, $s_z$ = 0.10 s/km) corresponds to a back azimuth of 291° and an incidence angle of 125.45°. These results match well the theoretical travel path of the wave from V01 to the source array, since V01 is east-north-east of the array.

For solutions with positive $s_z$ values the maximum stacked amplitude is found for ($s_x$ = -0.15 s/km, $s_y$ = -0.08 s/km, $s_z$ = 0.029 s/km). However, the stacked amplitudes are clearly smaller than in case of a negative $s_z$. The true $s_z$ direction can therefore be distinguished. Fig. 16 shows the stacked traces for both, the best solution with a negative and a positive $s_z$ value. The stack is better for the negative $s_x$, which corresponds to the true travel path.

Fig. 17 shows empirical array transfer function, obtained from a 3-D slowness grid and synthetic traces. The colors indicate the stacked power. While the maximum values are well resolved in north-south direction ($s_y$), the east-west component ($s_x$) is less resolved. This shortcoming results from the elongation in north-south direction compared to small maximum interevent distances in east-west direction.

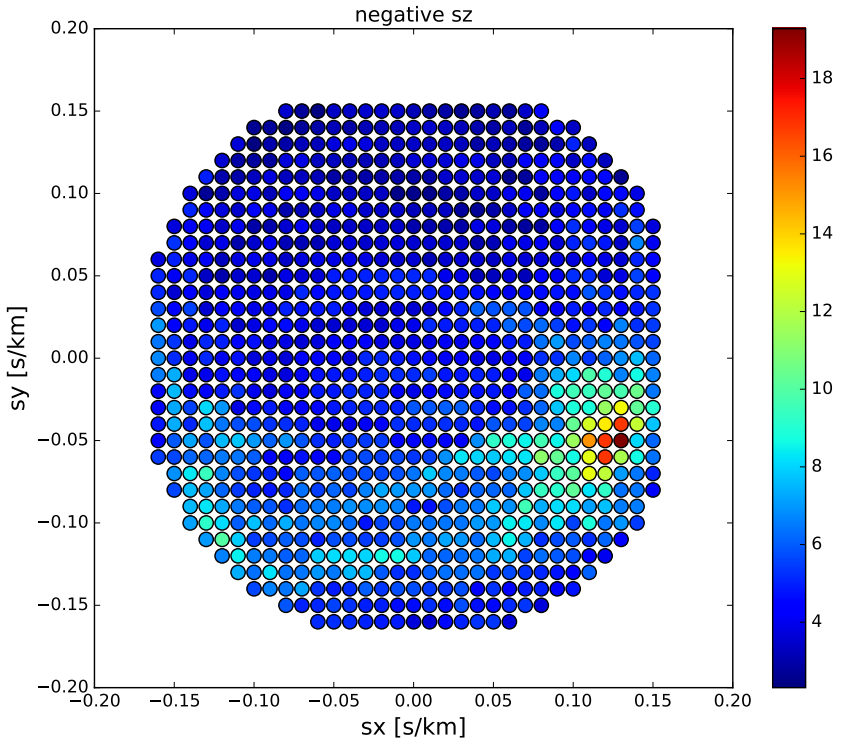


(a) Negative $s_z$.

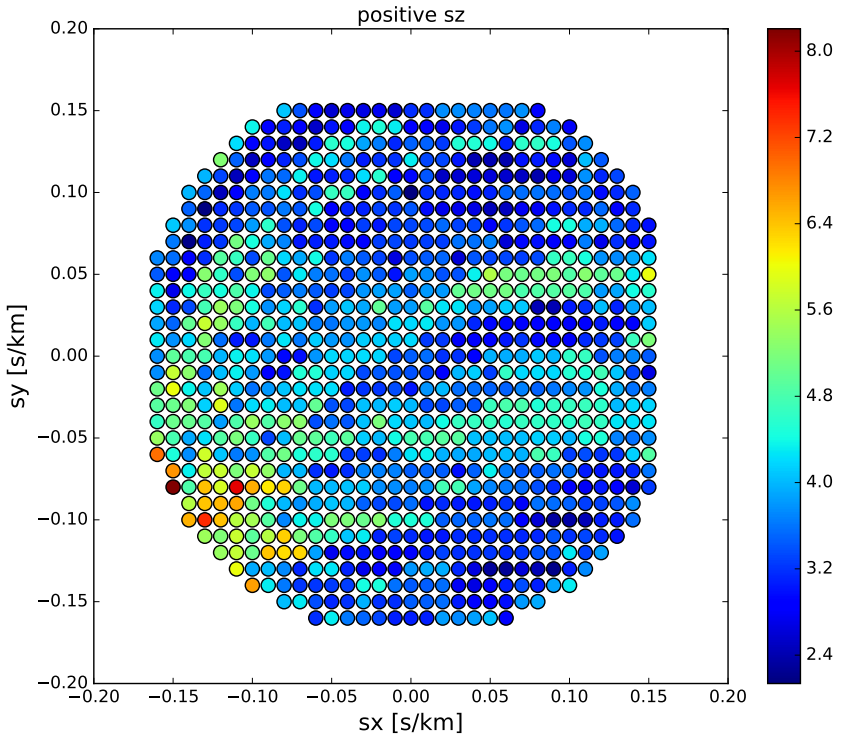


(b) Positive $s_z$.

Figure 15: Maximum amplitudes of stacks for direct P-wave. (a) Stack for the negative $s_z$ component, referring to the *true* solution. The maximal stacked amplitude is significantly higher then in case of a negative $s_z$ value (b). Fixed absolute velocity/ slowness.

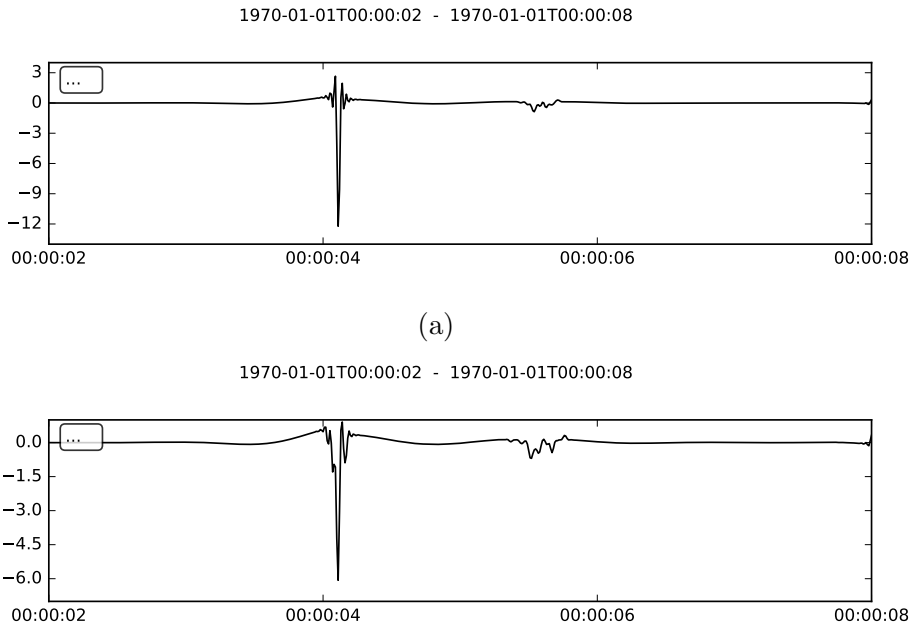


Figure 16: For comparison: (a) stacked synthetic traces for best fitting slowness vector and (b) SA traces stacked for best result with positive $s_z$-value (cf. 15). Traces were bandpass filtered before summation from 1 to 30 Hz.

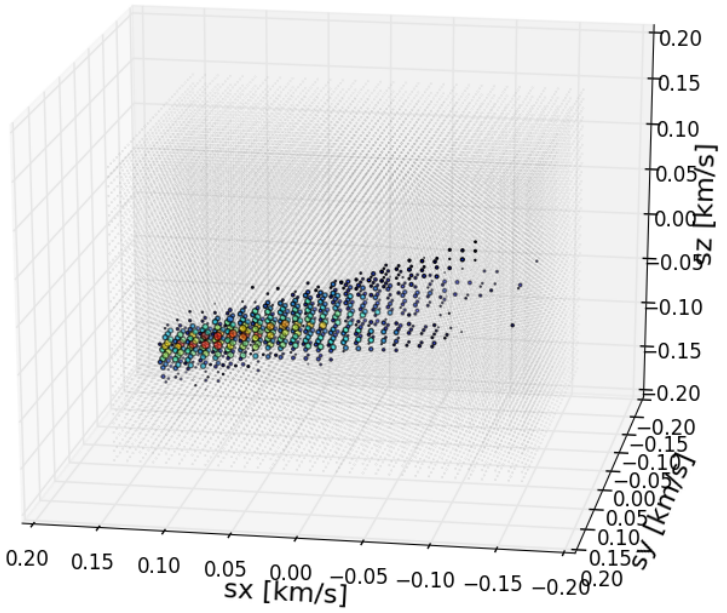


Figure 17: Stacked amplitudes in a 3-D slowness grid. The elongated shape points to the limited resolution in east-west direction due to the shape of the source array, being elongated in north-south direction.

# 6 Development of a source array beam forming method in time domain

Beam forming can be performed in time or frequency domain. In the beginning of this thesis, I decided to perform beam forming in time domain as described in section 4.1. Time domain beam forming is not only straight forward and more intuitive, but also very fast when no Fourier transform is necessary. However, in case of small distances between the events and the receiver stations, the data needs to be upsampled to enable small time shifts and for upsampling a Fourier transform is necessary. In frequency domain beam forming, upsampling is not necessary. In the end it might therefore be computationally more efficient. However, while in time domain beam forming the summation is performed on samples, in frequency domains time windows need to be chosen.

## 6.1 Development of a first beam forming algorithm

The python code for beam forming has been developed in two stages. At first, a simple code stacking the traces in loops over $s_x$ and $s_y$ was developed, assuming a fixed material velocity within the source array. This *warm-up* code was used for synthetic tests, showing that the principles of beam forming are understood and the code works fine. Afterwards, a new, much faster code was written, using the pyrocko function parstack [Heimann et al., 2017] and a 3-D slowness grid.

To perform beam forming shift times are calculated for a set of three dimensional earthquakes locations and potentially arriving plane waves defined by the slowness vector $\vec{s}$. The slowness vector $\vec{s}$ is composed of three components $s_x, s_y, s_z$. Under the assumption of a homogeneous velocity $v$, they can be written as:

$$s_x = 1/v \cdot sin(i) \cdot sin(baz), \tag{28}$$

$$s_y = 1/v \cdot sin(i) \cdot cos(baz) \tag{29}$$

and

$$s_z = 1/v \cdot cos(i), \tag{30}$$

with $baz$ being the back azimuth and $i$ being the incidence angle as defined in Figure 7 [Rost and Thomas, 2002]. $s_x$ points in east direction, $s_y$ in north direction and $s_z$ upwards (Fig. 18). Using the earthquakes as a source array is equivalent to thinking of a station as the source of a plane wave and the earthquake locations as recording stations. That is why the vertical angle of the beam is called incidence angle and not take-off angle. The travel time differences between a reference location $x_{ref}$ and all other locations $x_i$ for an

incident wave are calculated using the formula

$$dt_i = \vec{s}(\vec{x_i} - \vec{x}_{ref}) = s_x \cdot (x_i - x_{ref}) + s_y \cdot (y_i - y_{ref}) + s_z \cdot (z_i - z_{ref}). \quad (31)$$

The relative distances are converted from degree latitude and longitude to kilometres.

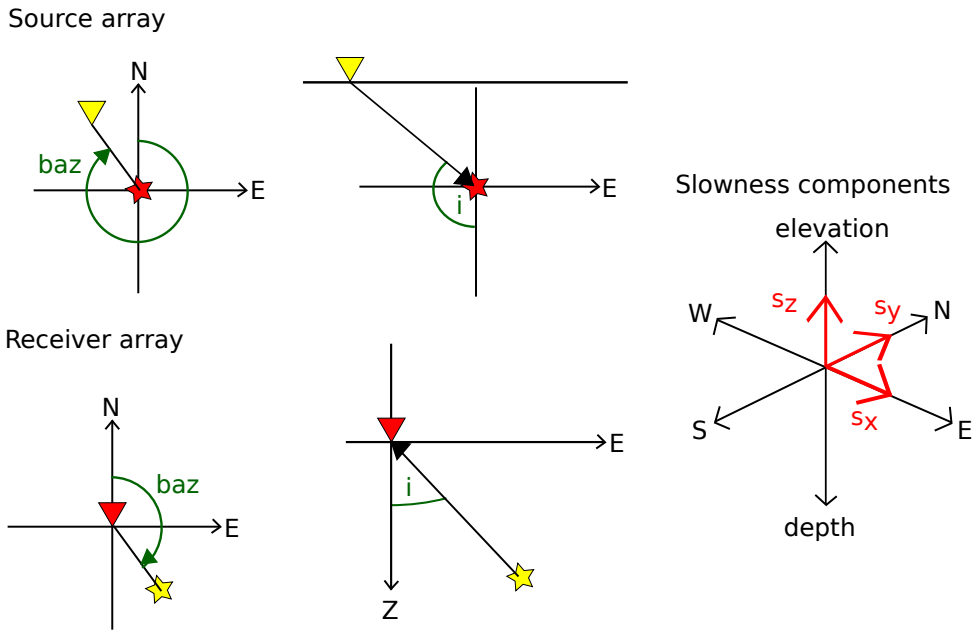


Figure 18: Definition of backazmiuth ($baz$), incidence angle ($i$) the three slowness components in source and reiceiver array geometry. In case of the source array, the incidence angle is the incidence angle of a hypothetical wave travelling from the receiver station to the array. In *normal* geometry, this angle would be called the take-off angle.

### Description of first beam forming code

ObsPy [Beyreuther et al., 2010] is used to read, filter and normalise the data. Afterwards the data is written into a NumPy array (ascii data). For the alignment of phases which generally have different arrival times at the stations (here: earthquake locations), the traces are shifted in time. In a $s_x$-$s_y$ grid implemented as *for*-loops, the time shifts are calculated using equation 31. $s_z$ is calculated from $s_x$ and $s_y$ assuming a fixed, homogeneous velocity for synthetic testing.

For synthetic testing, the full workflow ranging from the calculation of shift times to stacking is executed in a $s_x$-$s_y$ grid implemented with *for*-loops over $s_x$ and $s_y$ each varying from $-1/v$ to $1/v$ in steps of 0.01 s/km. In case of the first synthetic tests, the material velocity $v_P$ is kept constant, because it is known for the synthetic data. The vertical slowness component $s_z$ is calculated from $1/v = \sqrt{{s_x}^2 + {s_y}^2 + {s_z}^2}$. Both, positive and negative solutions for $s_z$ are used. To take into account unknown and differing phase velocities in case of recorded data, the beam forming algorithm is extended by a loop over

$s_z$ in section 6.3.

To evaluate the quality of the stacks the power in a defined time window of each stacked trace is calculated with:

$$P = \frac{1}{k} \cdot \sum_{k=0}^{K} {A_k}^2 \tag{32}$$

where A is the amplitude value of sample k and K is the length of the trace/ total number of samples within the time window.

## 6.2 Tests with synthetic data

### 6.2.1 Preparing synthetic data

Synthetic data was produced using the Fomosto software [Heimann et al., 2017]. Fomosto (*forward model storage tool*) is a tool for creating and working with Green's function databases. Ten independent Green's tensor components are calculated from which seismograms can be composed. Once the Green's function databases are calculated, synthetic seismograms can easily and quickly be calculated for different focal mechanisms. The databases can be shared and reused. Fig. 19 shows the velocity model which was used to calculate the synthetic data. Within the first testing process, explosion sources were used.

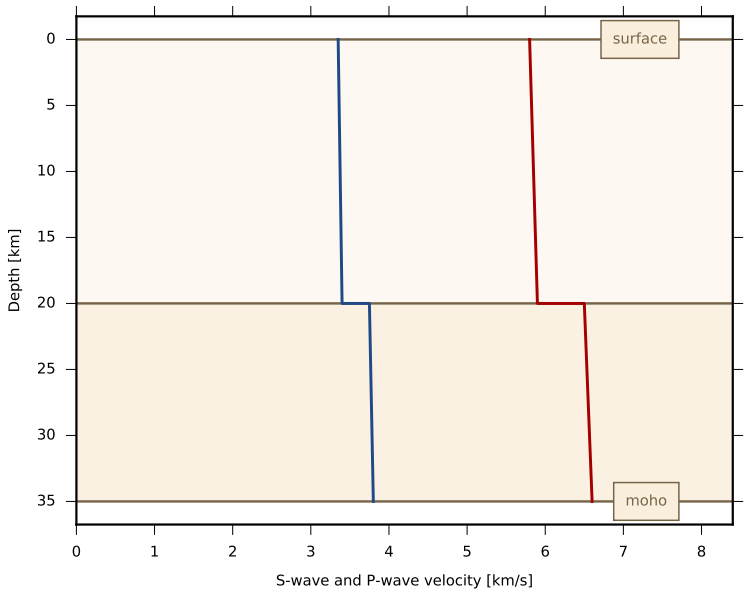


Figure 19: Velocity model used for the calculation of synthetic test data. Figure produced using cake [Heimann et al., 2017].

### 6.2.2 Testing with linear arrays

To test the stacking procedure five earthquakes are arranged first in a vertical and then in a horizontal line. In case of the vertical line, the station is set above the earthquakes, which are located at 6, 7, 8, 9 and 10 km depth (Fig. 20b). In the horizontal case, all earthquakes are located in 8 km depth on an E-W striking line with the station (Fig. 20a). The traces were bandpass filtered from 0-20 Hz and the amplitudes were normalized. Stacking was then performed as described in the previous subsections.

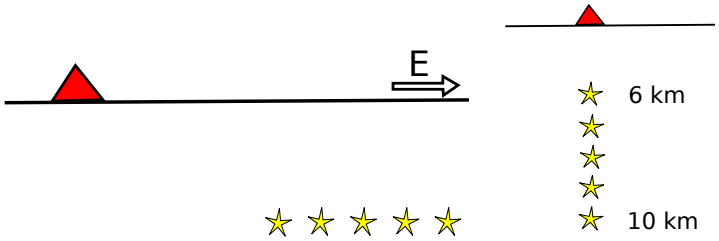


(a) Horizontal line. (b) Vertical line.

Figure 20: Test with earthquakes in a line.

Figure 21 shows the maximum stacked amplitudes in time windows around the onset of the direct P-wave for the horizontal and vertical line test cases. As expected, in case of the vertically arranged earthquakes the best stacks are achieved for maximum $s_z$ values. $s_y$ is zero, while $s_x$ is small since the station is slightly offset in x-component only. In case of the horizontal line, the results show the highest stacked amplitude for $s_x$=0.09, being independent of $s_y$ and $s_z$ ($d_y$=$d_z$=0). Negative $s_z$ values for a downward travelling wave are expected (in the source array the direct P wave is travelling from the station to the earthquake locations). Nevertheless, the same stacking results can be achieved with a positive $s_z$ when the recording station is underneath the earthquakes with the nearest earthquake location as reference.

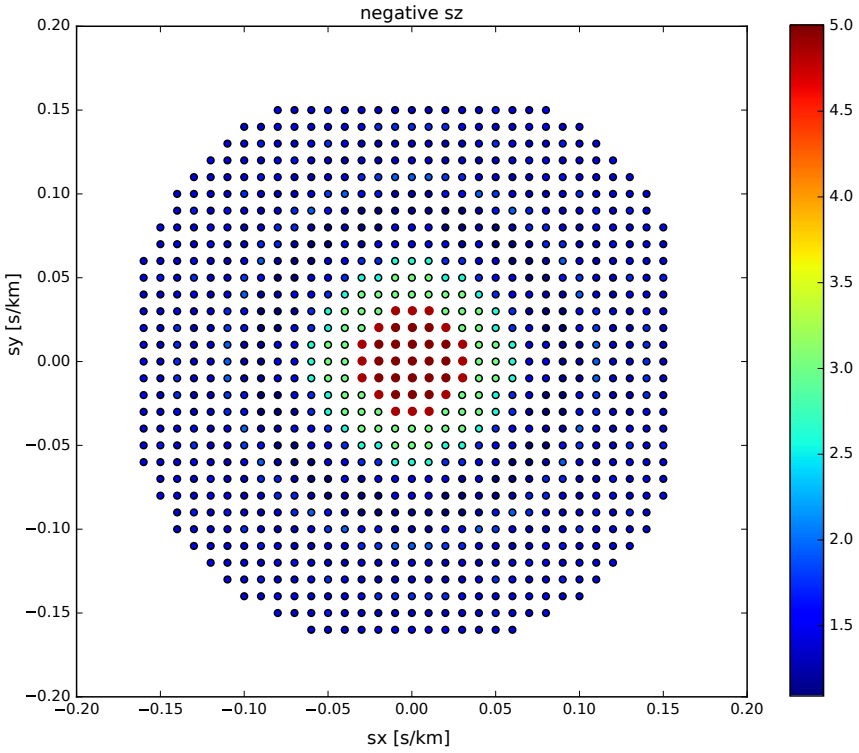


(a) $s_x$ vs. $s_y$, horizontal line.

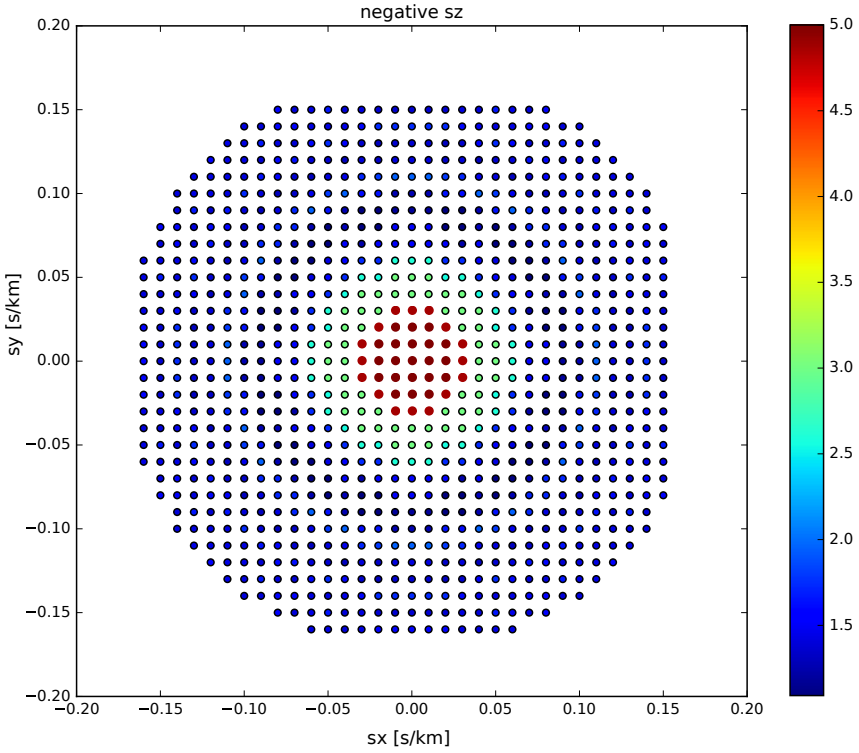


(b) $s_x$ vs. $s_y$, vertical line.

Figure 21: Maximum amplitudes of stacks for horizontal (a) and vertical (b) line.

## 6.3 Adaptation of beam forming code to recorded source array data

Contrary to synthetic data, in case of recorded data the material velocity in the source array region is not known but an additional objective. Therefore, the beam forming process described in section 6 is modified: $s_z$ is not calculated from $s_x$ and $s_y$ under the assumption of a known material velocity anymore but implemented as another *for*-loop. However, a constant (but unknown) slowness for the fault zone is still assumed.

The frequencies of interest of the Rohrbach Array lie between 10 and 40 Hz. Therefore a wide bandpass filter from 1-60 Hz is applied. To enhance the accuracy of the stacking process, the traces are upsampled from 250 Hz to 1000 Hz or 2000 Hz before stacking. Upsampling is performed with the function *scipy.signal.resample*. Resampling is performed in frequency domain. The Fast Fourier Transform of the signal is computed and zeros are added to the spectrum to reach the desired sampling rate. The higher sampling rate enables the implementation of very small and precise time shifts before stacking.

To save computation time, several major changes to the original python code (section 6.1) were made: First, the resulting beams are not saved as ObsPy traces anymore. Second, *parstack* by *pyrocko* [Heimann et al., 2017] was implemented. *parstack* is a python function which performs the beam forming in C. Among others, input parameters are the seismic traces, a shift table and weighting factors. In my script, the shift table is now calculated previous to the stacking in *for*-loops over $s_x$, $s_y$ and $s_z$. *parstack* then returns an array with summed amplitudes for each sample and each shift time. Every shift time corresponds to a slowness vector. In a loop over time windows of the beam with adjustable window length and step size, the amplitudes of all samples within the window are summed up and saved to a new matrix with the dimension $n(\vec{s})$ x $n(windows)$. For each window the maximum summed amplitude is searched as well as the corresponding indice which provides the slowness vector. The back azimuth and incidence angle are calculated from the slowness vector and plotted in an extra step. This workflow decreased the computation time from hours to few minutes only.

All shift times are calculated relative to the first event of the source array event list, number 88004344. For comparability, theoretical back azimuths are calculated using this event location. The entire workflow of source array beam forming is summarized in Fig. 22. All steps except the last two are performed within one python program (cf. appendix p. 90). The calculation of back azimuth and incidence angle are performed in another plotting program.

#### Alignment of traces relative to max. P amplitude

In case of imprecisely known origin times, the alignment of all traces with respect to the maximum amplitude of the direct P phase can remove uncertainties, if the P onsets are picked well and a velocity model is well known. P onset times are picked and the traces are afterwards delayed by delay times calculated from the product of distances and an imaginary plane wave travelling from the receiver station to the source array. This wave is described by a theoretical slowness $\vec{s}$ in x,y and z direction. For the calculation of the slowness vector (Formulas 28-30), the back azimuth and incidence angle of the direct P-wave are needed. The ObsPy function *obspy.geodetics.base.calc_vincenty_inverse* computes the distance and back azimuth between two geographic points on the WGS84 ellipsoid [Beyreuther et al., 2010]. The pyrocko package *cake* provides the incidence angle for a chosen velocity model [Heimann et al., 2017].

## 6.4 Adaption of beam forming code to receiver array

Modifying the source array beam forming program code for receiver array beam forming is straightforward, when geometrical constraints like the definitions of back azimuth direction and incidence angle are considered. For the interpretation, the limited resolution of the z-component of the slowness vector needs to be considered since the receiver stations are all located at the surface. To avoid solutions for waves coming from above the array (out of the air), the $s_x$-$s_y$-$s_z$- grid search is limited to negative $s_z$ values (upward travelling waves). The ambiguity is seen when the same maximum stacked power can be obtained from a high P wave velocity with a large incidence angle and a lower velocity with a steeper incising wave.

In order to test the implementation of the beam forming code for receiver arrays, beam forming was performed on synthetic traces with low-pass filtered peaks at theoretical P phase arrival times of event 88005106 at the Rohrbach Array stations. The geometrical back azimuth between receiver array station V01 and event 88005106 is 110.5°. The beam forming resulted in a back azimuth of 112.62°. An error of 2° is explained by the limited resolution due to a discrete $s_x$, $s_y$ and $s_z$-search grid and discrete time sampling.

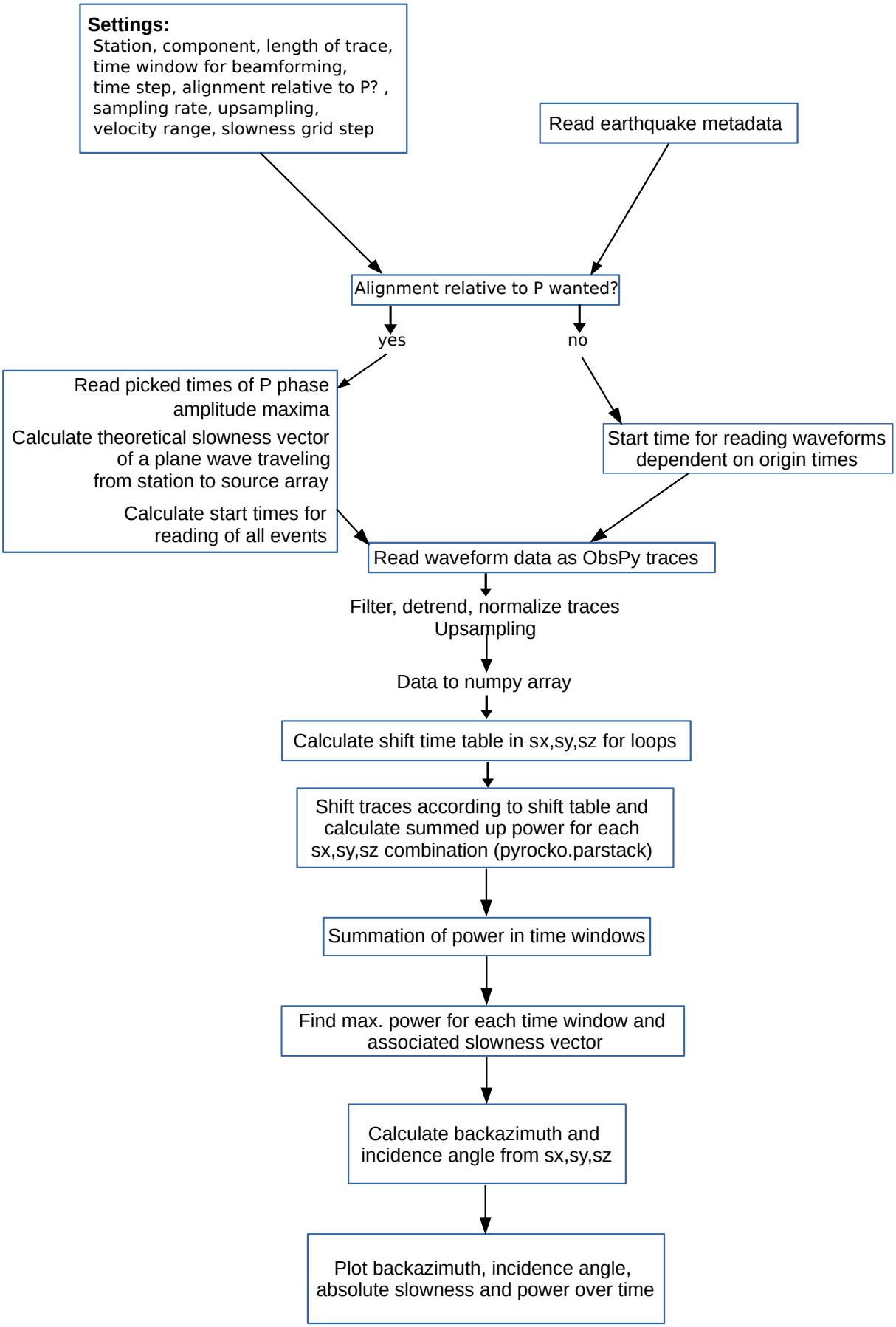


Figure 22: Workflow of source array beam forming.

# 7 Two methods for the determination of conversion locations

## 7.1 Analytical determination of conversion locations from beam forming results

From the back azimuths, the incidence angles (which are take-off angles from a normal perspective), the slowness/ velocity and the difference in travel time between a second converted phase and the direct P phase the location of a reflection or conversion point can be inferred, assuming constant homogeneous medium velocities for P and S waves and one single conversion/ reflection. Figure 23 shows a principle sketch of the problem. $\vec{a}$ is the vector describing the travel path of the direct P phase, $\vec{b}$ is the travel path between the location of the conversion and reflection and station V01 and $\vec{c}$ describes the path between hypocentre and conversion/reflection location. The angle $\beta$ is defined by the scalar product of $\vec{a}$ and $\vec{c}$:

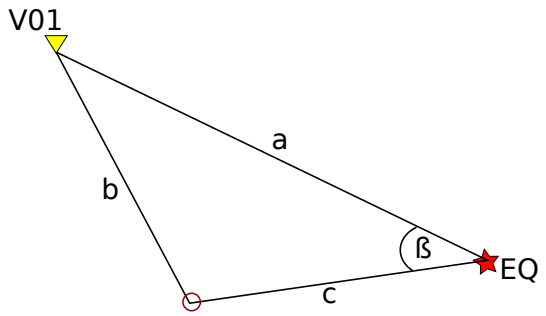


Figure 23: Geometrical constraints between direct P phase and another singularly converted or reflected phase. The illustration is shown in the plane that is held by the earthquake hypocentre, station V01 and the conversion/ reflection location.

$$\beta = acos(\frac{\vec{c} \cdot \vec{a}}{|\vec{c}| \cdot |\vec{a}|}). \tag{33}$$

Since $\beta$ is not dependent on the lengths of the travel path a or the partial travel path c, the equation can be simplified to

$$\beta = acos(\hat{c} \cdot \hat{a}), \tag{34}$$

where $\cdot$ implies the usage of the scalar product. By introducing polar coordinates, $\beta$ can be derived from the back azimuth and take-off angle (incidence angle of source array) of both faces. It holds that

$$\vec{a}, \vec{c} = \begin{pmatrix} x_{a,c} \\ y_{a,c} \\ z_{a,c} \end{pmatrix} \tag{35}$$

$$\text{with } x_{a,c} = r \cdot sin(i_{a,c}) \cdot cos(baz_{a,c}), \tag{36}$$

$$y_{a,c} = r \cdot sin(i_{a,c}) \cdot sin(baz_{a,c}) \tag{37}$$

$$\text{and } z_{a,c} = r \cdot cos(i_{a,c}). \tag{38}$$

$r$ is the radius (distance) from the event hypocentre which corresponds to the coordinate origin to either station V01 (for $\vec{a}$) or to the reflection point (for $\vec{c}$). The angle between the travel paths of the rays travelling from the source array reference event to a receiver station can be used to calculate the length of travel path $c$. Due to the law of cosine it holds that

$$b^2 = a^2 + c^2 - 2 \cdot a \cdot c \cdot cos(\beta), \tag{39}$$

with $a$, $b$ and $c$ being the lengths of $\vec{a}$, $\vec{b}$ and $\vec{c}$. With the help of the difference in travel time $dt$ between a converted/ reflected phase and the direct P phase, a third relation can be established:

$$\frac{a}{v_P} = \frac{b}{v_b} + \frac{c}{v_c} - dt, \tag{40}$$

where $v_b$ and $v_c$ are the velocities along path b and c (either $v_P$ or $v_S$). Rearranging and then squaring Formula (40) enables setting (40) = (39). This leads to

$$c^2 \cdot (1 - \frac{v_b^2}{v_c^2}) + c \cdot (2 \cdot \frac{a \cdot v_b^2}{v_p \cdot v_c} + 2 \cdot \frac{v_b^2}{v_c} \cdot dt - 2 \cdot a \cdot cos(\beta)) = \frac{a^2 \cdot v_b^2}{v_p^2} + 2 \cdot a \cdot \frac{v_b^2}{v_p} \cdot dt + dt^2 \cdot v_b^2 - a^2. \tag{41}$$

This formula can be solved using the general relation

$$uc^2 + vc + w = 0$$

$$\text{with solutions} \tag{42}$$

$$c_1 = -\frac{\sqrt{v^2 - 4uw} + v}{2u} \text{ for } u \neq 0 \tag{43}$$

$$c_2 = \frac{\sqrt{v^2 - 4uw} - v}{2u} \text{ for } u \neq 0 \tag{44}$$

$$c_3 = -\frac{w}{v} \text{ for } u = 0 \text{ and } v \neq 0 \tag{45}$$

[Merziger, 2010].

$u$, $v$ and $w$ can be written as:

$$u = 1 - \frac{v_b^2}{v_c^2}, \tag{46}$$

$$v = 2 \cdot \frac{a \cdot v_b^2}{v_p \cdot v_c} + 2 \cdot \frac{v_b^2}{v_c} \cdot dt - 2 \cdot a \cdot cos(\beta) \tag{47}$$

$$\text{and } w = -(\frac{a^2 \cdot v_b^2}{v_p^2} + 2 \cdot a \cdot \frac{v_b^2}{v_p} \cdot dt + dt^2 \cdot v_b^2 - a^2). \tag{48}$$

Depending on the velocities along a and c (both either $v_P$ or $v_S$) the resulting formula can be simplified. In case of a PP reflected phase equation 45 can be applied to obtain

$$c = \frac{-dt^2 \cdot v_P^2 - 2a \cdot dt \cdot v_P}{-2a - 2dt \cdot v_P + 2a \cdot cos\beta}. \tag{49}$$

$c$ is the distance from the hypocentre to the conversion/ reflection point. For SP and PS phases two solutions $c_1$ and $c_2$ are found. To decide which solution is the appropriate one, $c_1$ and $c_2$ are entered into equation 40 to compute b:

$$b_{1,2} = \frac{a \cdot v_b}{v_p} + dt \cdot v_b - \frac{c_{1,2} \cdot v_b}{v_c}. \tag{50}$$

The overall travel time along path $c + b$ is given by

$$t_{ges_{1,2}} = \frac{c_{1,2}}{v_c} + \frac{b_{1,2}}{v_b}. \tag{51}$$

The better solution is the one for which $t_{ges} - t_{xx}$ is closest to zero. This is tested in a forward calculation. $t_{xx}$ is the arrival time of the converted phase.

Combining $c$ with the back azimuth and incidence angle provides a unique description of the position of the conversion/ reflection point. The relative coordinates of the reflection/ conversion point are defined through

$$x = c \cdot sin(i) \cdot cos(baz), \tag{52}$$

$$y = c \cdot sin(i) \cdot sin(baz) \tag{53}$$

$$\text{and } z = c \cdot cos(i), \tag{54}$$

where $x$ is in east-west direction, $y$ in north-south direction and $z$ describes the depth.

The shortcomings of this method are the assumption of a homogeneous velocity along the travel path and that it cannot be used in direct vicinity of the source (or receiver) array where the plane wave assumption is violated.

#### Testing with fixed point below receiver

Synthetic traces were calculated for P and PP, SP and PS waves travelling from the 22 earthquake locations to receiver station V01. Low-pass filtered peaks are set at the theoretical arrival times of the phases (Fig. 24). Thereby the arrival times of the converted phases are calculated for a homogeneous velocity model along the travel path in a 3-D

medium. Beam forming is performed on the traces and the results are presented as back azimuth, incidence angle and absolute value of slowness in 0.05 s long time windows (Fig. 25).

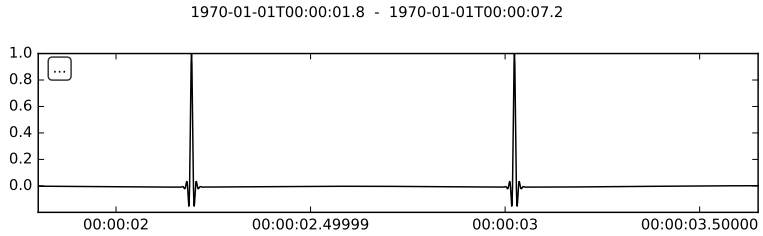


Figure 24: Synthetic trace with low-pass filtered spikes at P and SP arrival times. Calculated for a conversion in 5 km depth and source location of event 88005410 (2008-12-09 04:49:16.120 M -0.1), recorded at station position V01. A homogeneous velocity model was assumed.

In the test case presented here the position of the conversion/reflection point was set to 5 km depth, since Hrubcová et al. [2016] described a potential reflection layer in 3-6 km depth. The horizontal position was chosen more or less arbitrarily to lie between the source array and station V01. Beam forming provides the back azimuth, incidence angle, absolute slowness and time difference between the second phase and the direct P phase. Figure 26a shows the conversion point which was obtained from the read off values, along with the originally assumed point, for which the synthetic traces were calculated. The location difference is 485 m in E-W, 2 m in N-S and 420 m in depth for the SP phase. For the PS case the location errors are 405 m in E-W, 61 m in N-S and 278 m in depth. For the PP case the location was clearly unfavourably chosen, since the arrival times of P and PP differ by less than 0.06 s. Thus the location could not be derived properly. All location errors are explained through the limited resolution of the back azimuth and incidence angle obtained from the slowness vector in the beam forming procedure.

In a second test case the conversion point was chosen to lie further outside the direct line between epicentre and recording station (Fig. 26b). Location errors of up to 300 m in E-W direction and less than 100 m in N-S direction were found. The depth error depends crucially on the determined incidence angles. Errors between 1 m and 99 m were obtained for the different phases PP, SP and PS. Overall the location errors of several tests with synthetic data are less than 5 %.

Playing around with the back azimuth and incidence angle provides more insight into the dependence of the locations on correct readings. In the second test case a variation of the incidence angle by 1° leads to a depth change of almost 250 m. Changes introduced by a 1° difference in back azimuth are here in the order of 100-200 m in horizontal directions. The results of the synthetic test show that even in a synthetic test case with spike-like

signals the resolution of the beam forming process is limited due to the chosen grid spacing of the slowness vector. The results strongly dependent on the exact determination of the back azimuth and the incidence angle. While the N-S direction is generally well resolved due to the elongated source array, E-W and depths strongly depend on correctly obtained readings.

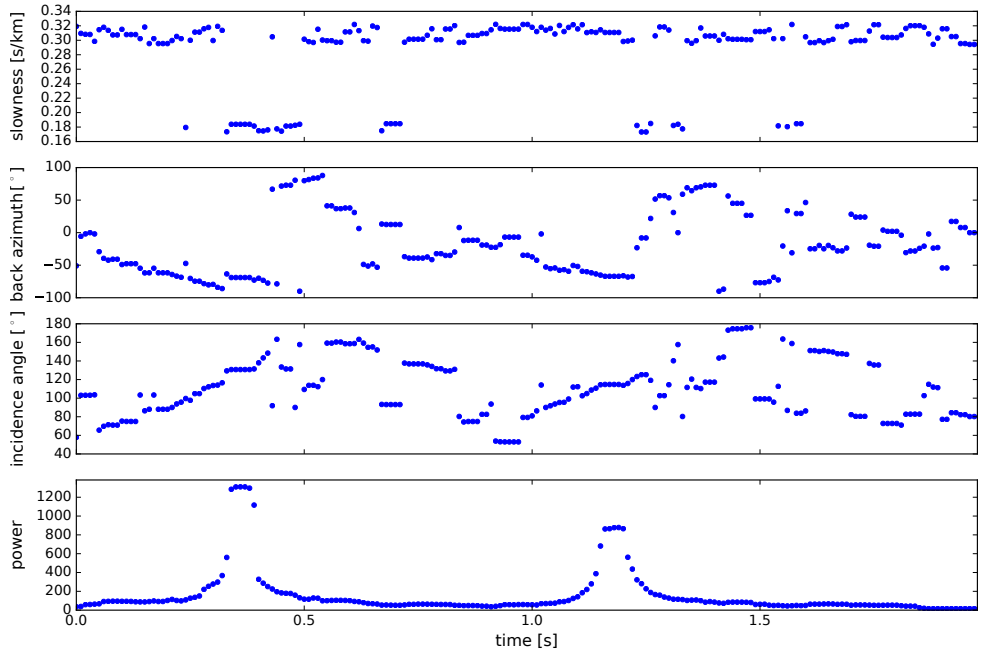


Figure 25: Beam forming result of 22 synthetic traces with P and SP onsets, calculated for a conversion in 5 km depth (cf. Fig. 24).

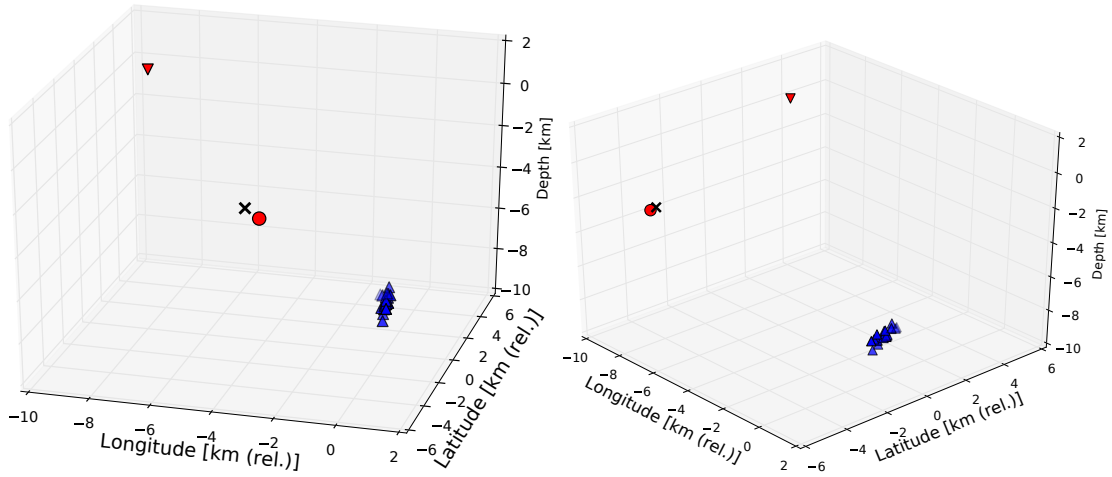


Figure 26: Conversion points obtained from beam forming (big red circle) along with true position of conversion points (small red circle) for which synthetic traces were calculated. Latitude and longitude are in km relative to the centre event of the source array. Two test cases, both S to P conversions calculated for a homogeneous velocity. Location errors are in the order of up to 500 m.

## 7.2 Grid search for conversion locations

A tridimensional grid search was chosen as a second approach to determine conversion locations. Assuming singular converted phases like SP and PS, for a conversion at each grid point the arrival time of a phase travelling from the epicentre to the grid point and further on to the receiver is calculated. In chosen time window around the theoretical arrival time the beam power is calculated. The beam power of conversions at each grid point are plotted with scaled color and symbol size. In case of a phase originating from a conversion at a certain grid point, the beam power should be much higher than for other grid points. Regions with a high probability of phase conversions can be recognised and estimates on the spatial resolution of the conversion locations can be made.

The grid search is implemented in *for*-loops over latitude, longitude and depth with respect to reference event 88004344. For each point in space, the theoretical arrival time of a phase being converted here is calculated. *cake.arrivals* [Heimann et al., 2017] is used to calculate the travel time of the converted phase, using the velocity model presented in Hrubcová et al. [2016]. In order to do this, the travel path is split into to parts: The first path between hypocentre and conversion grid point and the second path between conversion grid point and receiver. In case of the source arrays for each single earthquake hypocentre the travel time to the conversion point is calculated assuming a receiver at the depth of the conversion point. The travel time from the conversion point to a receiver station is calculating assuming a source at the conversion point. Both parts are summed up.

After the calculation of the complete travel time of the first event's phase, calculations only continue when the complete arrival times lies within previously defined limits. When the direct P and S phases are included in the search, the power search is dominated by those conversions which are in the direct vicinity of the source array and resemble the direct phases the most. Temporal boundaries can be set with respect to the direct P and/or S wave arrival times or by entering concrete values.

A grid spacing of 500 m or 250 m is used when a large (e.g. 15 km * 15 km * 12 km) search space is evaluated, without narrow time limits. However, when a phase is visible in the beam forming results, the search can be restricted to a time window around the observed phase. Additionally the search space can be restricted to an area which fits the observed slowness vector from the beam forming results. Then a very fine grid spacing can be chosen. The time window for beam forming needs careful adjustment.

Figure 27 shows the result of a grid search using synthetic data. For a fixed conversion point (black cross) synthetic traces with peaks at P and PP arrival times were calculated. The grid search was performed using a large grid covering a volume of -9 to +5 km in longitude, -5 to +5 km in latitude and 2 to 6.5 km in depth with respect to reference

event 88004344. A grid spacing of 500 m was chosen to save computation time and the beam forming time window was 0.02 s long. The originally assumed conversion location was determined with errors of 0.2 km in Latitude and 0.5 km in depth and longitude. In a second step, the search space was narrowed down and a spacing of 100 m was used. Using a smaller grid spacing improves the results to about 0.1 t 0.2 km.

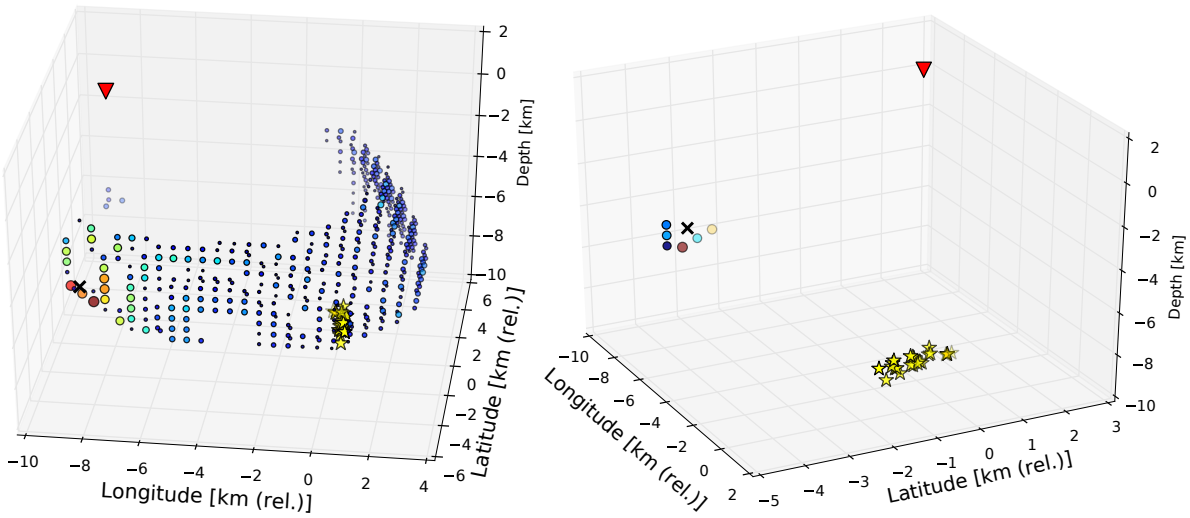


(a) (b)

Figure 27: Location grid search result, synthetic test. Time window: 0.02 s, grid spacing: 500 m, grid area covering lon: -9 to +5 km, lat: -5 to 5 km, depth: 2 to 6.5 km. Black cross: true conversion location. Symbol size and color are scaled to power. Red indicates highest power, only grid points associated with grid power above 5 % (a), respectively 66 % (b) are shown. Highest power grid point deviates by 0.5 km in longitude, 0.2 km in latitude and 0.5 km in depth from true location. With smaller grid spacings, the errors can be decreased.

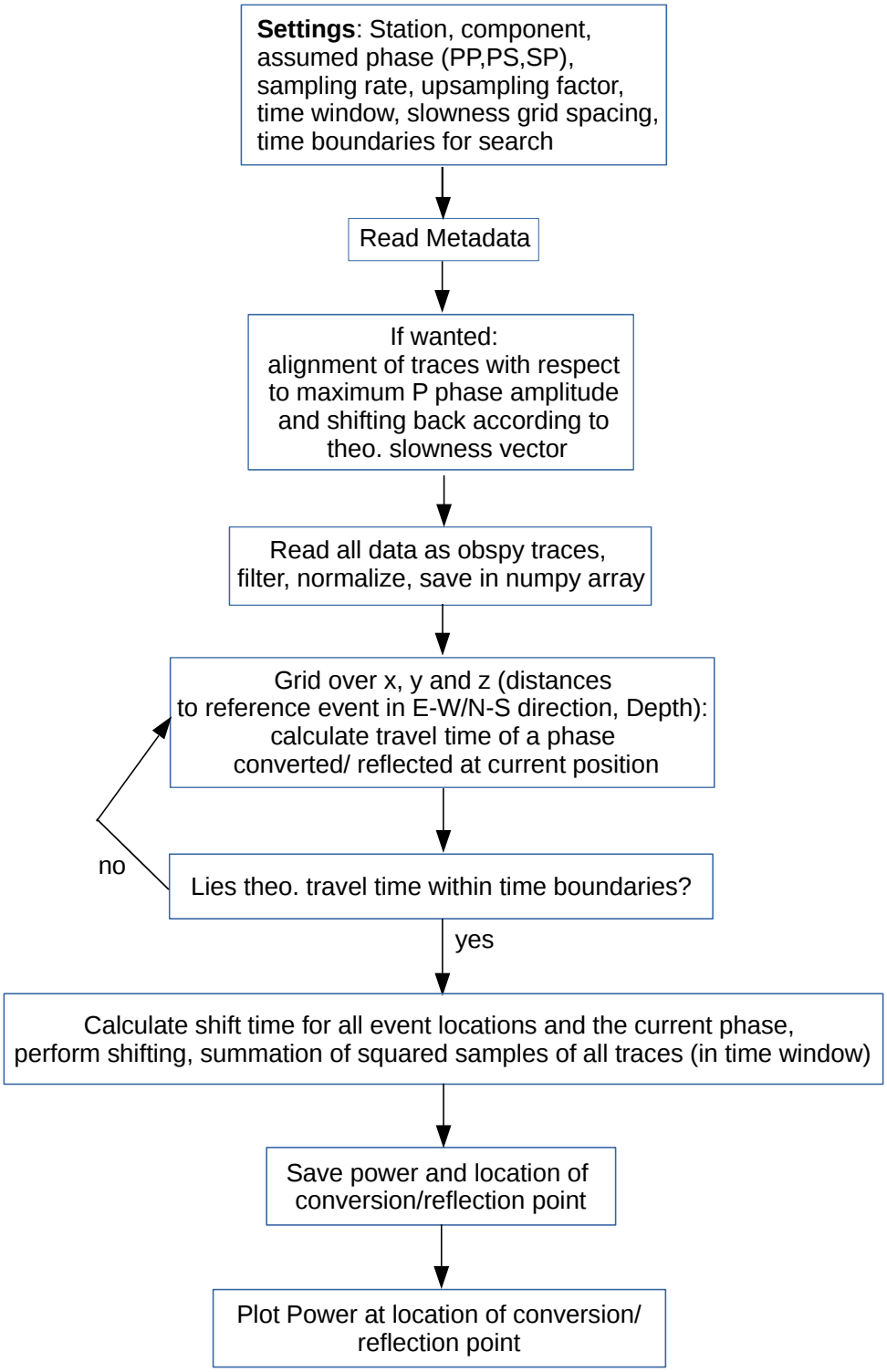


Figure 28: Workflow of grid search method.

# 8 Evaluation of prerequisites of source array beam forming

## 8.1 Waveform similarity - comparison between source and receiver array

The successful application of beam forming on source array events requires a certain degree of waveform resemblance. The similarity of waveforms can be inspected visually and quantified by calculating cross-correlation coefficients. In a first attempt, the similarity of the z-components of all events recorded at station V01 was controlled visually and compared with the recorded traces of single earthquakes at all stations of the Rohrbach Array (e.g. Figures 30 and 31). All traces were filtered with a wide recursive bandpass filter from 1 to 60 Hz. The P phases of all events recorded at V01 are remarkably similar (source array). Comparing different stations for event 88005274 does also show great similarities, however, V12 shows significant differences (higher frequencies) as well as V10 which has a wider maximum (receiver array).

The visual impression was quantified by calculating cross-correlation coefficients. The ObsPy function *xcross* calculates normalized cross-correlation coefficients in time domain while shifting the two traces relative to each other [Beyreuther et al., 2010]. All traces were bandpass filtered from 1 to 60 Hz and the amplitudes were normalized in order to compare events of different magnitude. The shift value for which the highest cross-correlation coefficient is obtained is returned as well as the coefficient itself. Adjustable parameters are the maximum number of samples to shift and the complete time window to consider. In a time window starting 0.2 s before and ending 0.2 s after the picked P onsets, the cross-correlations coefficients were calculated in time windows of 0.26 s length, shifted by max. 36 samples.

The source array generally shows higher cross-correlations than the receiver array (cf. Fig. 29). This holds not only for the records of receiver station V01 but for all stations except station V12, where the waveforms differ significantly between different events. Fig. 32 shows that in case of receiver station V12, the waveforms are more complex. Small temporal changes of the waveforms are seen, e.g. the waveforms of the events occurring between 2008-11-03 and 2008-12-09 show higher resemblances (cf. also sec. 9.6). The signal to noise ratio does not show a clear temporal trend.

Waveform differences between the recordings of the receiver array stations can most likely be explained by heterogeneities directly below the stations. The observed smaller cross-correlation coefficients within the receiver array indicate a heterogeneous subsurface in the receiver array area, while the source array volume appears to be more homogeneous. The resolution of heterogeneities depends on the frequencies that can be resolved by the source and receiver array. Even for a bandpass range of 1-100 Hz the cross-correlation coefficients on some stations are unexpectedly high (Appendix p. 94). The

cross-correlation coefficients of both, source and receiver array, are increased, when the frequency bandwidth of the signal is decreased (cf. Appendix p. 94 and following).

Due to the described great similarities between different events observed at the same station, as described above, the usage of a source array provides great possibilities for structural analysis not only for this thesis but also for future applications.

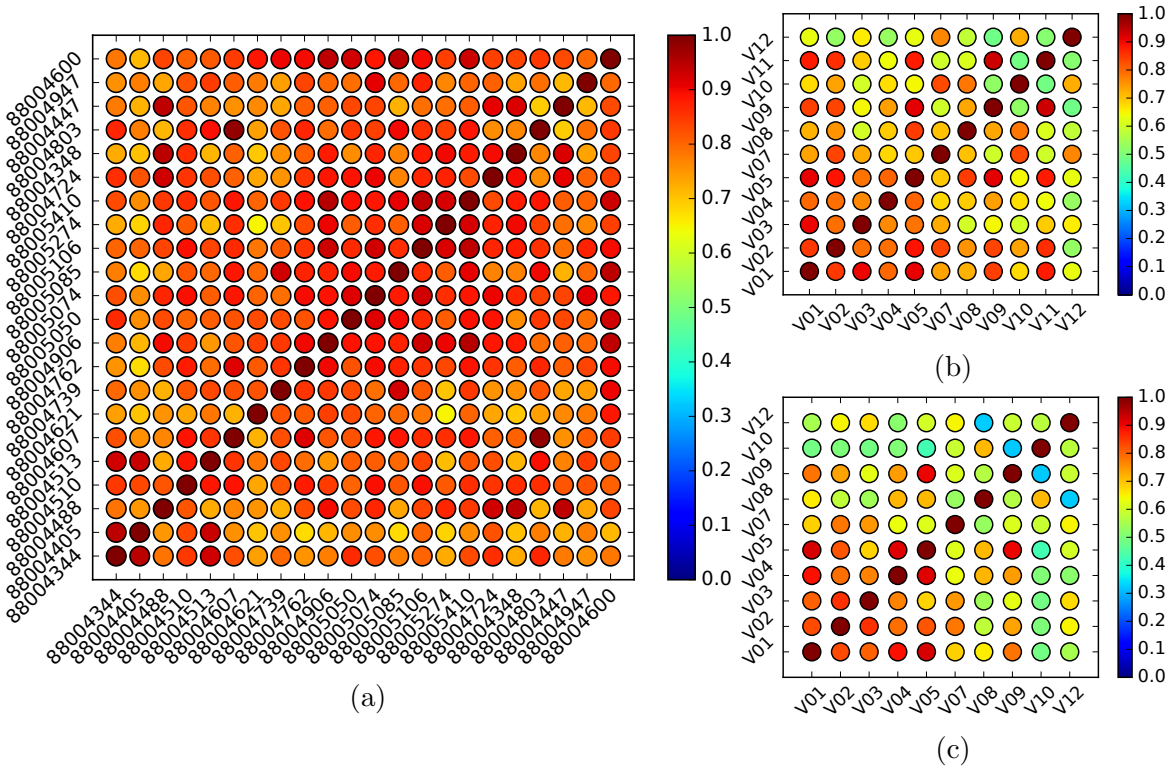


Figure 29: Maximum cross-correlation coefficients for source array recorded at station V01 (a) and for receiver array recordings of events 88004621 (2008-10-28 10:08:05.020 M 1.5)(b) and 88005106 (2008-11-08 23:11:55.240 M 0.4) (c), obtained in ±0.2 s time windows around the picked P onsets. Traces were normalized and bandpass filtered (1-60 Hz).

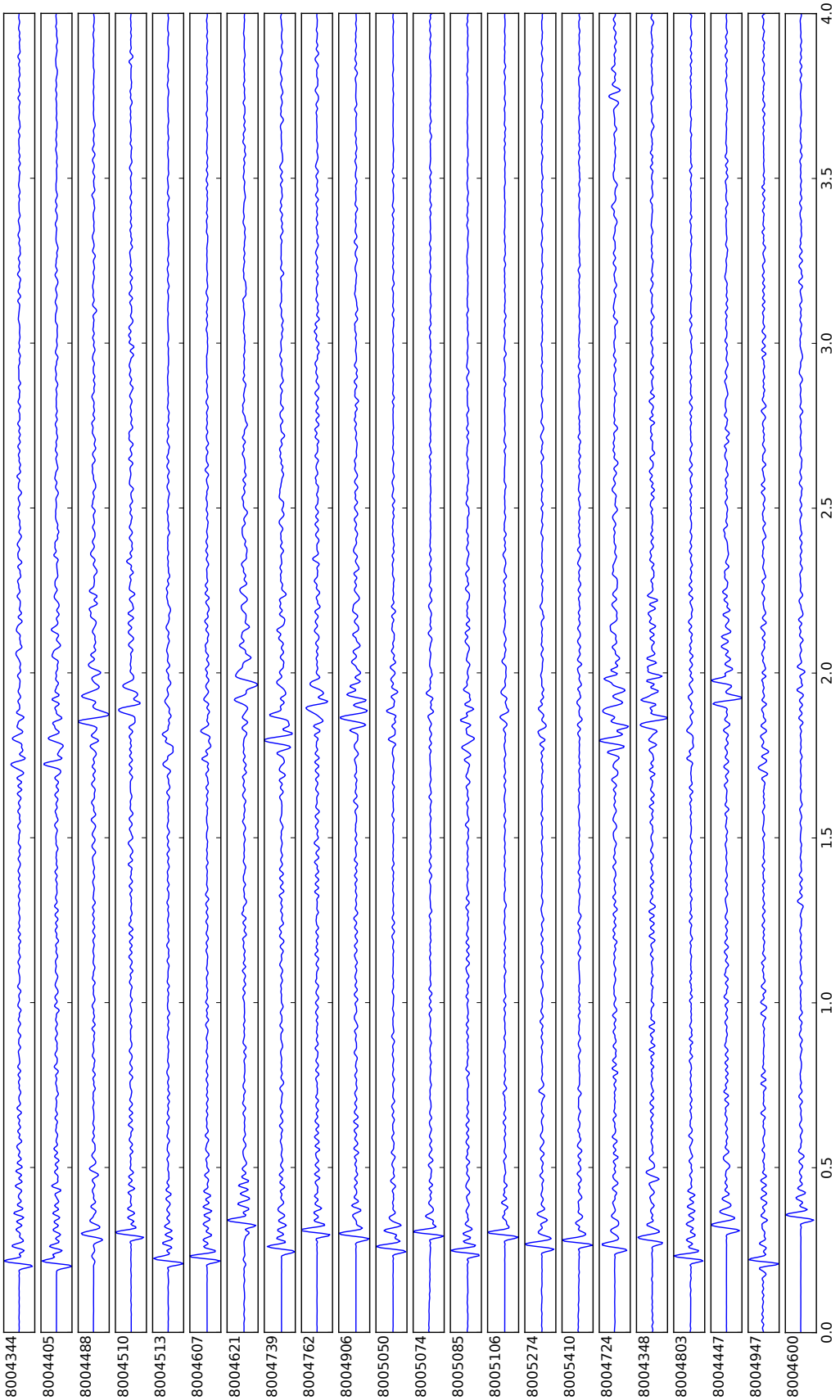


Figure 30: Source array events recorded at station V01 of the Rohrbach Array, bandpass filtered (1-60 Hz). Time 0.0 s corresponds to 1.8 s after the origin time of each event. The P phase waveforms are notably similar.

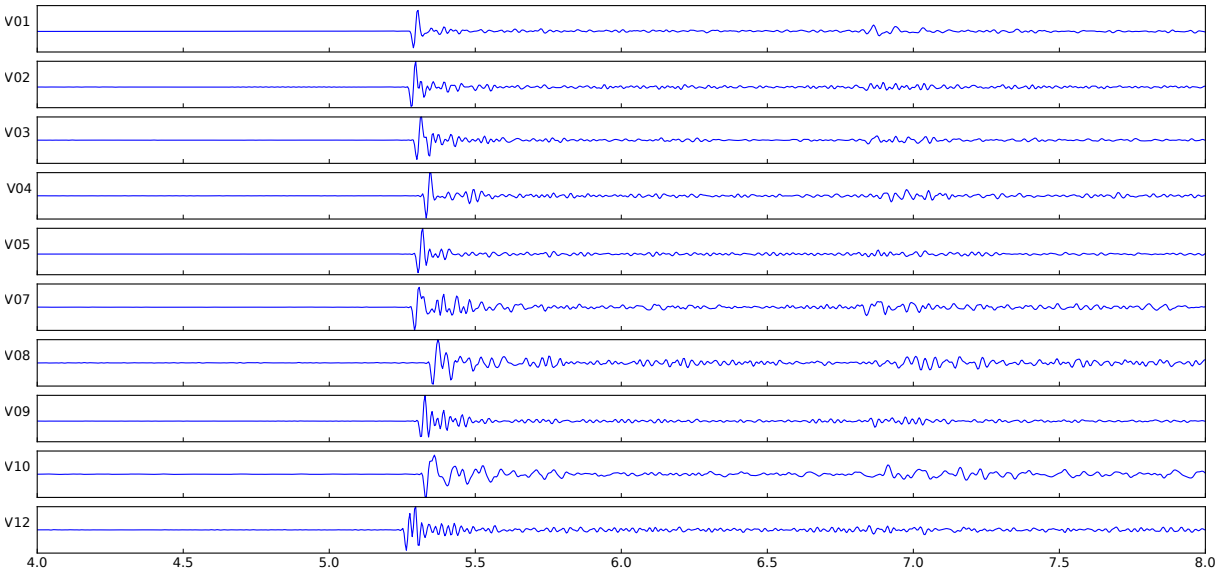


Figure 31: Receiver array recordings for event 88005106 (2008-11-08 23:11:55.240, M 0.4).

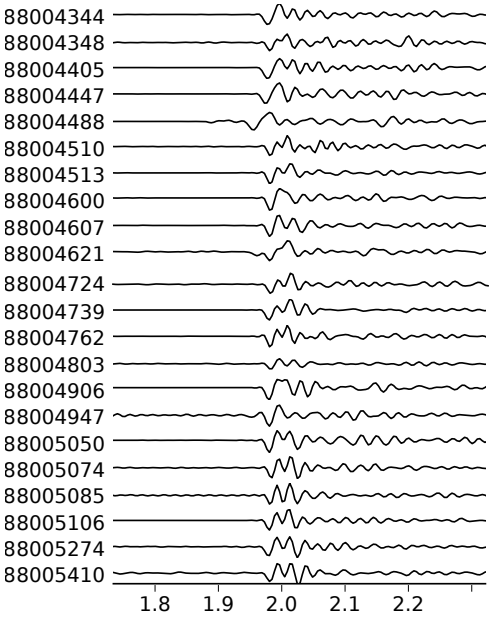


Figure 32: Small extract of source array events recorded at station V12 of the Rohrbach Array, bandpass filtered (1-60 Hz). Events are shown in temporal order.

## 8.2 Origin times and locations

Knowledge of precise (relative) origin times and earthquake locations are necessary for source array beam forming. According to Fischer et al. [2010] the event catalogue provides the hypocentres with uncertainties of 100 m. The quality of the origin times and locations from the catalogue was determined by calculating the residuals between theoretical and

picked P onset times. P arrival times $t_{P,obs}$ of three earthquakes on all Rohrbach stations were picked manually using *snuffler* [Heimann et al., 2017]. From the provided source and receiver locations the hypocentral distance was calculated. Using a range of reasonable mean material velocities along the travel path, theoretical arrival times $t_{P,theo} = dist/v_P$ of the P phase were calculated. $r_i = t_{P,obs} - t_{P,theo}$ provides the residuals for each station (e.g. [Havskov and Ottemöller, 2010]).

In case of a significantly wrong event location, the velocity associated with the minimum residuals would differ from station to station. If the origin time of one of the evaluated events was wrong, the velocities to achieve minimum residuals would be the same on all stations recording that event, but significantly different to the velocities used for other events.

In case of the three evaluated earthquakes, the smallest residuals were found for velocities of about 5.625 km/s (e.g. 33). Neither significant differences for the different stations recording one event nor between the different events themselves were observed. (However, when events with significantly different depths are compared, the velocity associated with minimum residuals shows depth-dependences (cf. sec. 8.3).)

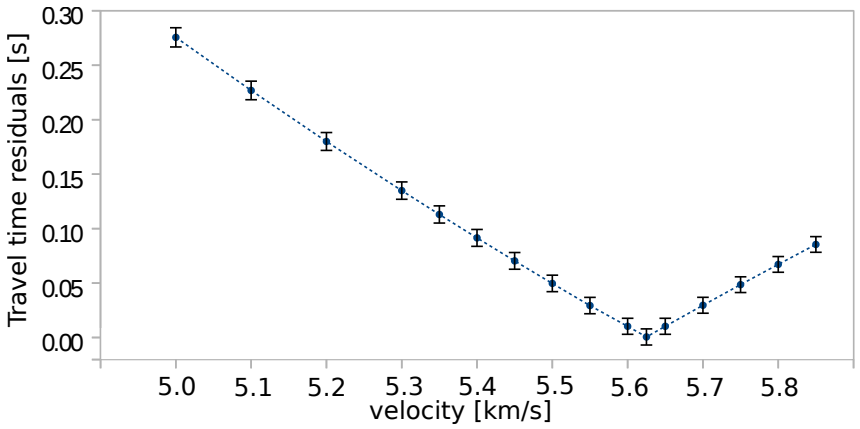


Figure 33: Event 88004344 (2008-10-20 11:17:56.380 M 0.9). Mean of residuals from all stations for different velocities. A minimum is found for 5.625 km/s. The error bars show the standard deviation.

Residuals were usually clearly below 0.01 s and a common minimum was generally found for all stations accept V02 and V10. For V02 slightly faster velocities (+0.025 km/s) and for V10 slightly lower velocities (-0.025 km/s) are associated with the minimum residuals between theoretical and picked onset times.

The obtained velocity is the mean velocity along the complete travel path, assuming a homogeneous material. In reality, the material is not homogeneous and therefore the obtained velocity has no true geological meaning. From section 8.3 velocity changes with depth can be inferred. For better understanding of the subsurface velocity distribution,

*cake* [Heimann et al., 2017] was used to compare theoretical arrival times of the direct P phase obtained from published velocity models of the area with the picked P phase arrival times (cf. sec. 9.1).

## 8.3 Homogeneous velocities within the source array

A homogeneous velocity within the 3-D source array is assumed to simplify the beam forming process. In the more common case of receiver arrays this prerequisite is met when the stations are not varying significantly in depth and are located within the same geological unit.

In case of a source array the same holds for horizontal location differences, but additionally significant differences in depth are necessary to enable a 3-D analysis with direct resolution of the $s_z$ slowness component. This leads to weighting up the desired vertical aperture against an acceptable velocity variation.

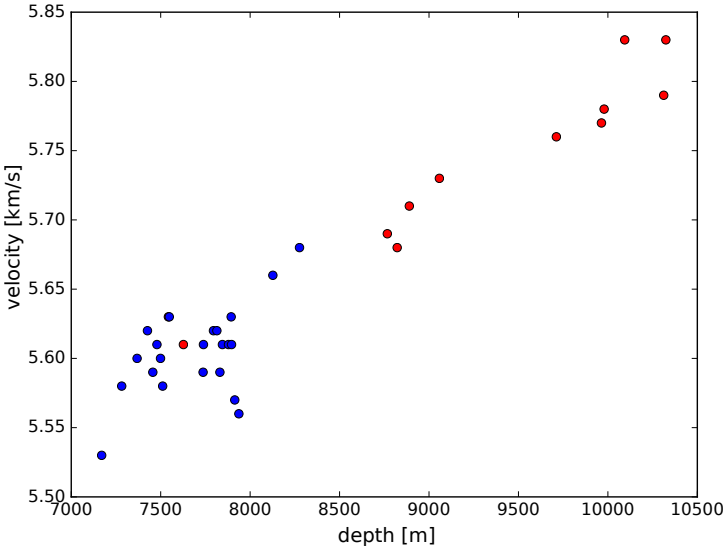


Figure 34: Mean velocity along the travel path associated with min. residuals between obs. and theo. P phase arrival times vs. depth of events, blue: Source Array, red: additional events.

According to Figure 3, the Nový Kostel focal zone lies in two structural units, the crystalline rocks of the Erzgebirge in the East and a sedimentary unit in the West. In order to evaluate the effect of this geological change observed at the surface, the residuals (difference between observed and theoretical arrival times) between station V01 and all earthquakes of the source array were calculated for different velocities (Appendix, Fig. 48). Likewise, eleven additional, mainly deeper events are treated in order to detect a dependence of depth. The velocities are the mean velocities along the travel path of the direct P phase. The velocities associated with the minimum residuals are in the order of 5.53 to 5.76 km/s for the events of the source array. Small deviations are noticed for the different events, but no dependency on the longitude (or latitude) is observed (Fig. 35). The source array is, however, elongated in north-south direction and varies in east-west direction by only about 550 m. While no horizontal trend in velocity is observed, the mean travel path velocities show a general trend with respect to depth: The deeper the earthquake, the higher the velocities associated with the lowest residuals (Fig.

34). This is not surprising, since a material velocity increase with depth is common. In section 9.1, velocity models for the source region are presented. According to Málek et al. [2005] velocities between 5.8 km/s and 6.1 km/s are observed in 2.5 to 8.4 km depth. In a second model, a P wave velocity of 5.3 km/s is assumed for depths below 5 km and 6.3 km/s for 5 to 12 km depth. A model similar to the two presented models was likely used to obtain the catalogue locations.

The increasing velocity with depth has to be taken into account as an error source. In case of the source array used here, a homogeneous velocity is still assumed. However, for future work and especially when using larger source arrays, the velocity variability within the array needs to be further addressed.

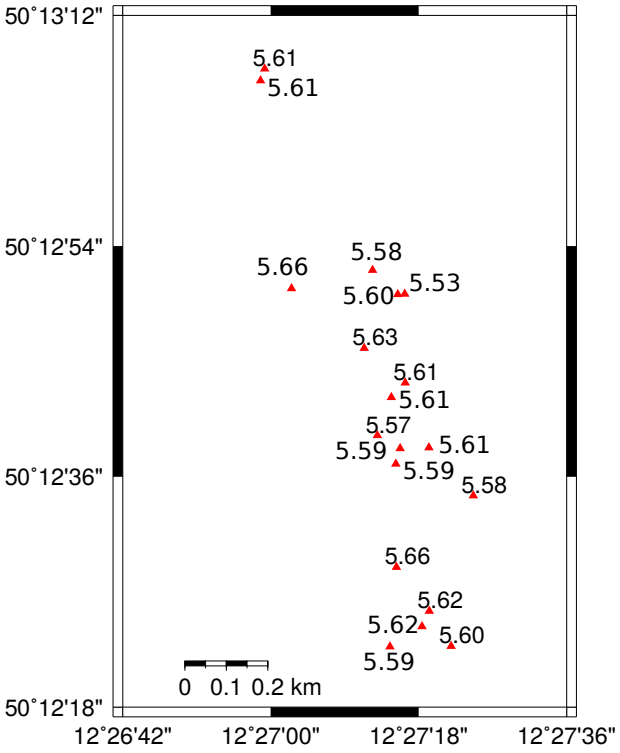


Figure 35: Map showing epicentres of source array events along with the travel path velocities associated with the minimum residuals. No trend in NS or EW direction is observed.

# 9 Source array analysis: Results and Interpretations

Source array beam forming was performed on the previously presented 22 source array events recorded on the stations of the Rohrbach receiver array.

Stacked power was calculated for $s_x, s_y, s_z$ combinations in a velocity range between 3.5 and 7 km/s on vertical and horizontal components of all Rohrbach stations (grid spacing 0.2 s/km). Additionally, for P wave velocities between 5.5 to 7 km/s a smaller grid spacing (0.1 s/km) was chosen to improve the resolution. Before restricting the velocity range, velocities between 2.8 and 8 km/s were tested. An optimal time window length of 0.05 s with steps of 0.01 s was determined empirically.

In the first subchapter, the arrival times of the direct P phases are compared to arrival times calculated with two different velocity models (Sec. 9.1). The sensitivity of the beam forming results towards location errors is tested in Sec. 9.2. Afterwards, the beam forming results both dependent and independent of origin times are compared and interpreted (Sec. 9.3 and 9.4). Then some deeper events are used as a new source array to analyse structural phases directly visible in the waveforms of deep ($> 9$ km) events only (Sec. 9.5). Based on the beam forming results and the recorded waveforms, the Rohrbach array stations are finally evaluated with respect to their applicability for source array beam forming (Sec. 9.6).

## 9.1 Comparison of theoretical and observed P arrival times

Theoretical P arrival times were computed using *cake* [Heimann et al., 2017] and a velocity model published by Málek et al. [2005] (Table 3), adding $v_s$ for 32 km depth following the suggestion of Rößler [2006]. The theoretical and picked arrival times differ by 0.05 to 0.09 s (Table 5). Hrubcová et al. present another velocity model with sharp steps instead of gradual increases with depth [2016, p. 888, Fig. 9]. Since no numbers are provided, the P wave velocities and depths were read from the figure in the publication (Table 4). These model fits very well the observed P arrival times. The errors are in the order of picking errors, estimated from multiple picking.

Table 3: Isotropic 1-D $v_p$ and $v_s$ velocity model by Málek et al. [2005]

| depth(km) | $v_p$ (km/s) | $v_s$ (km/s) |
|---|---|---|
| 0.0 | 3.70 | 2.18 |
| 0.41 | 5.37 | 3.16 |
| 2.46 | 5.81 | 3.57 |
| 8.41 | 6.10 | 3.58 |
| 32.0 | 7.20 | 4.16 |

.

Table 4: Isotropic 1-D $v_p$ velocity model, velocities read off from figure by Hrubcová et al. [2016].

| depth (km) | $v_p$ (km/s) |
|---|---|
| 0.0 | 4.3 |
| 0.25 | 4.3 |
| 0.25 | 5.1 |
| 0.50 | 5.1 |
| 0.50 | 5.3 |
| 5.0 | 5.3 |
| 5.0 | 6.3 |
| 12.0 | 6.3 |

Table 5: Theoretical and observed P phase arrival times on station V01. $t_{theo}$ (M) and (H) refer to the theoretical arrival times calculated using *cake* [Heimann et al., 2017] and the velcocity models by Málek et al. [2005] and Hrubcová et al. [2016] (cf. text). Times are in seconds after origin time.

| event | $t_{obs}$ (s) | $t_{theo}$ (M) | dt | $t_{theo}$ (H) | dt |
|---|---|---|---|---|---|
| 88004344 | 2.18901 | 2.12542 | 0.0635872 | 2.18285 | 0.00616194 |
| 88004405 | 2.19107 | 2.12702 | 0.0640458 | 2.18431 | 0.00676181 |
| 88004488 | 2.26385 | 2.20628 | 0.0575661 | 2.27003 | -0.00618398 |
| 88004510 | 2.28334 | 2.22023 | 0.0631058 | 2.27976 | 0.00358128 |
| 88004513 | 2.20029 | 2.11421 | 0.0860797 | 2.17976 | 0.0205333 |
| 88004607 | 2.21166 | 2.14495 | 0.0667075 | 2.20684 | 0.00481506 |
| 88004621 | 2.28859 | 2.23789 | 0.0507023 | 2.29465 | -0.0060592 |
| 88004739 | 2.23021 | 2.16811 | 0.0620981 | 2.23062 | -0.000408571 |
| 88004762 | 2.28397 | 2.21857 | 0.0654009 | 2.27826 | 0.0057057 |
| 88004906 | 2.27848 | 2.20577 | 0.0727144 | 2.26589 | 0.0125883 |
| 88005050 | 2.24108 | 2.18097 | 0.0601051 | 2.23912 | 0.00196279 |
| 88005074 | 2.27982 | 2.19589 | 0.0839294 | 2.25406 | 0.0257611 |
| 88005085 | 2.2247 | 2.15743 | 0.0672685 | 2.22004 | 0.00465559 |
| 88005106 | 2.27257 | 2.19573 | 0.0768423 | 2.25472 | 0.0178497 |
| 88005274 | 2.24677 | 2.18043 | 0.0663415 | 2.24015 | 0.0066181 |
| 88005410 | 2.25746 | 2.18878 | 0.0686833 | 2.24752 | 0.0099356 |
| 88004724 | 2.23708 | 2.16737 | 0.0697066 | 2.23234 | 0.00474144 |
| 88004348 | 2.25337 | 2.18705 | 0.0663223 | 2.25122 | 0.00214545 |
| 88004803 | 2.20742 | 2.13635 | 0.0710697 | 2.19796 | 0.00946134 |
| 88004447 | 2.29454 | 2.23625 | 0.0582861 | 2.29897 | -0.00443342 |
| 88004947 | 2.19697 | 2.11322 | 0.0837486 | 2.16989 | 0.0270848 |
| 88004600 | 2.32757 | 2.27845 | 0.0491218 | 2.33444 | -0.00687377 |

## 9.2 Sensitivity of source array beam forming towards location errors

Accurately determined hypocentre parameters are one prerequisite for source array beam forming. In order to test the sensibility towards location errors, source array beam forming was performed on synthetic data with low-pass filtered spikes at the theoretical onset times of the direct P phases. Theoretical arrival times were calculated from the locations of the catalogue and a P wave velocity of 5.6 km/s. Random location errors in the order of -10 to +10 m, -50 to +50 m, -100 to +100 m and -150 to +150 m were added to the location differences $d_x$, $d_y$ and $d_z$. For these new relative locations the shift times for beam forming were calculated. Beam forming was performed for velocities between 5.2 and 6.0 km/s with a slowness search grid spacing of 0.01 s/km. From fifty beam forming iterations for each location error range an estimate of the sensitivity towards location errors is obtained. Fischer et al. [2010] estimate a location error of approximately 100 m. Hainzl et al. [2012] assume max. 75 m location errors in horizontal directions and up to 150 m in depth. The resulting back azimuth and incidence angles of all iterations and error ranges are presented in Fig. 36.

Beam forming with up to ±10 m and ±50 m location errors does not show significant deviations in back azimuth or incidence angle. For relative location errors of up to 10 m the back azimuth varied by max. ±2° in 50 iterations, in the second case by max. ±6°. The incidence angle varied by ±3°, respectively ±7°. Although these errors are negligible it is already noticeable that $s_x$ in east-west direction varies more than the slowness components $s_y$ and $s_z$.

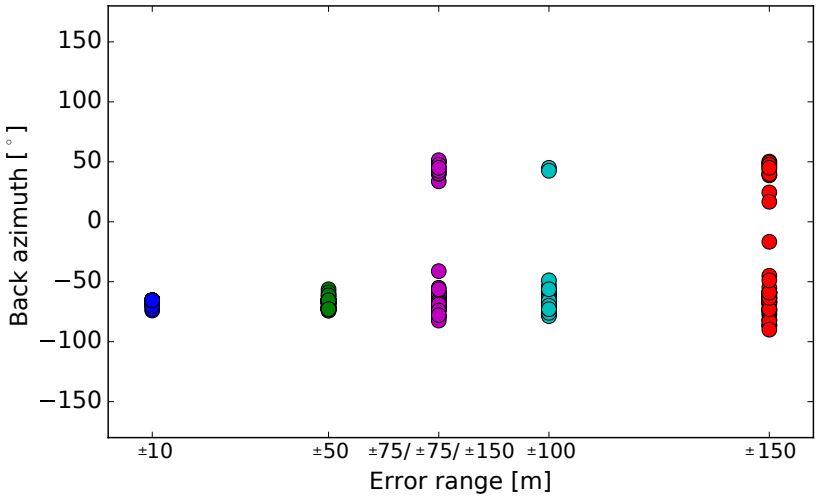


(a)

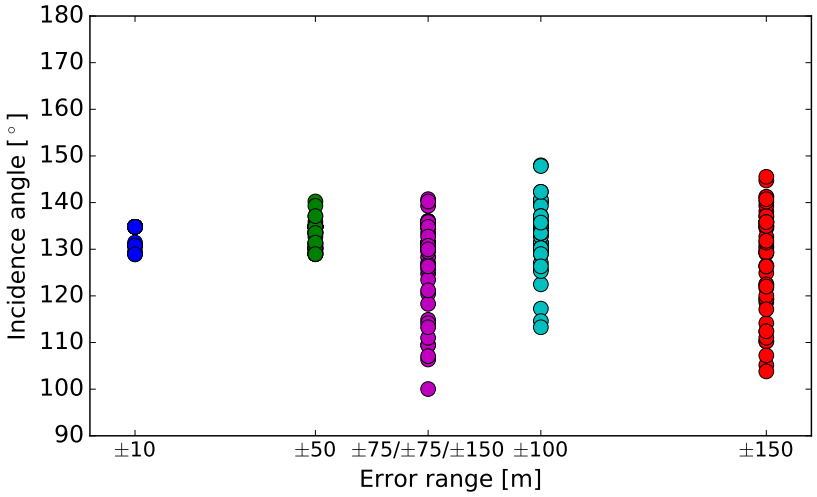


(b)

Figure 36: Derivations of back azimuth (a) and incidence angle (b) for different location error ranges. The relative location errors are determined using a random number function. While back azimuth and incidence angle are stable for small location errors, for larger location errors some solutions for opposite sign $s_x$ are found. These are visible here as positive back azimuth values. Angles are in source array (reciprocal) perspective. Beam forming was performed 50 times for each location error range.

For a variation of -100 m to +100 m, as well as for 75 m in horizontal directions and 150 m in depth, the weakness of the chosen source array becomes obvious. Since the east-west resolution is limited, in 2 of 50 iterations, respectively 11 of 50 iterations, the highest beam power within the 0.05 s long time windows is found for negative instead of positive $s_x$ values. Otherwise, the back azimuth variations were mostly less than 10°. 100 m [Fischer et al., 2010] is the absolute location error provided for the catalogue. For further work this error source is kept in mind. In case of the receiver array beam forming a similar procedure was not completed, because the locations of the receiver array stations are well known.

## 9.3 Source array beam forming results before and after alignment relative to P phase amplitude maxima

Recordings of the 22 source array events were analysed using beam forming. At first, beam forming was performed based on the origin times using the source array records of three stations (V01, V04 and V12). Due to wide P arrival power maxima in the beam forming results, in a second attempt all traces were aligned with respect to their maximum P phase amplitudes and shifted back by a theoretical slowness vector prior to beam forming. This enables beam forming independent of catalogue origin times.

The alignment greatly improved the beam forming results (cf. section 9.3.2). The first subsection deals with the results obtained without P alignment at three stations and the second part deals with the results from all 11 receiver stations obtained independently of origin time.

### 9.3.1 Beam forming dependent on origin times

Figure 37 presents the beam forming results of the source array for P wave velocities and S wave velocities recorded at the vertical component of station V01 without alignment with respect to the direct P phase amplitude maximum. The arrival of the direct P phase and the P coda are shown. S wave velocities were used in addition to P wave velocities to detect SP phases. The power resulting from beam forming on synthetic traces is plotted as thin lines along with the results. The synthetic traces are noise-free, containing only a P wavelet at the picked arrival times of each event (e.g. Fig. 37c). The wavelet was obtained from one model event of the source array for each station. The red arrows in the figure indicate local power maxima which can be interpreted as arrivals of converted or reflected phases.

The back azimuths of the direct P phase (-72.9°, -72.9° and -67.4°) deviate by up to 4° from the theoretical back azimuths (-74.4°, -74.3° and -71.5°) between the stations and reference event 88004344 obtained with the ObsPy function *geodetics.base.gps2dist_azimuth* [Beyreuther et al., 2010]. The incidence angles of the virtual reverse plane waves travelling from the receiver stations to the source array (take-off angles of the source array) are in the order of 120°. On the basis of a homogeneous velocity model, an angle of 132° would be expected. The slowness vector, which is used to obtain the optimal stack of the direct P phase (as well as other P phases), holds insight to the P wave material velocity within the source array area. From source array beam forming performed on recordings of station V01, V04 and V12 velocities of 6.5-6.6 km/s were inferred.

Besides the direct P phase several other local maxima occur in the stacked power. The power stacks of station V04 and V12 show a maximum at about 0.1 s after the arrival of the direct P phase. For the results of V01 the same can be surmised. This was initially interpreted as a PP phase travelling through the receiver array in western direction, slightly south of the direct P phase. The observation is further discussed in section 9.4 as an example of possible misinterpretations. In the $v_s$-stacks, another power height is observed for stations V01 and V04 arriving approximately 0.3 s after the direct P phase and travelling in south-western direction.

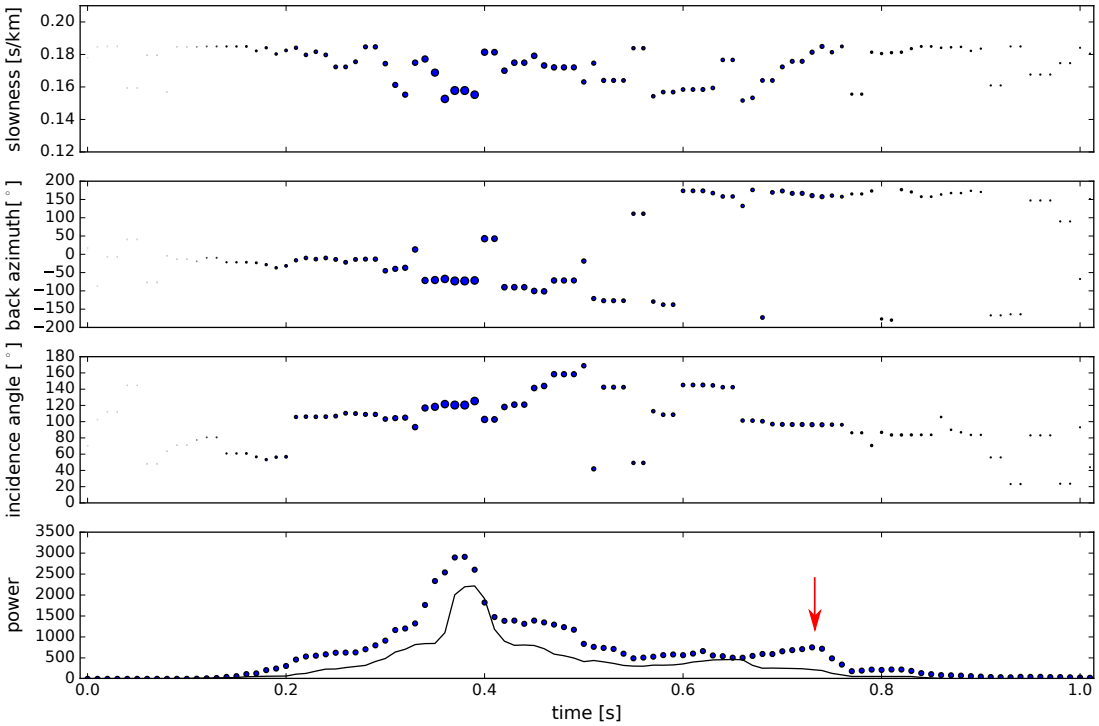


(a) Beam forming result, dependent on origin times. P coda with P wave slownesses.

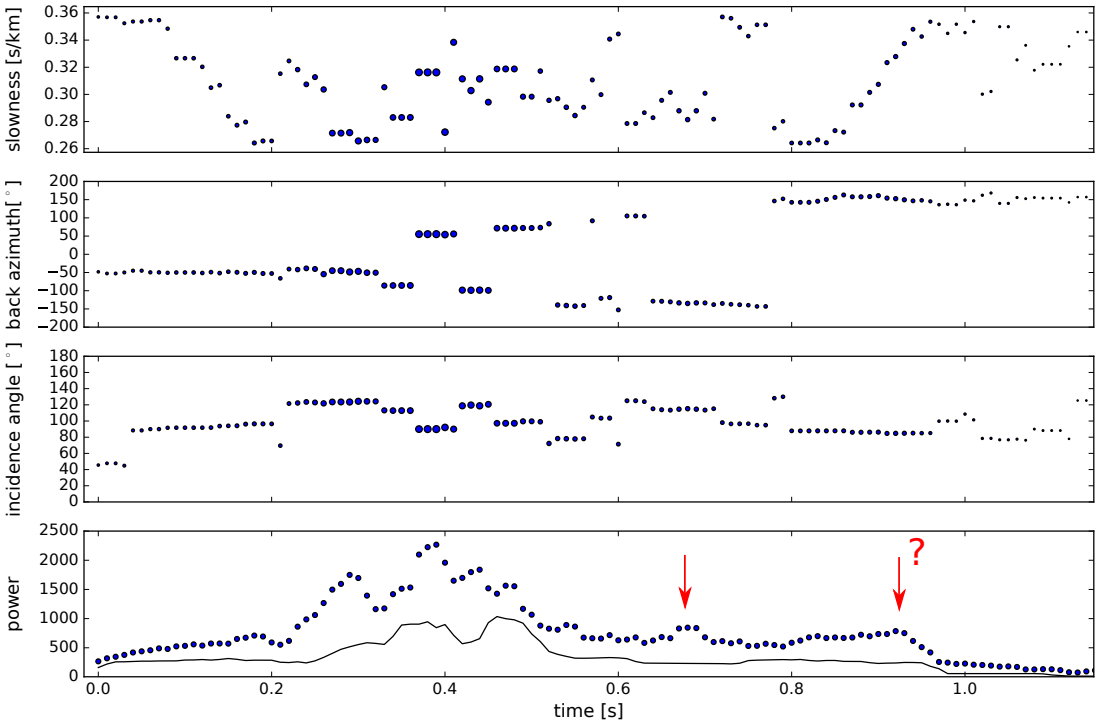


(b) Beam forming result, dependent on origin times. P coda with S wave slownesses for detection of SP phases.

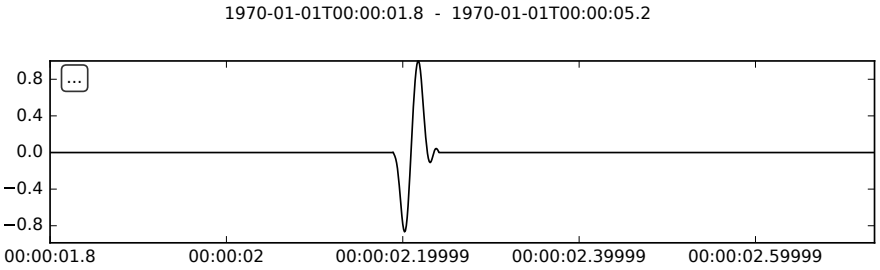


(c) Synthetic trace with P wavelet.

Figure 37: (a) and (b): Results of source array beam forming on records of station V01, P coda only, dependent on origin times (not aligned with respect to max. P amplitudes). Time step 0.01 s, window length 0.05 s. Beam forming with (a) P wave and (b) S wave velocities. Red arrows indicate potential arrivals of converted or reflected phases. The thin line displays the power resulting from the same beam forming process with synthetic traces. Note that the overall stack power is greatly improved by P alignment (cf. text) and the marked phases are not visible any more (Fig. 39). (c) The synthetic beam forming power shown in Fig. 37 was calculated from traces where the wavelet was set to the picked P onset times, not to maximum amplitude times.

### 9.3.2 Improvements of beam forming using P alignment

The wide power maxima and slow decline of the direct P phases in the source array stacks indicate that the direct P phases are not stacked optimally, most likely due to imprecise origin times or locations. Furthermore, this impression is confirmed when looking at the vertical-component traces, shifted in time for the observed slowness vector of the direct P phase (Fig. 38a). Therefore, the maximum amplitudes were picked, the traces aligned and shifted back for a theoretical direct plane wave as described in Sec. 6.3. In comparison to the beam forming results dependent on origin time, now the obtained stacks show great improvements (cf. Fig. 39). The P phase is very strong on the vertical component trace, while for most stations the S phase appears strongest on east component, pointing to a strong SV phase. When the vertical traces are now shifted in time for the observed back azimuth and incidence angle, the direct P phase wavelets are better aligned (Fig. 38b). Remaining derivations result from imprecisely known hypocentres.

The alignment with respect to the maximum P amplitudes clearly improves the beam forming results, although the results of the residual calculation as well as the comparison of theoretical and observed P arrival times (cf. sec. 9.1) indicate well known origin times and locations. The stacked power is double to quadruple compared to beam forming with respect to the catalogue origin times.

A velocity model is needed for shifting back the traces after the alignment. The influence of different velocities within the source array on the obtained back azimuth and incidence angles was evaluated by performing beam forming on two stations with P phase velocities in 5 to 12 km depth varying between 5.75 and 6.75 km/s (8% derivation from velocity model by [Hrubcová et al., 2016]). The back azimuth and incidence angle varied both by maximum 8°. Larger derivations from the velocity model are not likely.

In contrast to the stacks depending on the origin times, the previously described and interpreted phases do not show up on those stacks which are independent of origin times (Fig. 39 and appendix Fig. 53 and 53). Instead a presumable PS phase arriving about 0.15 s after the direct P phase is observed on the E component beam forming results of most stations. This phase travels with P phase velocity through the source array in a direction similar to the direct P phase. Assuming a P-SV conversion explains the strong occurrence on the east component. Additionally, on some N and E components a phase arriving before the direct S phase is observed. This might be a SP phase, converted at the same discontinuity. However, the phase is observed less often and less distinct.

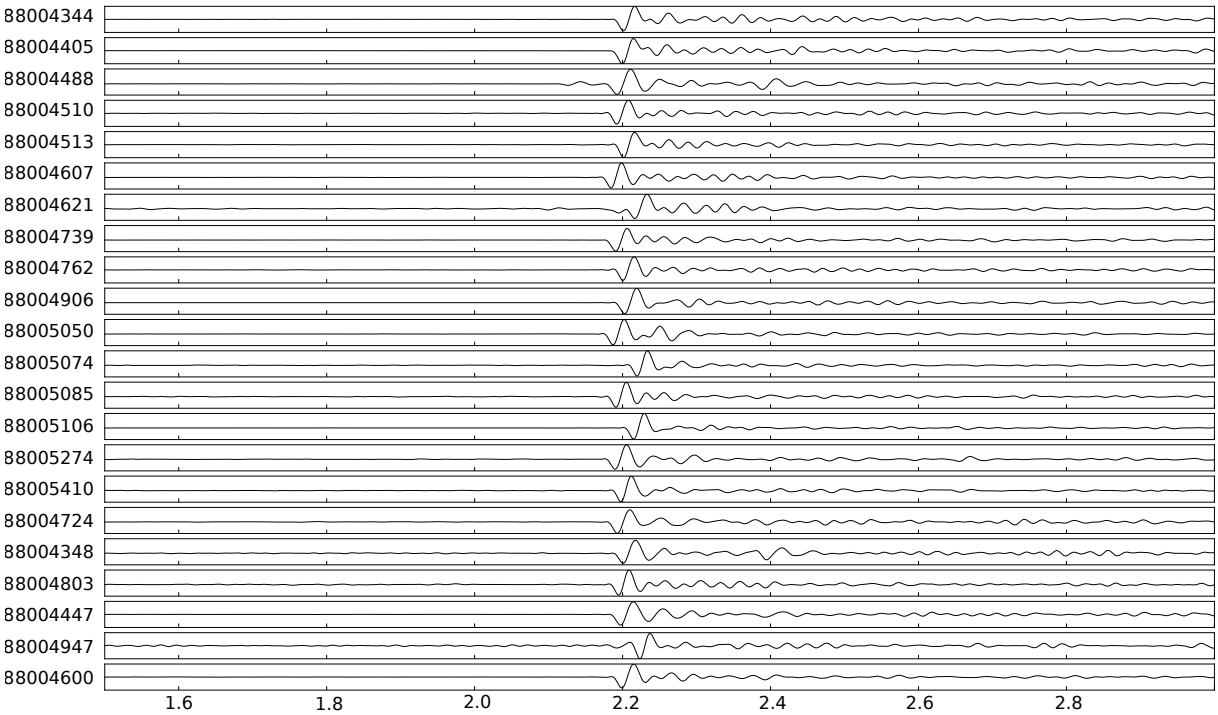


(a)

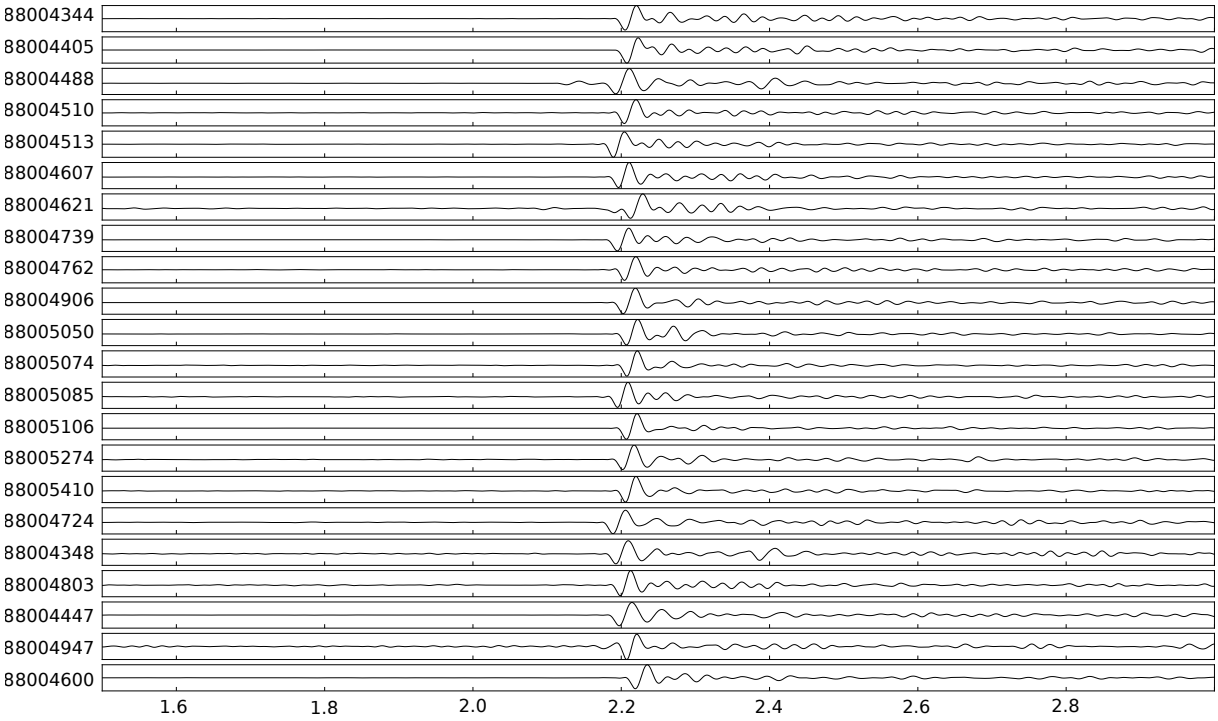


(b)

Figure 38: All source array vertical-component traces, station V01. Shifted in time with the observed slowness vector. (a) Dependent on catalogue origin times, (b) aligned with respect to amplitude maximum and shifted back before being shifted according to the observed slowness vector. The removal of the dependence on origin times improves the alignment of direct P phases. Remaining deviations result from imprecisely known hypocentres.

An SP phase converted at the same discontinuity would travel through the source array with an S phase velocity in a direction similar to the direct P and S phase. Arriving as a P phase at the receiver station, it should be strongest on the vertical component. However, the arrival of the direct S phase on the vertical component stack is not as sharp as the direct P phase. The bad visibility of a presumed SP phase might be explained through a wider S phase without distinct stack maxima. The directional information obtained for the PS phase resembles the direct P phase. In contrast, the SP phase is not only observed less often but also seems to travel north of the direct phase and nearly horizontally within the source array. It is therefore not certain, whether an SP phase of the same discontinuity is observed. The PS phase is interpreted with respect to its conversion location in section 9.4.

Another maximum occurs on the power stacks of more than half of the stations at 0.2 - 0.23 s after the direct P phase. It travels through the source array in southward direction. Shifting all traces for the obtained back azimuth and incidence angle indicates that the maximum is formed by constructive summation of the direct P phase of five events shifted

into that time window. The phase is therefore not interpreted further.

Besides the described phase following the direct P phase and the precursor of the direct S phase, no other distinct structural phases were observed. In contrast, a strong structural phase was observed on the records of deeper events by Hiemer [2009] and Hrubcová et al. [2016]. Therefore, the beam forming and grid search methods were tested on deeper events in a second source array (Sec. 9.5).

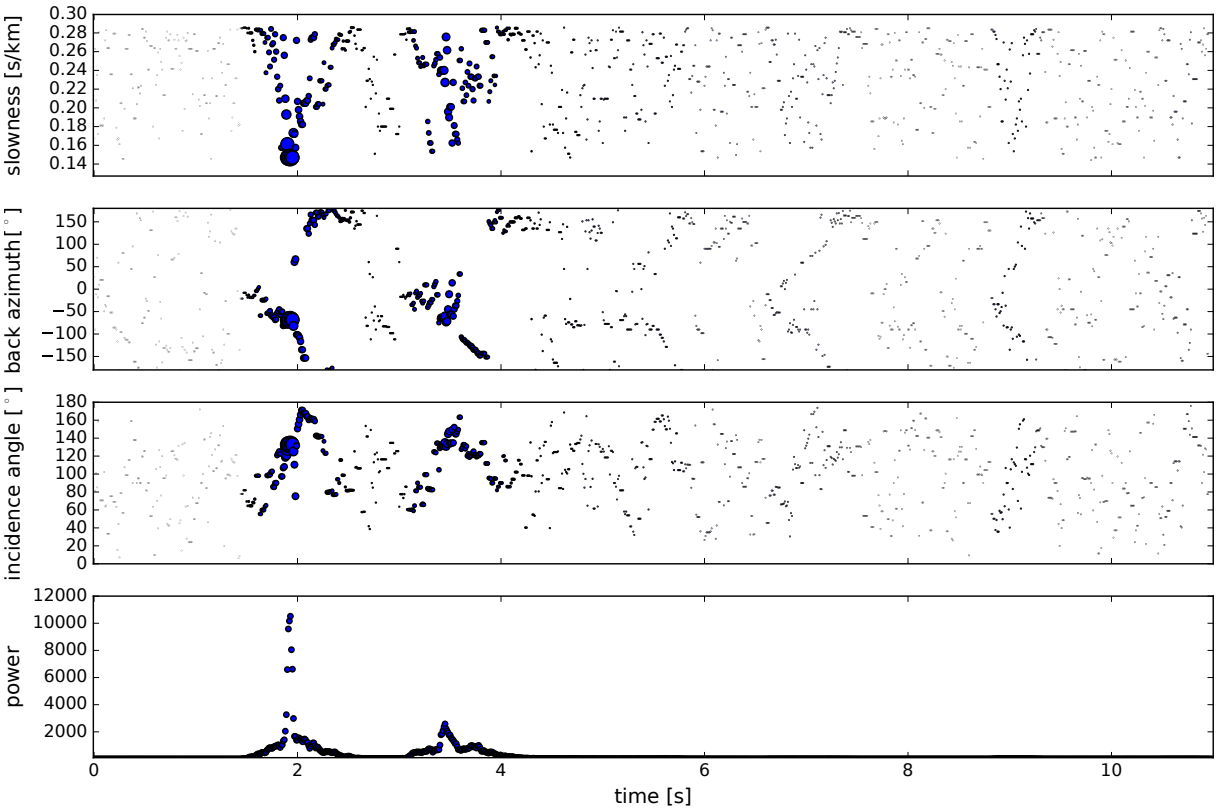


(a) HHZ

Figure 39: Results of source array beam forming on records of station V01 after alignment with respect to max. P phase amplitude. (a) HHZ, (b) HHN and (c) HHE component. Time step: 0.01 s, window length: 0.05 s, velocity range: 3.5 - 7 km/s, bandpass filter: 1-60 Hz. Red arrows indicate potential arrivals of converted or reflected phases. Note the strongly improved power. The direct P phase is strongest on vertical component (a), while the direct S phase is strongest on east component (c).

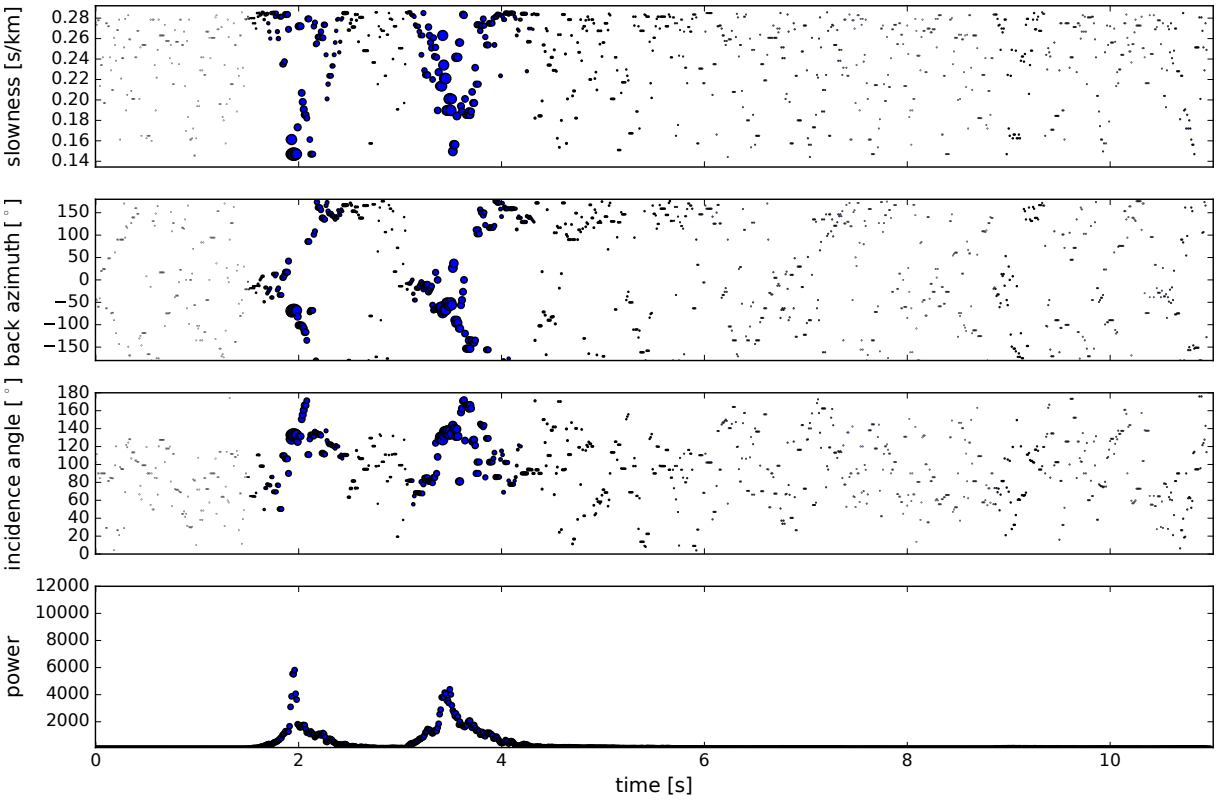


(b) HHN

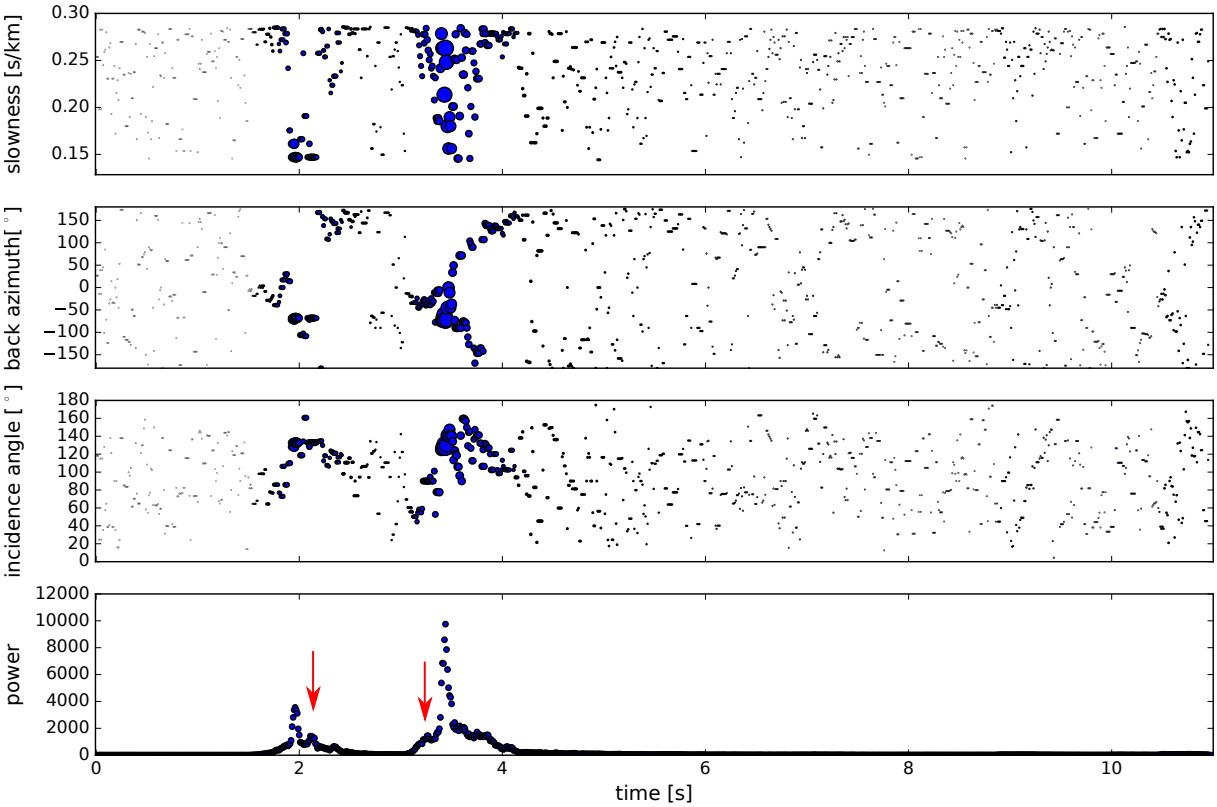


(c) HHE

Figure 39: cont.

## 9.4 Interpretation of phases detected with source array beam forming

The phases found using source array beam forming are compared to phases postulated in publications by Hrubcová et al. [2016] and Hiemer [2009]: Hrubcová et al. postulate a discontinuity in 2 to 6 km depth which could act as a barrier for fluids and hence for seismicity. At sharp velocity contrasts, P-to-S and S-to-P wave conversions occur. They observed a prominent SP phase arriving 0.7 s after the arrival of the direct P phases on a seismogram of WEBNET station SKC. Hiemer [2009] observed a PP phase in a migration analysis of deeper earthquakes of the 2008/2009 swarm, recorded with the Rohrbach Array. He states that this phase is converted south of the virtual direct line between the Rohrbach Array and the focal zone in about 4 km depth. For the migration a homogeneous velocity model ($v_p = 6$ km/s) was used. In order to compare the published detections with my observations, travel time calculations and the two methods for the determination of the conversion locations (Section 7) were used.

First, a velocity model was set up based on a figure from Hrubcová et al. [2016]. S waves velocities were calculated assuming a ratio of 1.71. Arrival times of P, SP, PS and S phases were calculated (Fig. 40 and Table 6), assuming conversions taking place along the direct line between the focal zone and the Rohrbach array.

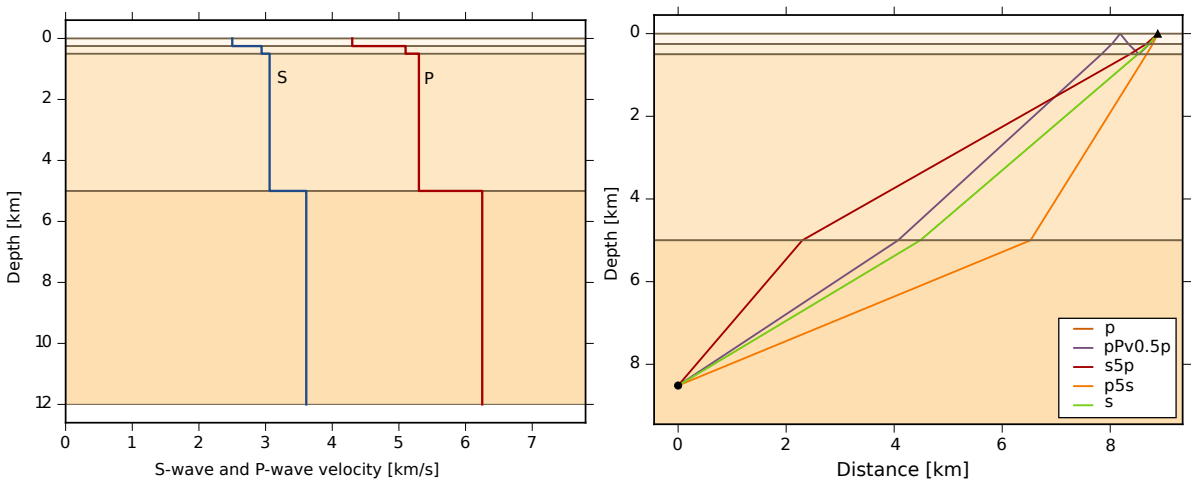


(a) (b)

Figure 40: (a): Velocity models with discontinuity in 5 km depth used for calculation of arrival times and travel paths of P, PPP, SP, PS and S phases. Based on model by [Hrubcová et al., 2016]. (b): Travel paths for P, PPP, S, PS and SP phases calculated for model (a). The travel paths of the direct P and S phases are almost congruent.
*Figures produced using pyrocko cake [Heimann et al., 2017].*

Table 6: Theoretical arrival times of P, PPP, SP, PS and S phases, assuming a travel path in line between source and receiver array. Calculated for event 88004344 recorded at station V01 (distance = 8.88 km, source depth = 7.8 km). P wave velocity from Hrubcová et al. [2016], S velocities obtained using $v_s/v_p = 1.71$.

| phase | $t_{xx}$ [s] | $t_{xx} - t_p$ [s] | obs. arr. [s] |
|---|---|---|---|
| P | 2.184 | - | 2.189 |
| PS (0.5 km) | 2.270 | 0.086 | |
| PPP (0.25 km) | 2.281 | 0.097 | |
| PPP (0.5 km) | 2.358 | 0.174 | |
| SP (5 km) | 2.73 | 0.546 | |
| PS (5 km) | 2.993 | 0.809 | |
| SP (0.5 km) | 3.603 | 1.419 | |
| S | 3.737 | 1.553 | 3.665 |

#### S and PS phase

The direct P phase and S phase arrival times match the model well. The presumable PS phase is likely to originate from 0.6 to 0.8 km depth (assuming constant velocities of $v_p$ = 4.3 km/s and $v_s$ = 2.5 km/s in the upper first km). The velocity model by Hrubcová et al. [2016] does not match the PS and SP arrival times. By lowering the 0.5 km velocity change in the model down to 0.9 km, the observed and calculated travel times of PS and SP are approximated.

#### PP phase detected on non-aligned stacks

On the stacks calculated without P alignment, a prominent phase is observed in the $v_p$ velocity stacks of stations V04 and V12 arriving about 0.1 s after the direct P phase. Using the analytical method with a homogeneous velocity along the entire travel path points to a possible scatterer in 4 km depth about 2.5 km west of the source array and hence south of the direct line between source array and receiver station V12 (in case of the phase being a PP reflection) (Fig. 42a). Using a 250 m grid spacing in all dimensions of a large grid, points to a conversion location in 5.0 km depth about 2.25 km west and 0.5 km south of reference event 88004344 (Fig. 43). However, due to the high amplitudes visible in the stack surrounding the evaluated phase and due to the small travel time difference to the direct P phase, this result is not reliable. Additionally this phase is not visible in the stacks which are independent of origin time due to alignment of P phases. In contrast, the grid search method indicates the existence of the phase even after applying the alignment procedure.

In order to understand whether the presumable PP phase travelling south of the direct

line between source and receiver array exists, all traces were shifted in time for the corresponding back azimuth and incidence angle. Figure 41 shows that the direct P phase wavelet of several events is shifted into the time window of question, when such a slowness vector is used. I therefore assume that this power maxima results from aliasing.

No distinct structural phase except the PS phase is observed at the stacks independent of origin time.

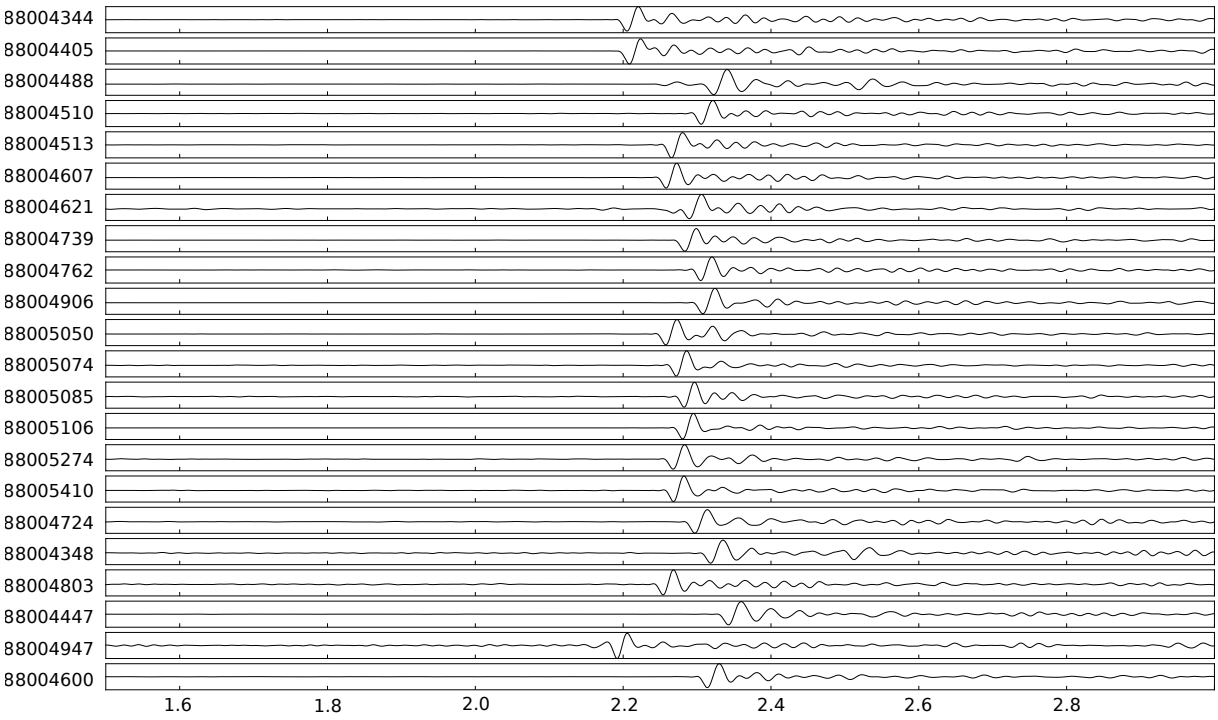


Figure 41: All source array vertical-component traces, station V01. Shifted in time for $baz = -105°$ and $i = 140.5°$. The P phase amplitude maxima of some traces are shifted to about 0.15 s after the direct P phase of reference event 88004344 (first line). Therefore, a local maxima in the stack and grid search at this time should not be interpreted as a separate PP phase.

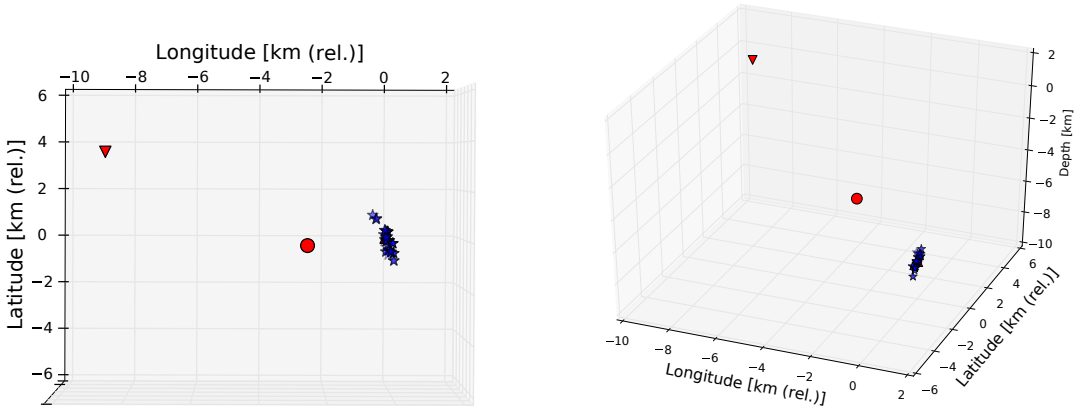


(a) (b)

Figure 42: Analytical determination of conversion locations of phases detected in Fig. 37. (a) + (b): First phase after arrival of direct P phase in $v_p$ stack V12, falsely interpreted as a PP phase. The determined conversion depth is in 4.3 km depth, 2.5 km west of reference event 88004344. The evaluation of the single traces shifted in time for the observed slowness vector shows that the "phase" is in fact an **aliasing artefact** (Fig. 41).

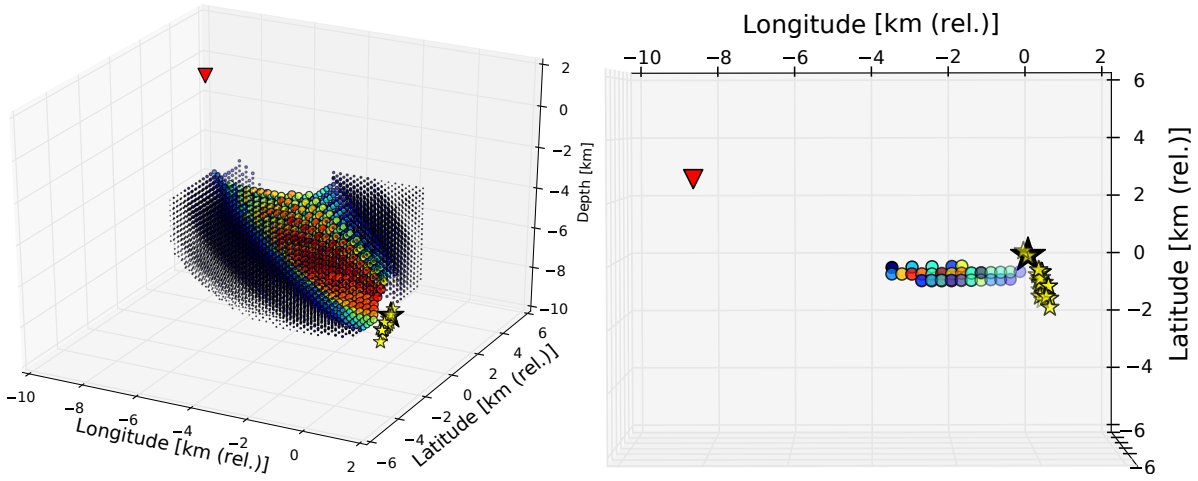


(a) (b)

Figure 43: Grid search result for location of potential PP reflection location (cf. Fig 41, aliasing!). The highest power was obtained for a location 2.25 km West and 0.5 km South of the reference event 88004344 in 5.0 km depth. (a) All grid points with travel times between 0.08 and 0.2 s after direct P phase, (b) only those with 90% of maximum stacked power. Yellow stars: source array events. Black star: reference event 88004344. Red triangle: Location of receiver V12.

## 9.5 Beam forming results of deeper events

In literature structural phases occurring on the records of deeper events are described (e.g. Hrubcová et al. [2016] and Hiemer [2009]). 12 earthquakes with depths between 9.2 and 10.3 km were chosen to set up a new source array (Table 7 and Fig. 44). An optimal source array design could not be considered as only few events with both, a prominent phase showing up about 0.85 s after the direct P phase (Fig. 45b) and an acceptable signal-to-noise ratio were found. Hrubcová et al. [2016] observed a structural phase which is interpreted as an S-to-P converted phase. Hiemer [2009] described a PP reflection travelling south-west of the direct line connecting the source and receiver locations.

Table 7: Information on earthquakes of the second, deeper source array. Based on information from event catalogue of T. Fischer [Fischer et al., 2010].

| Event | Origin time | Lat. (°) | Long. (°) | Magn. | Depth (m) |
|---|---|---|---|---|---|
| 88004271 | 2008-10-18 20:56:53.820 | 50.212207 | 12.449056 | 0.9 | 10265 |
| 88004280 | 2008-10-19 03:04:54.820 | 50.21237 | 12.448774 | 1 | 10324 |
| 88004281 | 2008-10-19 03:05:24.710 | 50.212703 | 12.448577 | 1.4 | 10223 |
| 88004282 | 2008-10-19 03:13:54.840 | 50.21261 | 12.448663 | 1.7 | 10204 |
| 88004284 | 2008-10-19 05:20:04.570 | 50.194613 | 12.456841 | 0.7 | 8934 |
| 88004293 | 2008-10-19 11:49:12.820 | 50.213997 | 12.445613 | 1.1 | 10302 |
| 88004323 | 2008-10-20 04:48:06.520 | 50.211536 | 12.448647 | 0.2 | 10109 |
| 88004329 | 2008-10-20 06:07:15.210 | 50.211784 | 12.446206 | 0.3 | 9979 |
| 88004422 | 2008-10-22 02:51:07.160 | 50.213285 | 12.448636 | 0.2 | 9712 |
| 88004424 | 2008-10-22 12:26:13.460 | 50.212874 | 12.448727 | 0.9 | 9772 |
| 88004463 | 2008-10-27 09:24:12.030 | 50.206779 | 12.450222 | 0.9 | 10134 |
| 88005141 | 2008-11-12 06:51:18.700 | 50.199679 | 12.454434 | 0.6 | 9261 |

From source array beam forming a back azimuth of -132° and an incidence angle of 86° were obtained, describing a phase travelling horizontally in south-western direction (Fig. 45c). The absolute slowness within the source array indicates that the phase is travelling as a P phase through the source array. Its is therefore assumed that the phase is not an SP conversion. The back azimuth and incidence angle indicate that the phase is most likely not a conversion travelling in plane with the direct phases but a reflection from a location south-west of the source array. The observed phase of most events is strongest on the vertical trace of the receiver stations. However, in case of some events, the amplitude of the phase is equally strong on the east component. Therefore, besides a PP reflection, a PS conversion could be a possible candidate to explain that phase. Receiver array beam forming using several events of the 'deep' source array confirms a travel path south of the travel path of the direct P phase. However, solutions can be found for both, a P velocity and an S velocity with different incidence angles. Shifting

the source array traces for the obtained back azimuth and incidence angle of the phase does not result in a truly satisfying alignment of the phase. The single events are close together and therefore location errors affect the obtained results.

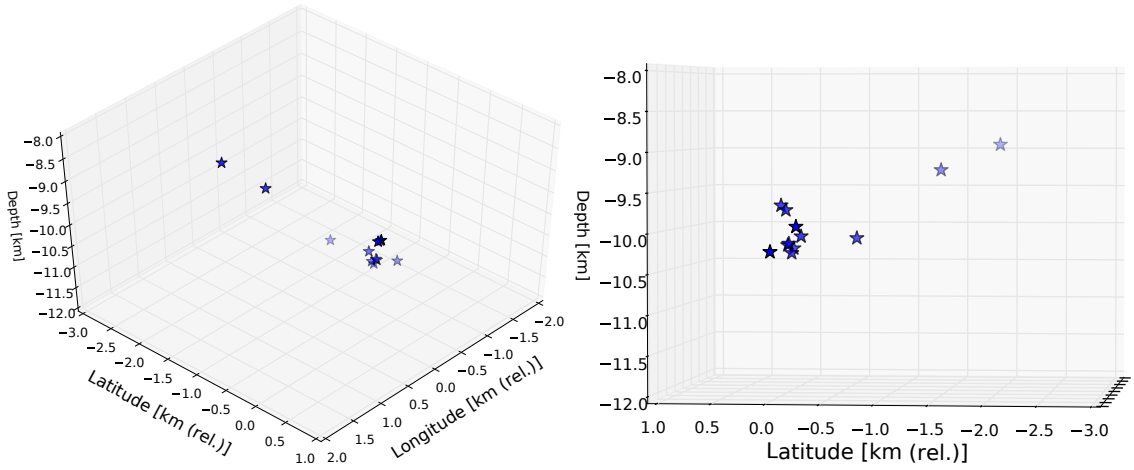


(a) (b)

Figure 44: Source array hypocentres of second, deeper array. Latitude and longitude are in km relative to event 88004271.

In case of a PP reflection, the analytical solution with a homogeneous velocity model points to a reflection in 10.7 km depth, roughly 5.4 km west and 4.8 km south of the deep source array. Searching for a (PP-) reflection location with the grid search method using the same events implies that while the latitude is well resolved (4.8 km south of reference event like the analytical solution), the depth and longitude are less distinct (Fig. 45a). The highest power in the grid search was obtained for a reflection 7 km west and 4.8 km south of the source array in 4.5 km depth. For comparison: Hiemer [2009] located the reflection origin in 4 km depth, 6 km west but at the same latitude as his source array. Hiemer's results were calculated using a homogeneous velocity model for the entire travel path ($v_p$= 6 km/s) and 6 events.

In case of a PS conversion, the grid search as well as simple travel time calculations point to a conversion in about 5 km depth, roughly in plane with the travel paths of the direct phases. For one thing, this contradicts the direction obtained from source array beam forming. On the other hand, it is remarkable, that the described phase is not observed on records of events shallower than 9 km. Generally, the occurrence on seismograms of deep events only could be explained by a conversion in greater depth. However, calculations of travel times for PS and SP phases travelling in direction of the direct phases require a conversion depth of about 5 km to match the arrival times of the phase (0.85 s after the direct P phase).

In case of a PP reflection off the path of the direct phases the incidence angle of the emitted waves at the reflector in combination with the slope of the reflector surface could possibly lead to an occurrence of the phase with large amplitudes on the seismograms in case of deeper events only. The requirements for such a ray-reflector geometry have not been investigated in the course of this thesis.

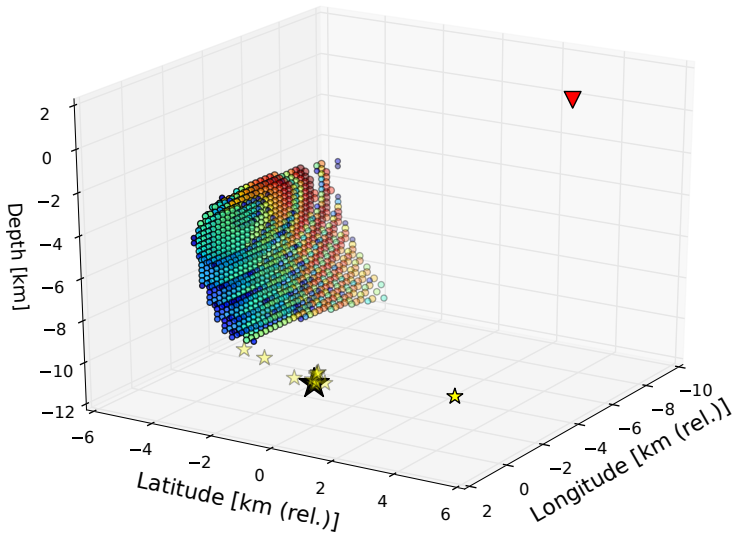


(a) Grid search results.

Figure 45: (a) Grid Search result. For all travel paths arriving 0.6 to 1.0 s after the direct P phase in a 250 m spacing grid the power stacks are calculated. Only results with >50% of maximum power are shown. The highest power was obtained for a reflection 7 km west and 4.8 km south of the source array in 4.5 km depth. Latitude ($s_y$) is better resolved than depth ($s_z$) and longitude ($s_z$).
(b) Waveforms of 12 deeper events on vertical-component traces of station V01 (bandpass filtered 1-60 Hz, normalized). The events are forming a new source array containing a structural phase arriving about 0.85 s after the direct P phase.
(c) Beam forming results, time window 0.1 s. Only P wave velocities between 5.5 and 7 km/s are used. Red arrow indicates arrival of structural phase observed in (a).

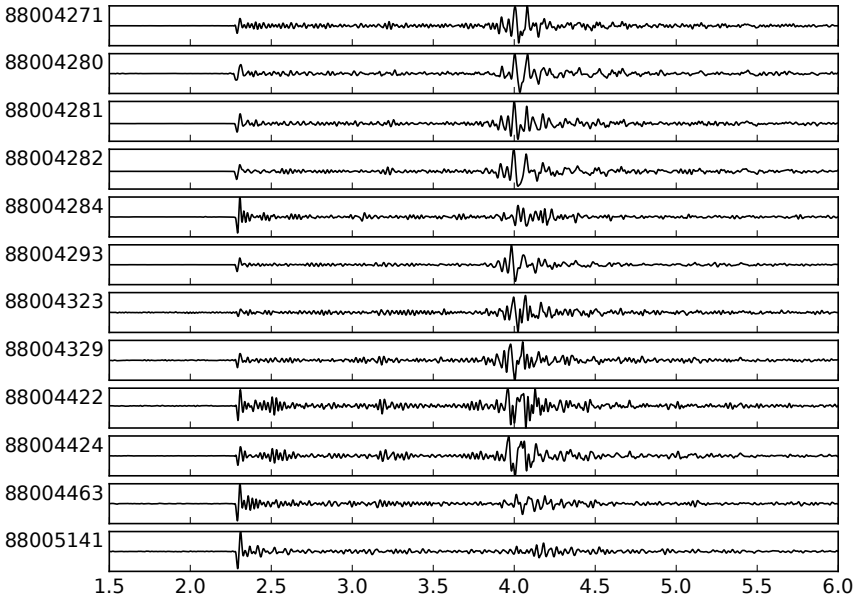


(b) Waveforms of deeper events (V01, HHZ).

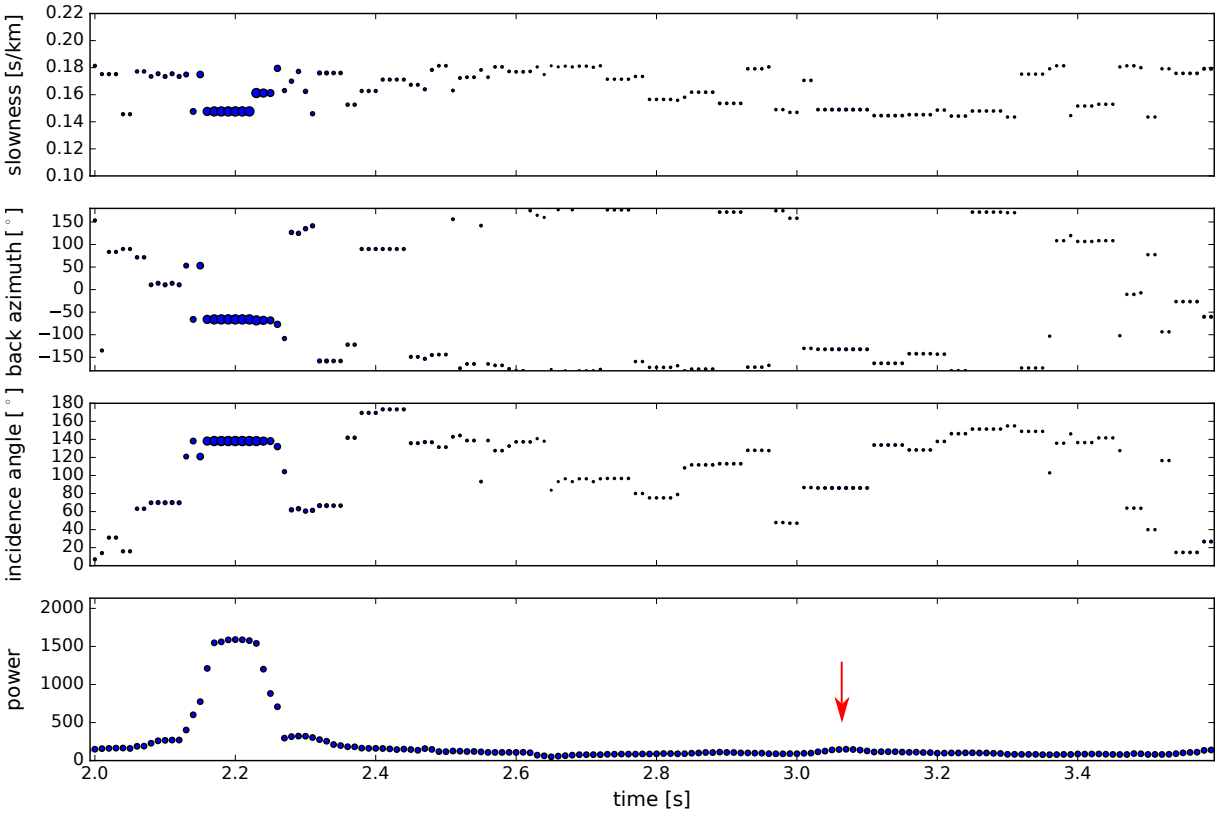


(c) Beam forming results P coda (V01, HHZ).

## 9.6 Comparison of Rohrbach stations based on the source array records

How suitable a receiver station is for source array beam forming depends mainly on the resemblance and complexity of the recorded waveforms. Both the cross-correlation coefficient plots and the source array beam forming results provide this information.

First of all, the visual comparison of P waveform complexity of all source array events recorded at all stations provides information on subsurface effects of the receiver locations. Based on visual evaluation, the waveforms recorded at receiver stations V01, V02, V03, V05, V07 and V09 are simpler than the ones recorded at the northern stations of the receiver array (V04, V08, V10, V11 and V12). Fig. 46 presents the waveforms of the source array events recorded at station (a) V01, (b) V05, (c) V08 and (d) V12 (bandpass filter 1-60 Hz). The P phase signals are simpler on stations V01 and V05, which additionally have higher cross-correlation coefficients and very distinct beam forming results.

The cross-correlation coefficients of every event pair of the source array were calculated for recordings of all stations (cf. Sec. 8.1 and figures in supplementary material on CD). They are higher than the coefficients of station pairs recording the same events. However, small differences between the stations are visible. While stations V01, V03, and V05 show up with highest coefficients, V12 clearly has the least resembling records of the source array events. The beam forming results, additionally used to evaluate the different stations, confirm the previous impression. The power stacks are most distinct on stations V01 to V07 and V09.

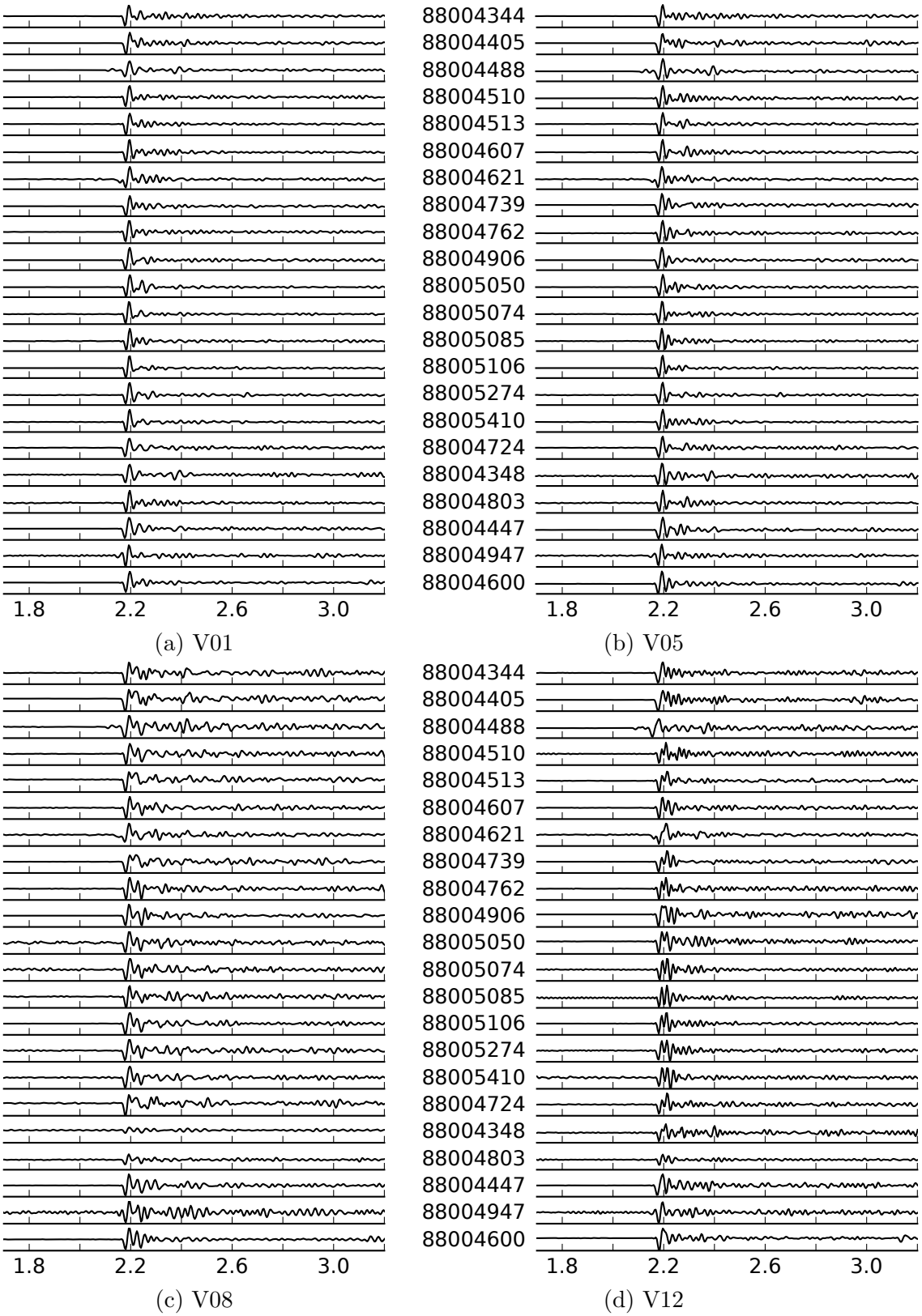


(a) V01 (b) V05

(c) V08 (d) V12

Figure 46: P waveforms of all source array events recorded at stations V01, V05, V08 and V12. The P waves are first, simpler on stations V01 and V05 and second, more similar on these stations. Numbers are event names (Table 2).

# 10 Receiver array analysis: Results

Receiver array beam forming was implemented using the Rohrbach Array recordings of six different events (88004344, 88004405, 88004488, 88004621, 88005106 and 88005410) (cf. Table 8).

## 10.1 Direct P phase: Comparison of observed and theoretical travel paths

The beam forming results of the receiver array hold a first interesting feature by comparing the back azimuths of the direct P phases to the theoretical back azimuths: While the theoretical back azimuths between the Rohrbach Array and the epicentres are in the order of 105 to 113°, the back azimuths obtained from beam forming are in the order of 127 to 145°. Errors resulting from mistakes in the beam forming code were ruled out by computing peak onsets at theoretical arrival times. The obtained back azimuths resemble the theoretical directions.

The direct P phases seem to travel south of the direct line between source and receiver array. The target area consists of a variety of geologically different materials. Hence, the observed discrepancy between observed and theoretical travelling direction can be explained by a material change from phyllite in the northern part beneath the receiver array and granitic rocks south of it. Fermat's principle describes that rays travel along paths of extremal (here minimal) travel time.

For event 88004344 a theoretical incidence angle of 43.9° was calculated under the assumption of a homogeneous velocity. From the stacking result, an incidence angle of 32.0° was obtained. This can be explained through steepening of the ray with a decrease of material velocity for decreasing depth.

## 10.2 Other phases obtained using beam forming

Besides the direct P phases, the beam forming results of the receiver array show mainly three reoccurring phases after the P phase. Power maxima are observed roughly 0.06 s, 0.1 s and 0.22 s after the direct P phase. Comparing back azimuth and incidence angle can give a hint on whether the phases observed on the stacks of different events originate from the same conversion locations or reflectors. Additionally, theoretical arrival times for the different source-receiver combinations can be computed. An onset roughly 0.20-0.23 s after the direct P phase is observed on $v_p$-stacks of events 88004344, 88004488 and 88004405. This phase appears to arrive from the same direction as the direct P phase. Another possible phase arriving 0.1 s after the direct P phase appears to arrive from south-western directions. However, the results are not truly consistent. On two stacks a

power maximum arriving 0.06 s after the direct P phase from west is observed. Both, the 0.06 s and 0.1 s onsets are very close to the direct P phase. Therefore, before any attempt to interpret them as phases aliasing should be tested carefully. The receiver array results are provided in the appendix (Fig. 55 - 60).

Table 8: Phase information of beam forming results (Reciever Array - Events 88004344, 88005106, 88004621, 88004488, 88005410 and 88004405). Arrival times correspond to time axis shown in plots.

| event | $t_{xx}$ (s) | $t_{xx} - t_p$ (s) | baz (°) | i (°) | $\|\vec{s}\|$ (s/km) | theo. baz (°) | notes |
|---|---|---|---|---|---|---|---|
| 4344 | 2.19 | | 131.2 | 32.0 | 0.20 | 105.5 | direct P |
| 4344 | 2.25 | 0.06 | -80.0 | 59.9 | 0.20 | | |
| 4344 | 2.42 | 0.23 | 126.9 | 32.0 | 0.19 | | |
| 5106 | 2.26 | | 127.9 | 35.5 | 0.20 | 110.5 | direct P |
| 5106 | 2.37 | 0.11 | 119.0 | 83.1 | 0.33 | | |
| 5106 | 2.35 | 0.09 | 51.1 | 68.5 | 0.22 | | |
| 5106 | 2.32 | 0.06 | -17.5 | 75.0 | 0.19 | | |
| 4621 | 2.30 | | 127.9 | 31 | 0.22 | 112.1 | direct P |
| 4621 | 2.41 | 0.11 | -90 | 87.5 | 0.22 | | |
| 4621 | 2.40 | 0.10 | -120.8 | 66.7 | 0.28 | | |
| 4488 | 2.27 | | 145.0 | 45.5 | 0.17 (?) | 112.7 | direct P |
| 4488 | 2.35 | 0.08 | -90 | 82.1 | 0.22 | | |
| 4488 | 2.47 | 0.20 | 142.1 | 41.1 | 0.17 (?) | | |
| 5410 | 2.25 | | 127.9 | 31 | 0.22 | 109.6 | direct P |
| 4405 | 2.19 | | 131.2 | 32.0 | 0.20 | 105.7 | direct P |
| 4405 | 2.27 | 0.08 | 79.2 | 76.7 | 0.22 | | |
| 4405 | 2.41 | 0.22 | 126.9 | 32.1 | 0.19 | | |
| 4405 | 2.29 | 0.10 | -77.9 | 74.4 | 0.30 | | |
| 4405 | 2.42 | 0.23 | 131.2 | 19.5 | 0.32 | | |

# 11 Discussion and concluding remarks

## 11.1 Summary

In the course of this thesis, 22 events were selected for source array beam forming and to evaluate possible reflection/ conversion locations. Prerequisites of source array usage (precisely known origin times and locations, high waveform similarity, homogeneous velocity within the source array) were tested and the beam forming results were evaluated with respect to interesting phases under the assumption of singular reflections/ conversions. The entire workflow of the source array analysis performed in this thesis is summarized in Fig. 47. Additionally, 12 deeper events were chosen to analyse a structural phase already visible on the vertical traces and several single events were used for receiver array beam forming.

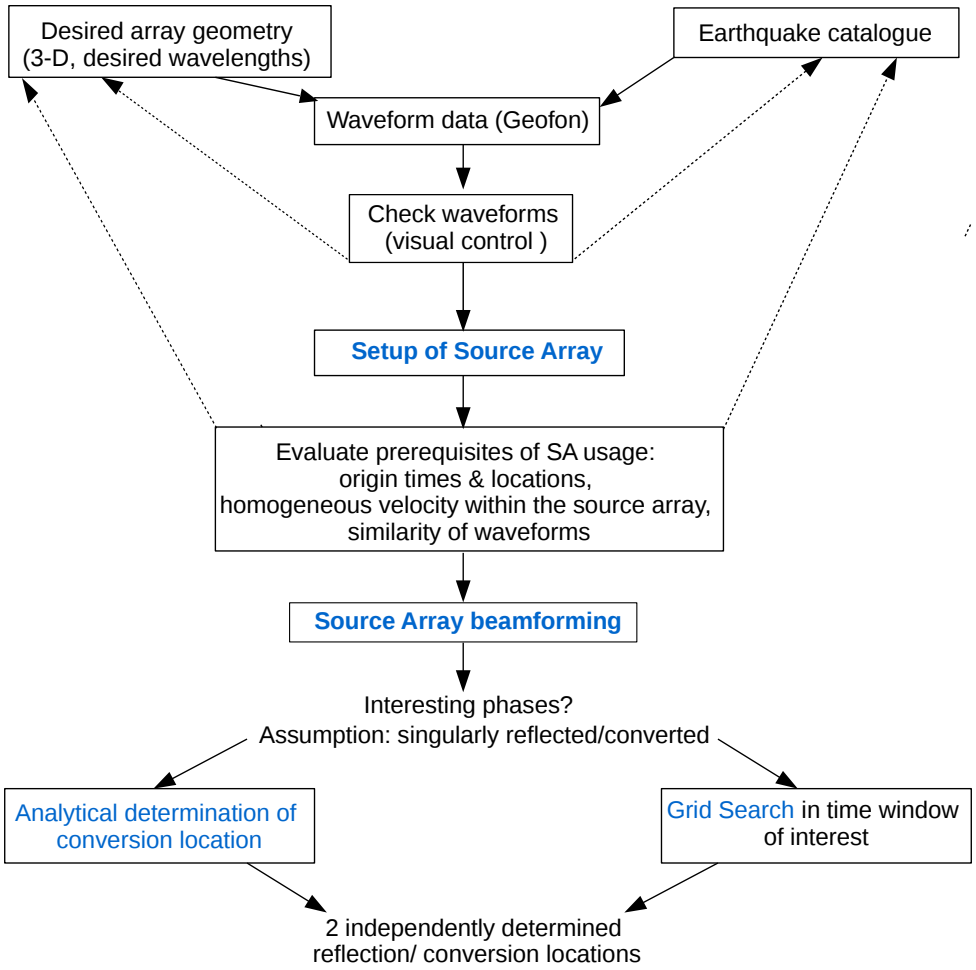


Figure 47: Workflow diagram of source array analysis of crustal phases.

It was observed that the velocity model shown in Hrubcová et al. [2016] fits well the observed travel times of the direct P phase. With a $v_s/v_p$ ratio of 1.71, the S phase arrival

times are approximated. Residuals of theoretical and picked P onset times were computed to evaluate the precision of origin times and locations. Along the entire travel path, the mean velocity is 5.625 km/s. Although the residuals were generally small, the alignment of traces with respect to the maximum amplitude of the direct P phase greatly improved the beam forming results.

In addition to residual calculations, the sensitivity of the beam forming results with respect to location errors was tested. Using random location errors in different error ranges indicates that relative location errors in the order of up to 50 m are not problematic, but location errors in the order of the location errors of the catalogue (100 m) can be. Because of the limited east-west resolution ($s_x$ slowness component), the obtained back azimuth can be erroneous. In case of the real data, the direct P and S phases reflected the true directions of all stations correctly (back azimuth errors below 10°).

The resemblance of waveforms was assured by visual selection of events and quantified with the calculation of cross-correlation coefficients. I observed that the different events recorded at a single station generally show greater resemblances than the recordings of one event at all stations of the receiver array. This indicates a heterogeneous subsurface beneath the receiver array and a comparably homogeneous source array volume with respect to the frequency-dependent resolution of both arrays.

After evaluating the residuals and waveform resemblance, beam forming was performed using vertical and horizontal components. The direct P and S phase are very distinct on the power stacks. While the direct P phase is strongest on the vertical component, the direct S phase is most distinct on east-west component indicating a strong SV phase. A PS phase following the direct P phase is observed on the HHE component stacks of the source array recorded on most stations. The travel time difference between this phase and the direct P phase points to a conversion in 0.6 to 0.9 km depth. Additionally, a phase arriving prior to the S phase is observed. The directional information obtained from beam forming does not fit to a SP phase of the same conversion depth. However, since the phase is rarely observed and appears in vicinity of the S phase on the vertical component, it is unsure whether the phase is an SP phase. Within the source array, P wave velocities of about 6.25 to 6.7 km/s are observed.

In addition to the first source array, which was carefully constructed from 22 selected events, a second, deeper source array was used. 12 events were selected based on two criteria only: their depth and a visible structural phase arriving about 0.85 s after the direct P phase. It remains an open questions why this phase is not visible on recordings of events shallower than about 9 km. Although the resolution of this source array is limited, the results indicate that the phase is a PP phase, reflected south-west of the source array and hence south of the direct line between source and receiver array. In order to validate

the true conversion location, a larger set of earthquakes supplemented for example by other swarms could be used. A better resolution of depth and east-west direction could be obtained from a better tridimensional distribution of events.

The performance of each receiver array station used for the source array analysis was evaluated by comparing waveforms, cross-correlation coefficients and beam forming results. The northern stations record more complex waveforms than the southern stations. While station V12 has the most complex waveforms and the least resembling records, for example stations V01 is clearly more suitable for source array beam forming. For future work I would recommend the usage of the stations located in the southern half of the receiver array. However, the reverberations of the direct P phase could be of interest when a subsurface study of the Rohrbach array area is performed.

Finally, receiver array beam forming was performed using the Rohrbach array recordings of 6 different events of the source array. The most striking result is the deviation of the theoretical and observed back azimuth. Deviations of about 15° to 30° might be explained by a geological transition between phyllite with a slower material velocity in the north and granite with a faster material velocity in the south.

## 11.2 Advantages and shortcomings of applied source array techniques

Starting a source array study might be confusing due to opposite geometries and the development of beam forming codes under the assumption of a hypothetical wave travelling from the receiver station to the source array. Although this concept might not be intuitive in the beginning it is straightforward and as fast to use as receiver array methods after being implemented once.

Source arrays have several advantages over receiver arrays: They are cheap to apply, since only one recording station is necessary and all recordings have the same receiver and subsurface transfer function. In case of the 2008/2009 swarm events the great waveform resemblance fulfils one major requirement. On the other hand, important requirements are well known origin times and locations. Therefore, source array beam forming can only be performed when exact event catalogues exist. Even if the dependence of origin times is removed, the hypocentre locations still are of great importance.

Using source arrays bears the possibility to get hold of all three components of the slowness vector. In case of my dataset, the resolution is limited due to all events being distributed on a fault plane, but this limitation could be overcome by adding events of other swarms or by using a receiver station located in different directions.

Error sources and shortcomings of the presented beam forming and localisation tech-

niques are:

- Every spatial distribution of the events of a source array defines not only the detectable wavelengths, but also defines the resolution of the slowness vector in 3-D.
- Location errors are shown to influence the results. In case of the presented source array, location errors of 100 m can result in an instability of the $s_x$ component. The events of the source array should be separated more distant than the location error range.
- Shifting for certain slowness vectors can lead to the constructive summation of the direct P or S phases of some events of the source array. These phases show up as smaller power maxima in vicinity of the optimally stacked P and S phases. Phases detected close to the onsets of the direct P and S phases should therefore be evaluated with respect to aliasing.
- In the applied beam forming and grid search techniques, a homogeneous velocity within the source array is assumed, although from a geologically point of view a homogeneous fault zone is not likely.
- The grid search method for localisation of reflections/ conversions depends on a velocity model for the entire travel path, while the analytical model even depends on a mean medium velocity. Both introduces errors to the obtained locations.
- The velocity model fitting best is a 1-D model. For a complex, anisotropic source area, a 3-D model might be necessary instead.
- With the current conversion location methods, it is assumed that all observed traces are only reflected or converted once. Multiple reflections cannot be studied.

## 11.3 Conclusion and small outlook

In conclusion, I think that the distinct beam forming results along with the striking waveform resemblance reveal the opportunities of using source arrays consisting of small swarm events for the analysis of crustal structures.

Possible future work to further expand the source array analysis of the Vogtland earthquake clusters could be the application of an extended source array, covering a larger depth range and, if possible, with a larger spreading in east-west direction. Events of other swarms could be added. A recording station east or south of the source array could be used. Differences in the results could hint to geologic features. The set-up of the source array (finding the optimal array from an earthquake catalogue) could be automatised and the variability of velocities within the source array could be implemented. Furthermore,

the source array should be analysed in combination with the receiver array. Double beam forming or a double beam migration analysis (grid search) are related approaches. Finally, the source array (or double beam) techniques could be tested on other data sets like for example on records of induced events with resembling waveforms.

## Acknowledgements

I would like to thank my supervisors apl. Prof. Frank Krüger and Dr. Matthias Ohrnberger for their steady support. They not only ignited my interest and enthusiasm for seismology in general, but also suggested this topic to me. During the work on this thesis both always had open ears and doors for ideas and questions.
I would also like to thank everyone who answered my seismology, Vogtland and/or python related questions: Torsten Dahm, Sebastian Hainzl, Sebastian Heimann, Marius Kriegerowski, Heiko Woith and others.
I wish to thank Elisabeth Schönfeldt for proof-reading and Matthias Lüthjohann for proof-reading and for *having my back* throughout my entire study and especially through writing this thesis. Last but not the least, I want to express my gratitude to my parents for supporting me during my years of study.

## Selbstständigkeitserklärung

Ich erkläre hiermit, dass ich die vorliegende Arbeit selbstständig erfasst und keine anderen als die von mir angegebenen Hilfsmittel genutzt habe.
Es handelt sich bei dieser Arbeit um meinen Erstversuch.

Potsdam, January 21, 2018

# References


Aki, K. and Richards, P. G. (2002). *Quantitative seismology*. University Science Books, Sausalito, CA, 2nd edition.

Bankwitz, P., Schneider, G., Kämpf, H., and Bankwitz, E. (2003). Structural characteristics of epicentral areas in Central Europe: study case Cheb Basin (Czech Republic). *J Geodyn*, 35:5–32.

Beyreuther, M., Barsch, R., Krischer, L., Megies, T., Behr, Y., and Wassermann, J. (2010). ObsPy: A Python Toolbox for Seismology. *Seismol Res Letters*, 81(3):530–533. doi: 10.1785/gssrl.81.3.530.

Bräuer, K., Kämpf, H., and Strauch, G. (2014). Seismically triggered anomalies in the isotope signatures of mantle-derived gases detected at degassing sites along two neighboring faults in NW Bohemia, central Europe: Seismically induced anomalies. *J Geophys Res: Solid Earth*, 119:5613–5632. doi:10.1002/2014JB011044.

Burridge, R. and Knopoff, L. (1964). Body force equivalents for seismic dislocations. *Bull Seismol Soc Am*, 54:1875–1888.

Dahm, T., Hrubcová, P., Fischer, T., Korn, J. H. M., Buske, S., and Wagner, D. (2013). Eger Rift ICDP: an observatory for study of non-volcanic, mid-crustal earthquake swarms and accompanying phenomena. *Scientific Drilling*, 16:93–99.

Dodge, D. A. and Beroza, G. C. (1997). Source array analysis of coda waves near the 1989 Loma Prieta, California, mainshock: Implications for the mechanism of coseismic velocity changes. *J Geophys Res*, 102(B11):24,437–24,458.

Fischer, T., Horálek, J., Hrubcová, P., Vavryčuk, V., Bräuer, K., and Kämpf, H. (2014). Intra-continental earthquake swarms in West-Bohemia and Vogtland: A review. *Tectonophysics*, 611:1–27.

Fischer, T., Horálek, J., Michálek, J., and Boušková, A. (2010). The 2008 West Bohemia earthquake swarm in the light of the WEBNET network. *J Seismol*, 14:665–682. doi:10.1007/s10950-010-9189-4.

Geissler, W., Kämpf, H., Seifert, W., and Dulski, P. (2007). Petrological and seismic studies of the lithosphere in the earthquake swarm region Vogtland/NW Bohemia, central Europe. *J Volcanol Geoth Res*, 159:33–69.

Geissler, W. H., Kämpf, H., Kind, R., Bräuer, K., Klinge, K., Plenefisch, T., Horalek, J., Zednik, J., and Nehybka, V. (2005). Seismic structure and location of a CO2 source in the upper mantle of the western Eger (Ohře) Rift, central Europe. *Tectonics*, 24:1–23.

Hainzl, S. (2004). Seismicity patterns of earthquake swarms due to fluid intrusion and stress triggering. *Geophys J Int*, 159:1090–1096. doi:10.1111/j.1365-246X.2004.02463.x.

Hainzl, S. and Fischer, T. (2002). Indications for a successively triggered rupture growth underlying the 2000 earthquake swarm in Vogtland/NW Bohemia. *J Geophys Res*, 107(B12):5–1–5–9. doi:10.1029/2002JB001865.

Hainzl, S., Fischer, T., and Dahm, T. (2012). Seismicity-based estimation of the driving fluid pressure in the case of swarm activity in Western Bohemia: Seismicity-based fluid pressure estimation. *Geophys J Int*, 191:271–281.

Hainzl, S., Fischer, T., Čermáková, H., Bachura, M., and Vlček, J. (2016). Aftershocks triggered by fluid intrusion: Evidence for the aftershock sequence occured 2014 in West Bohemia/Vogtland. *J Geophys Res: Solid Earth*, 121:2575–2590. doi:10.1002/2015JB012582.

Hainzl, S. and Ogata, Y. (2005). Detecting fluid signals in seismicity data through statistical earthquake modeling. *J Geophys Res*, 110:B05S071–1–10. doi:10.1029/2004JB003247.

Havskov, J. and Alguacil, G. (2010). *Instrumentation in Earthquake Seismology*. Modern Approaches in Geophysics. Springer Dordrecht Heidelberg London New York.

Havskov, J. and Ottemöller, L. (2010). *Routine Data Processing in Earthquake Seismology*. Springer Dordrecht Heidelberg London New York.

Heimann, S., Kriegerowski, M., Isken, M., Cesca, S., Daout, S., Grigoli, F., Juretzek, C., Megies, T., Nooshiri, N., Steinberg, A., Sudhaus, H., Vasyura-Bathke, H., Willey, T., and Dahm, T. (2017). Pyrocko - An open-source seismology toolbox and library. *GFZ data services*, V.0.3. doi:10.5880/GFZ.2.1.2017.001.

Heinicke, J., Fischer, T., Gaupp, R., Götze, J., Koch, U., and Konietzky, H. (2009). Hydrothermal alteration as a trigger mechanism for earhquake swarms: the Vogtland/NW Bohemia region as a case study. *Geophys J Int*, 178:1–13. doi:10.1111/j.1365-246X.2009.04138.x.

Hiemer, S. (2009). *Arrayseismologische und statistische Auswertung des Erdbebenschwarms aus dem Jahr 2008 im Vogtland/NW-Böhmen*. PhD thesis, Universität Potsdam.

Hiemer, S., Roessler, D., and Scherbaum, F. (2012). Monitoring the West Bohemian earthquake swarm in 2008/2009 by a temporary small-aperature seismic array. *J Seismol*, 16:169–182.

Hrubcová, P., Vavryčuk, V., Boušková, A., and Bohnhoff, M. (2016). Shallow crustal discontinuities inferred from waveforms of microearthquakes: Method and application to KTB Drill Site and West Bohemia Swarm Area. *J Geophys Res: Solid Earth*, 121:881–902. doi:10.1002/2015JB012548.

Hrubcová, P., Vavryčuk, V., Boušková, A., and Horálek, J. (2013). Moho depth determination from waveforms of microearthquakes in the West Bohemia/Vogtland swarm area. *J Geophys Res*, 118:120–137.

Hrubcová, P., Środa, P., Špičák, A., Guterch, A., Grad, M., Keller, G. R., Brueckl, E., and Thybo, H. (2005). Crustal and uppermost mantle structure of the Bohemian Massif based on CELEBRATION 2000 data. *J Geophys Res*, 110(B11305):1–21.

Hutko, A. R., Lay, T., and Revenaugh, J. (2009). Localized double-array stacking analysis of PcP: D" and ULVZ structure beneath the Cocos plate, Mexico, central Pacific and north Pacific. *Physics of the Earth and Planatary Interiors*, 173:60–74.

Ibs-von Seht, M., Plenefisch, T., and Klinge, K. (2008). Earthquake swarms in continental rifts - A comparison of selected cases in America, Africa and Europe. *Tectonophysics*, 452:66–77.

Krüger, F., Baumann, M., Scherbaum, F., and Weber, M. (2001). Mid mantle scatterers near the Mariana slab detected with a double array method. *Geophys Res Letters*, 28(4):667–670.

Krüger, F., Scherbaum, F., Weber, M., and Schlittenhardt, J. (1996). Analysing of Asymmetric Multipathing with a Generalization of the Double-Beam Method. *Bull Seismol Soc Am*, 86(3):737–749.

Merziger, G. (2010). *Formeln + Hilfen höhere Mathematik*. Binomi.

Mousavi, S., Bauer, K., Korn, M., and Hejrani, B. (2015). Seismic tomography reveals a mid-crustal intrusive body, fluid pathways and their relation to the earthquake swarms in West Bohemia/Vogtland. *Geophys J Int*, 203:1113–1127. doi:10.1093/gji/ggv338.

Mrlina, J., Kämpf, H., Kroner, C., Mingram, J., Stebich, M., Brauer, A., Geissler, W., Kallmeyer, J., Matthes, H., and Seidl, M. (2009). Discovery of the first Quarternary maar in the Bohemian Massif, Central Europe, based on combined geophysical and geological surveys. *J Volcanol Geoth Res*, 182:97–112.

Málek, J., Horálek, J., and Janský, J. (2005). One-dimensional qP-wave velocity model of the upper crust for the West Bohemia/Vogtland earthquake swarm region. *Stud Geophys Geod*, 49:501–524.

Niazi, M. (1969). Use of source arrays in studies of regional structure. *Bull Seismol Soc Am*, 59(4):1631–1643.

O'Brien, P. J. and Carswell, D. (1993). Tectonometamorphic evolution of the Bohemian Massif: evidence from high pressure metamorphic rocks. *Geol Rundsch*, 82:531–555.

Peterek, A., Rauche, H., Schröder, B., Franzke, H.-J., Bankwitz, P., and Bankwitz, E. (1997). The late- and post-Variscan tectonic evolution of the Western Border fault zone of the Bohemian Massif (WBZ). *Geol Rundsch*, 86:191–202.

Rietbrock, A. and Scherbaum, F. (1999). Crustal scattering at the KTB from a combined microearthquake and receiver analysis. *Geophys J Int*, 136:57–67.

Roessler, D., Hiemer, S., Bach, C., Delavaud, E., Krueger, F., Ohrnberger, M., Sauer, D., Scherbaum, F., and Vollmer, D. (2008). Rohrbach/Vogtland Seismic Array 2008, Univ. Potsdam. Deutsches GeoForschungsZentrum GFZ. Other/Seismic Network. doi:10.14470/1N934013.

Rost, S. and Thomas, C. (2002). Array Seismology: Methods and Applications. *Rev Geophys*, 40(3):2–1–2–27.

Rößler, D. (2006). Retrieval of earthquake source parameters in inhomogeneous anisotropic media with application to swarm events in West Bohemia in 2000. PhD Thesis, (Scientific Technical Report STR ; 06/09, Potsdam : Deutsches GeoForschungsZentrum GFZ).

Schenk, V., Schenková, Z., Jechumtálová, Z., and Pichl, R. (2012). Crustal deformations in the epicentral area of the West Bohemia 2008 earthquake swarm in central Europe. *J Geophys Res*, 117(B07408):1–19. doi:10.1029/2011JB009053.

Scherbaum, F., Gillard, D., and Deichmann, N. (1991). Slowness power spectrum analysis of the coda composition of two microearthquake clusters in northern Switzerland. *Physics of the Earth and Planetary Interiors*, 67:137–161.

Scherbaum, F., Krüger, F., and Weber, M. (1997). Double beam imaging: Mapping lower mantle heterogeneities using combinations of source and receiver arrays. *J Geophys Res*, 102(B1):507–522.

Shearer, P. M. (2009). *Introduction to Seismology.* Cambridge University Press, New York, 2nd edition.

Spudich, P. and Bostwick, T. (1987). Studies of the Seismic Coda Using an Earthquake Cluster as a Deeply Buried Seismograph Array. *J Geophys Res: Solid Earth*, 92(B10):10526–10546.

Ulrych, J., Lloyd, F., and Balogh, K. (2003). Age relations and geochemical constraints of Cenozoic alkaline volcanic series in W Bohemia: A review. *GeoLines*, 15:168–180.

Vavryčuk, V., Bouchaala, F., and Fischer, T. (2013). High-resolution fault image from accurate locations and focal mechanisms of the 2008 swarm earthquakes in West Bohemia, Czech Republic. *Tectonophysics*, 590:189–195.

Vavryčuk, V. and Boušková, A. (2008). S-wave splitting from records of local microearthquakes in West Bohemia/ Vogtland: An indicator of complex crustal anisotropy. *Stud Geophys Geod*, 52:631–650.

Weckmann, U., Muñoz, G., Pek, J., Meqbel, N., Kováčiková, S., and Klanica, R. (2016). Earthquake swarms, Mofettes and mid Pleistocene volcanism - Electromagnetic imaging of the Eger Rift (W Bohemia). Abstract T33C-3037 presented at 2016 Fall Meeting, AGU, San Francisco, Calif., 12-16 Dec.

Wessel, P., Smith, W. H. F., Scharroo, R., Luis, J. F., and Wobbe, F. (2013). Generic Mapping Tools: Improved version released. *EOS Trans. AGU*, 94:409–410.

*The seismic data was processed using the python packages ObsPy [Beyreuther et al., 2010] and Pyrocko [Heimann et al., 2017]. The maps were created using the Generic Mapping Tools (GMT) [Wessel et al., 2013] and Google Earth. Figures were edited using the open-source vector graphics editor Inkscape. This report was written with the LaTeX editor Texmaker.*

# Appendix

## Supplementary material on CD

The self-written python code and additional figures are provided as supplementary material on the attached disc as well as the waveform data of the source array events. Additionally a poster, which was presented at the annual meeting of the AG Seismologie in Bad Breisig, Sept. 26.-28. 2017 is included.

### Python code

Eight python programs are provided on the CD. The following list shortly summarizes their purpose.

- *xcorr_SA_final+Loop.py* was written to determine the resemblance of waveforms. For each station in the list 'stations' the maximum cross-correlation coefficients of each event pair on one defined component (HHE, HHN or HHZ) is calculated. The length of the time window, a number of shifts and a bandpass filter can be adjusted. For every station one plot is prepared and saved showing the cross-correlation coefficients of each event-pair.

- *difftime.py* contains three functions to calculate shift times based on the slowness vector of a plane wave and the locations of each event of a source array plus the location of the reference event.

- *beamforming_parstack_newSA_allStats_rel2P.py*: Beamforming program as described in section 6.3.

- *beamforming_parstack_PLOTTING_SA.py*: Plot results of (3).

- *conversion-points_16JUL.py*: Calculate conversion location as described in section 7.1.

- *Grid-Seach_with_velMod,realData,Palignment_SA.py*: Migration-like grid search method for determination of location with highest probability of a conversion, workflow described in section 7.2.

- *Grid-search_result_Plot_expl.py*: Plot results of grid search.

- *plot_traces_shifted-by-slowness-vector.py*: Small program to shift traces according to a defined slowness vector. Used to check aliasing effects (cf. sec. 9.4).

## Source array - residuals of obs. and theor. arrival times

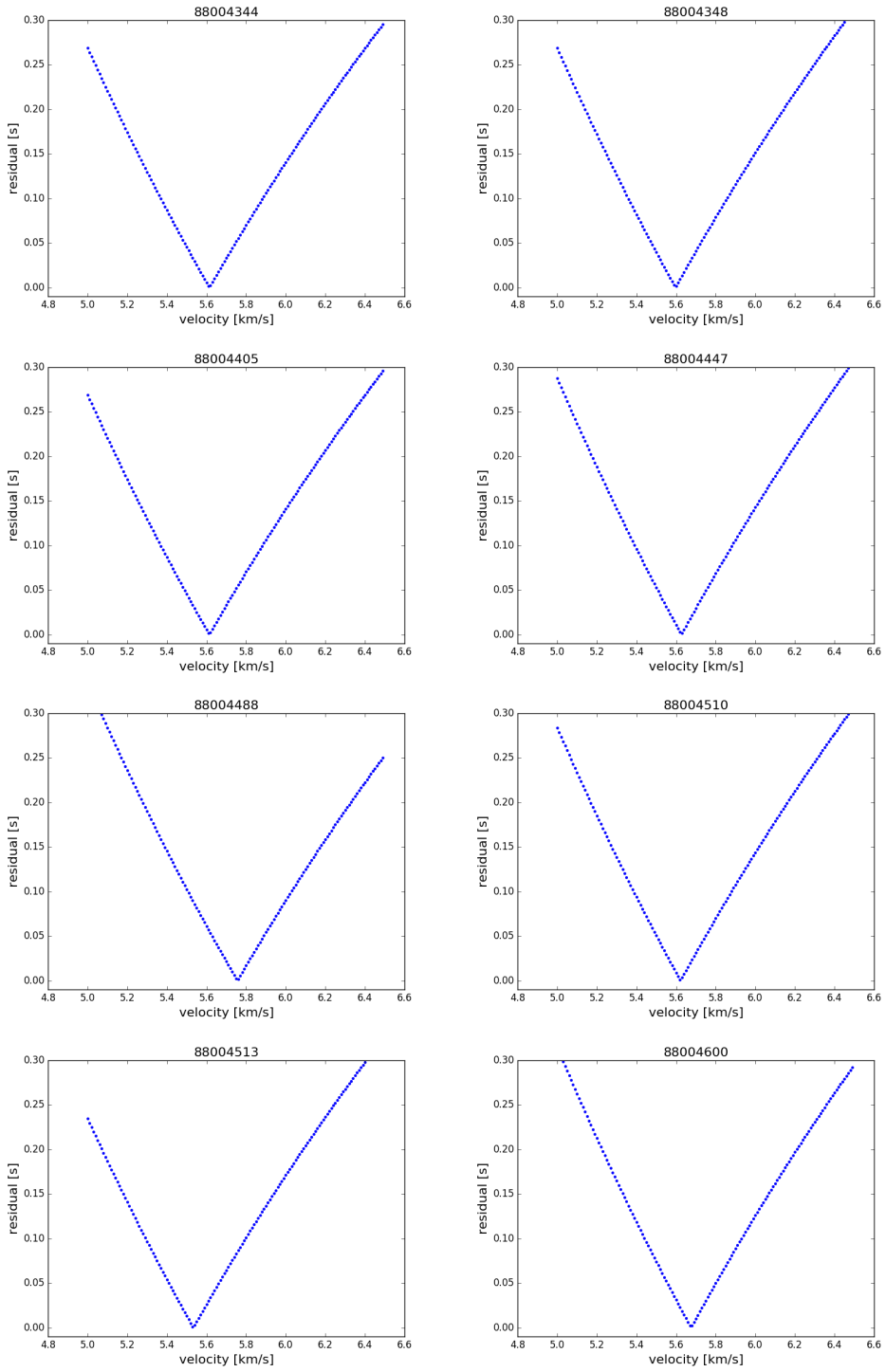


Figure 48: Difference between picked and theoretical P wave travel time for different velocities.

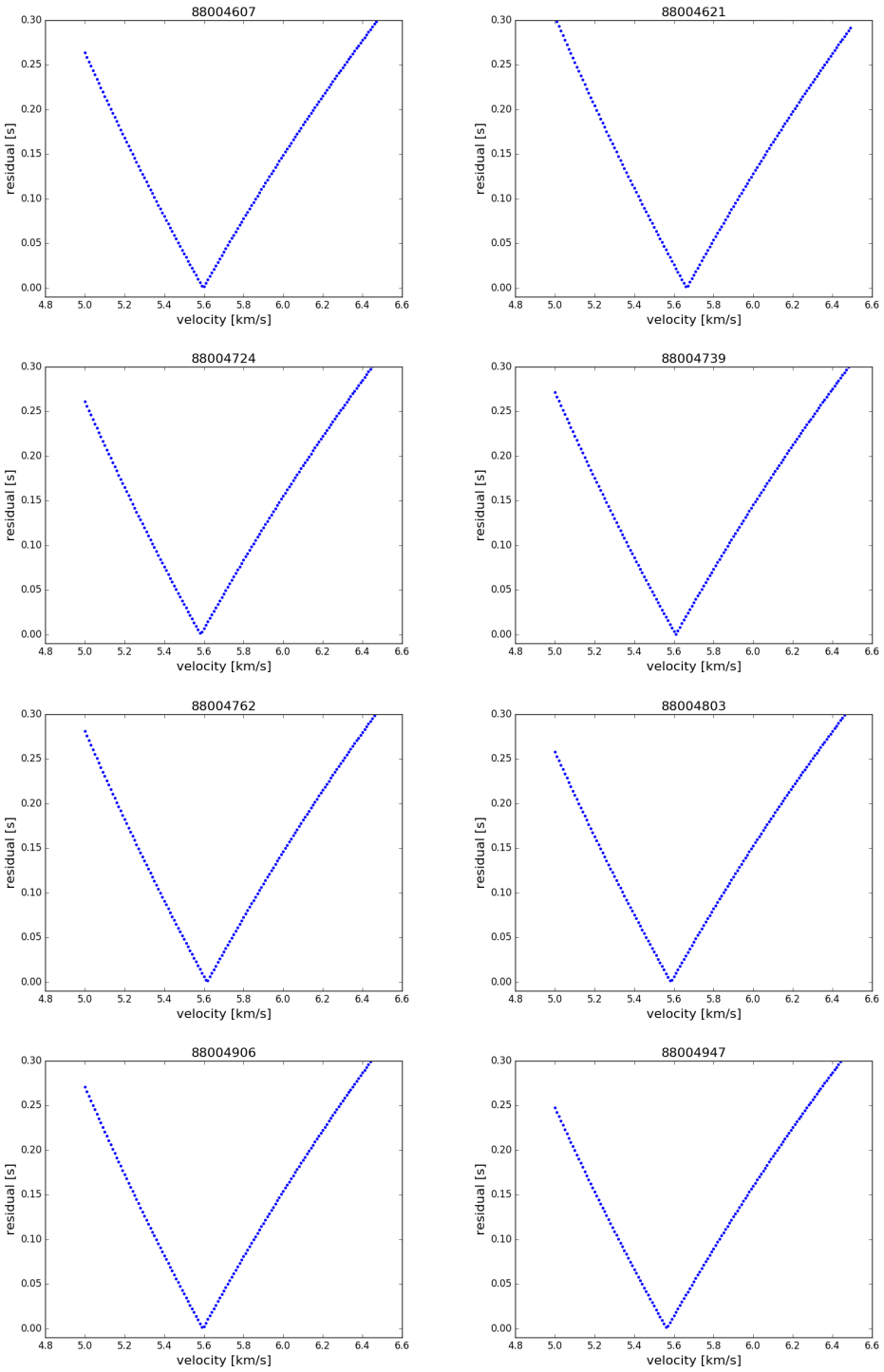


Figure 48: (cont.)

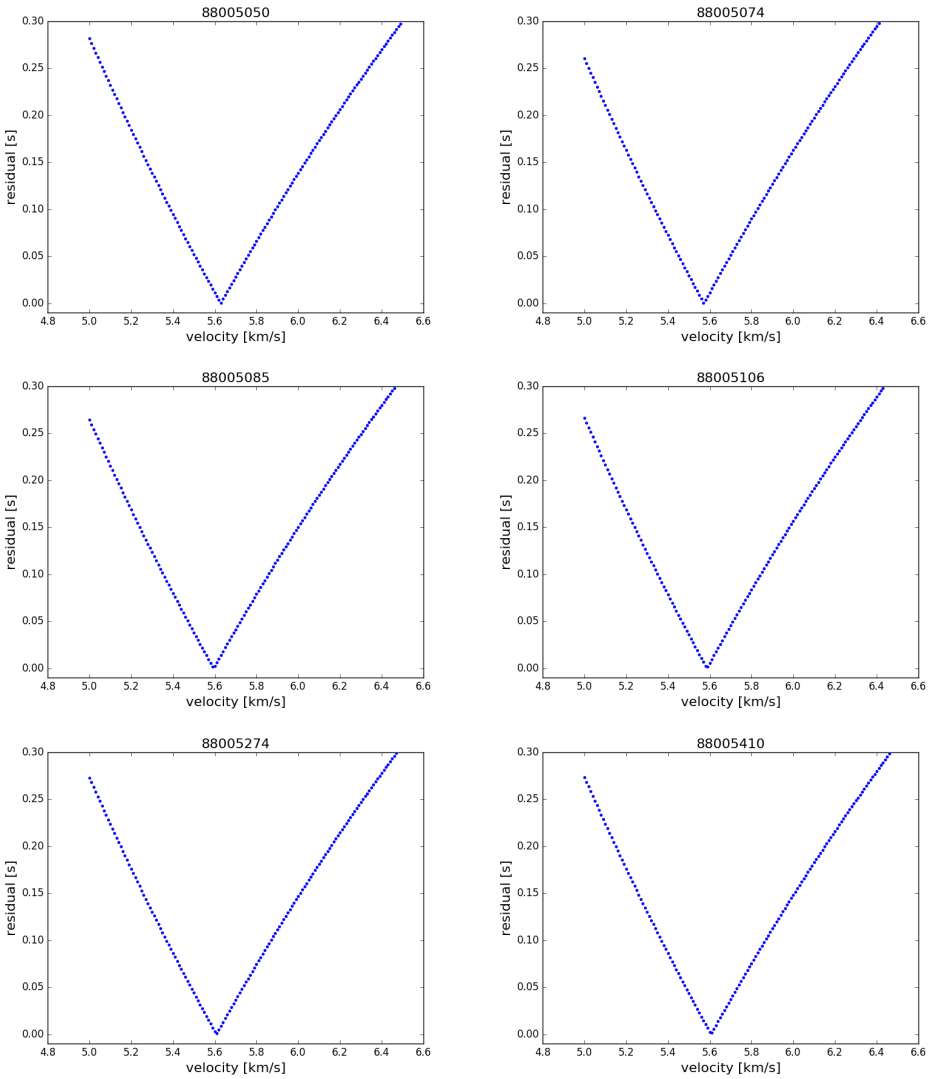


Figure 48: (cont.)

## Cross-correlation analysis for different frequency ranges

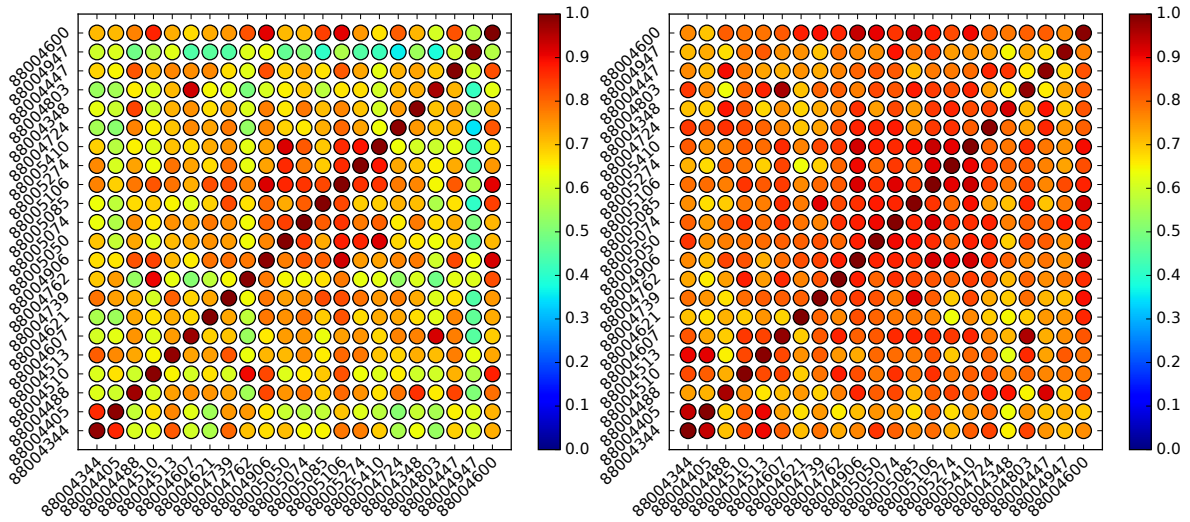

(a) V04 (b) V01

Figure 49: Maximum cross-correlation coefficients for source array recorded at station V04 (a) and V01 (b), obtained in ±0.2 s time windows around the picked P onsets. Traces were normalized and bandpass filtered from **1 to 100 Hz**. While the cross-correlation coefficients for this wide filter is clearly decreased compared to narrower bandwidths, the coefficients are still unexpectedly high on some stations (here seen at station V01).

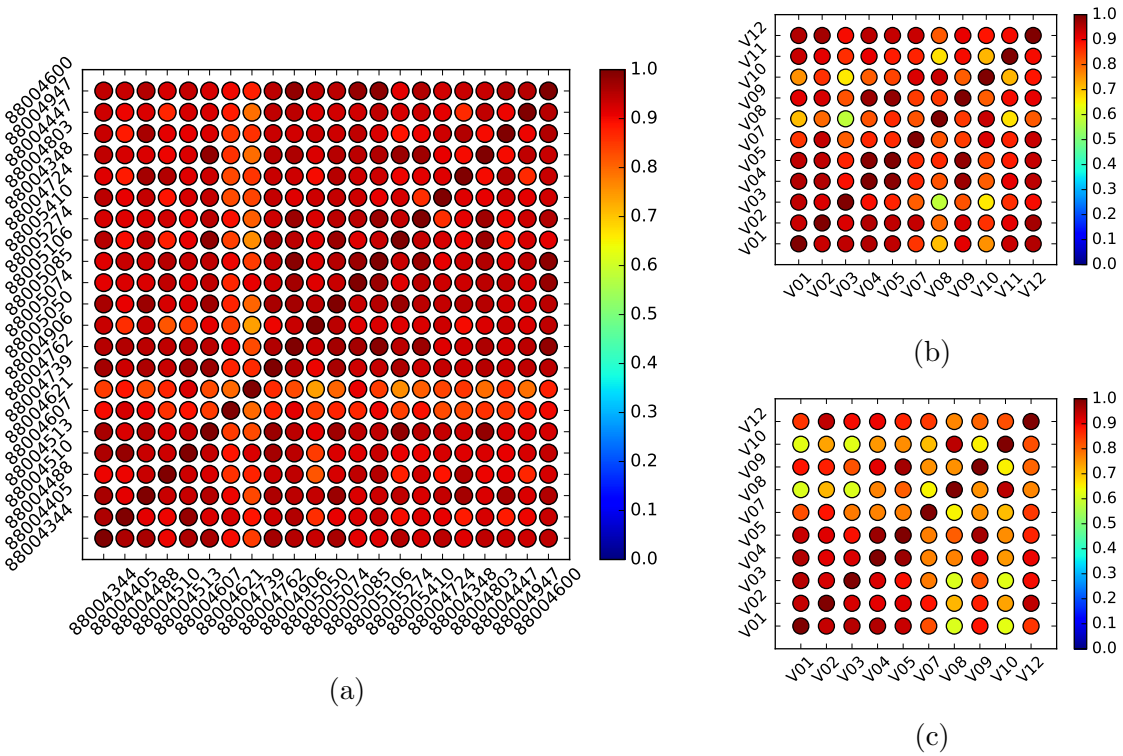


Figure 50: Maximum cross-correlation coefficients for source array recorded at station V01 (a) and for receiver array stations recordings of events 88004621 (2008-10-28 10:08:05.020 M 1.5)(b) and 88005106 (2008-11-08 23:11:55.240 M 0.4) (c), obtained in ±0.2 s time windows around the picked P onsets. Traces were normalized and bandpass filtered from **1 to 30 Hz**.

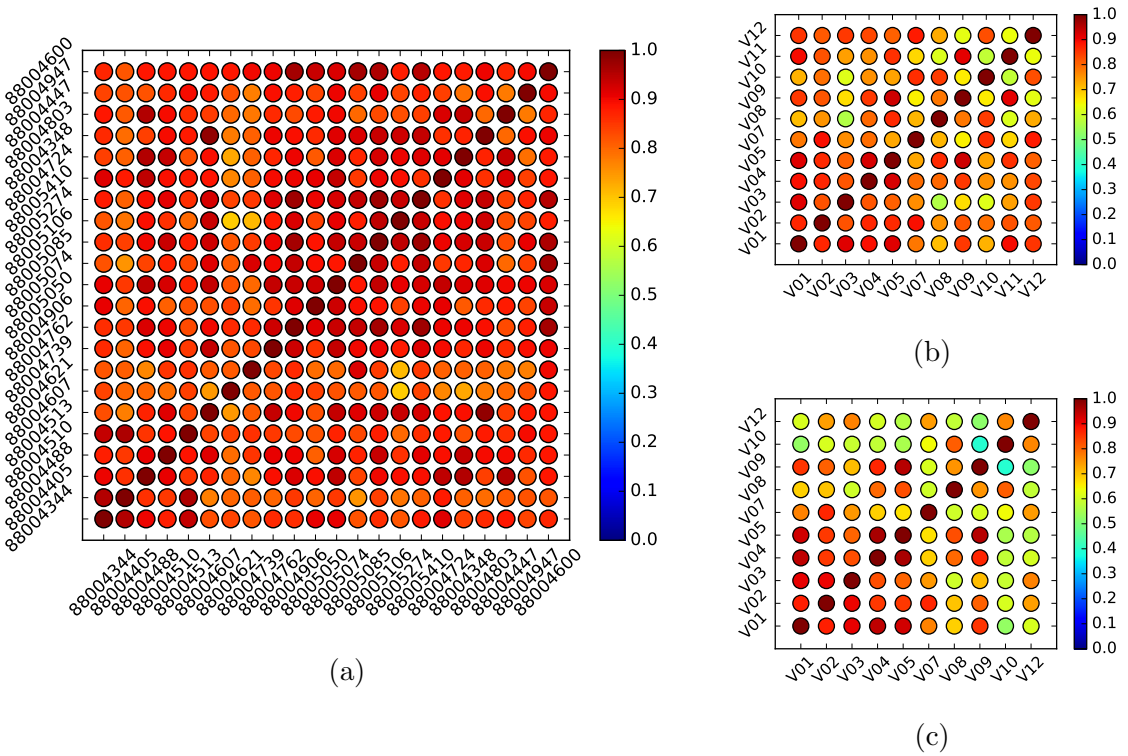


Figure 51: Same as Fig. 50, bandpass filtered from **1 to 40 Hz**.

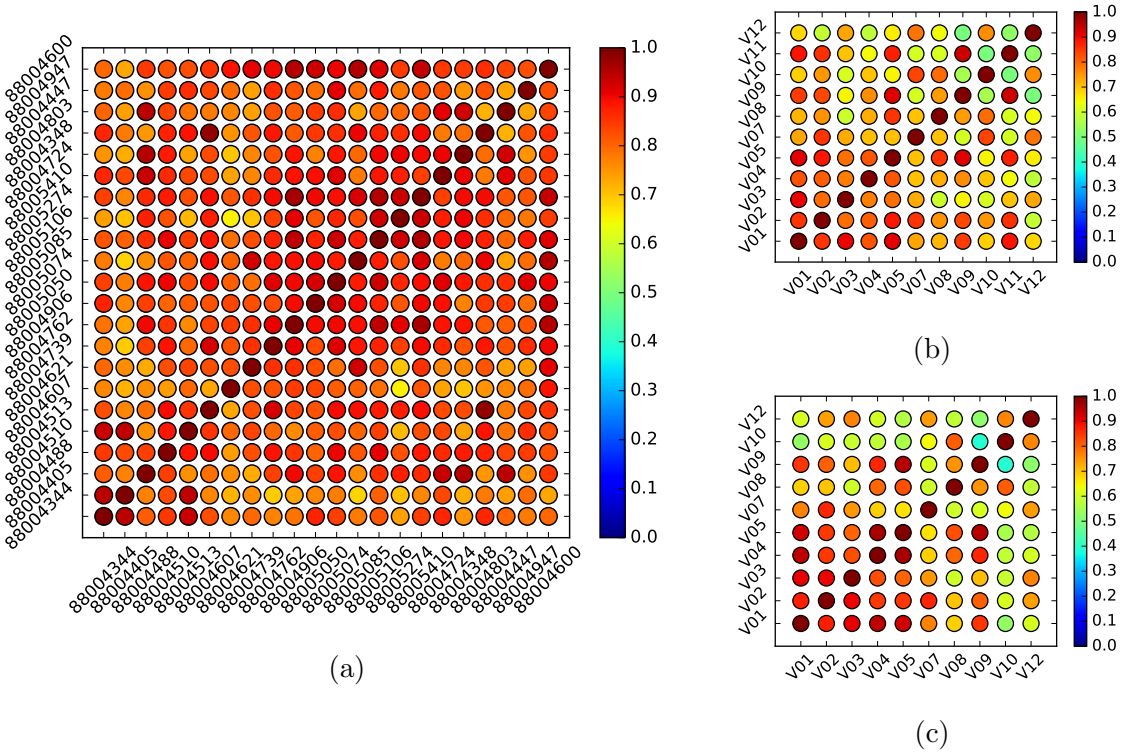


Figure 52: Same as Fig. 50, bandpass filtered from **1 to 50 Hz**.

## Beam forming results

### Source array

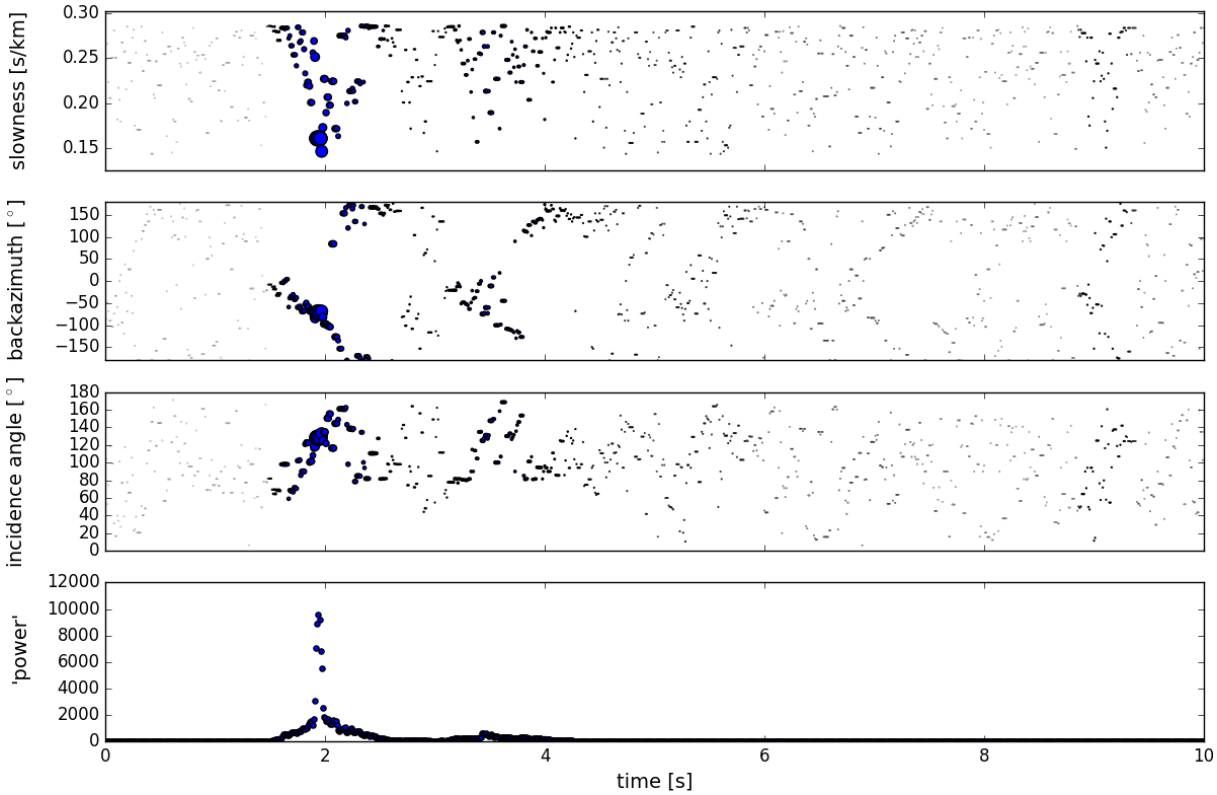


(a) HHZ

Figure 53: Results for station V05 (source array), traces were aligned relative to P amplitude maximum and shifted back according to a theoretical slowness vector prior to beam forming. Time step 0.01 s, window length 0.05 s, bandpass filter 1-60 Hz. (a) HHZ, (b) HHN and (c) HHE component.

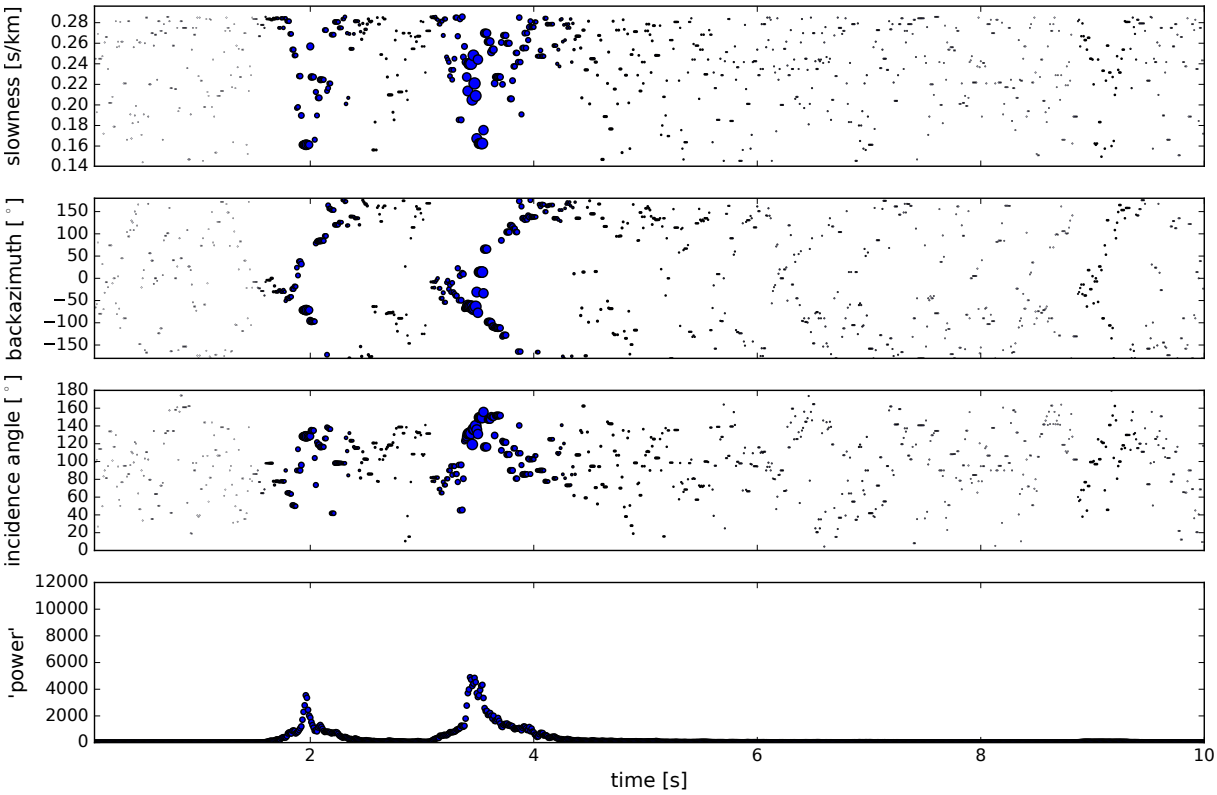


(b) HHN

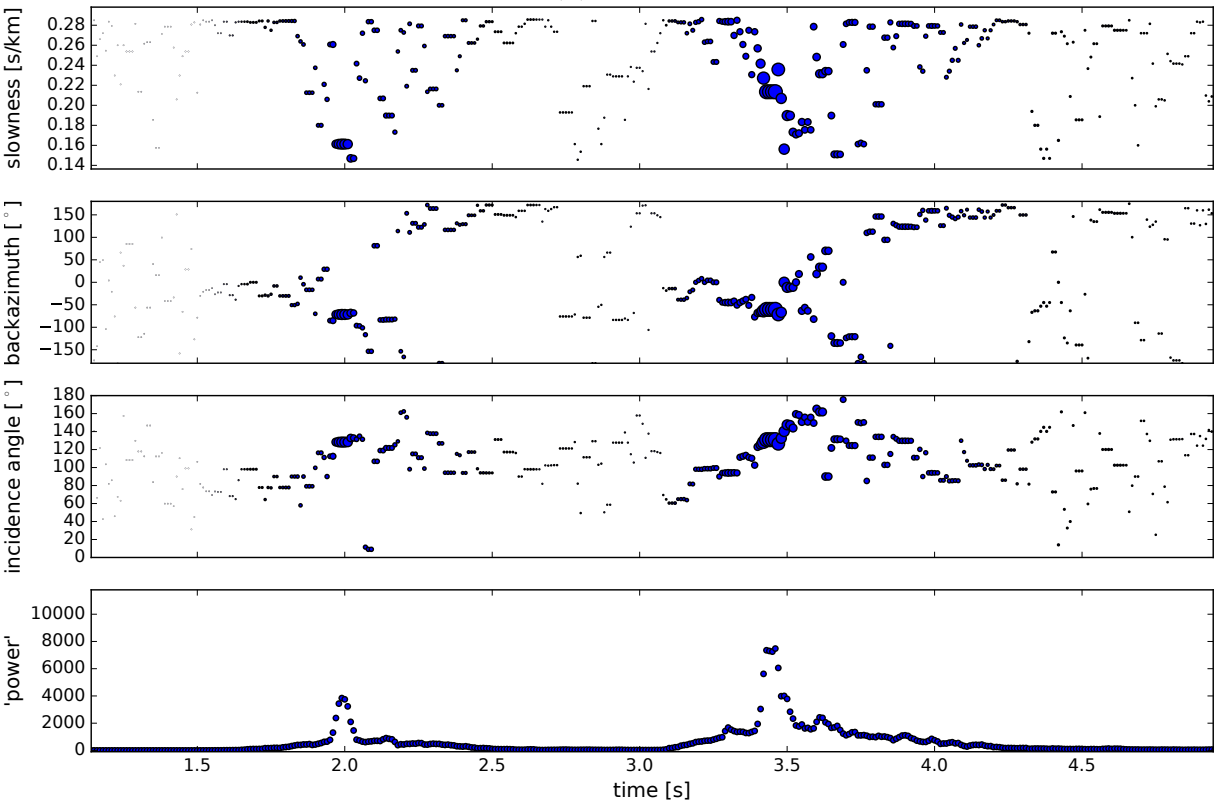


(c) HHE

Figure 53: cont.

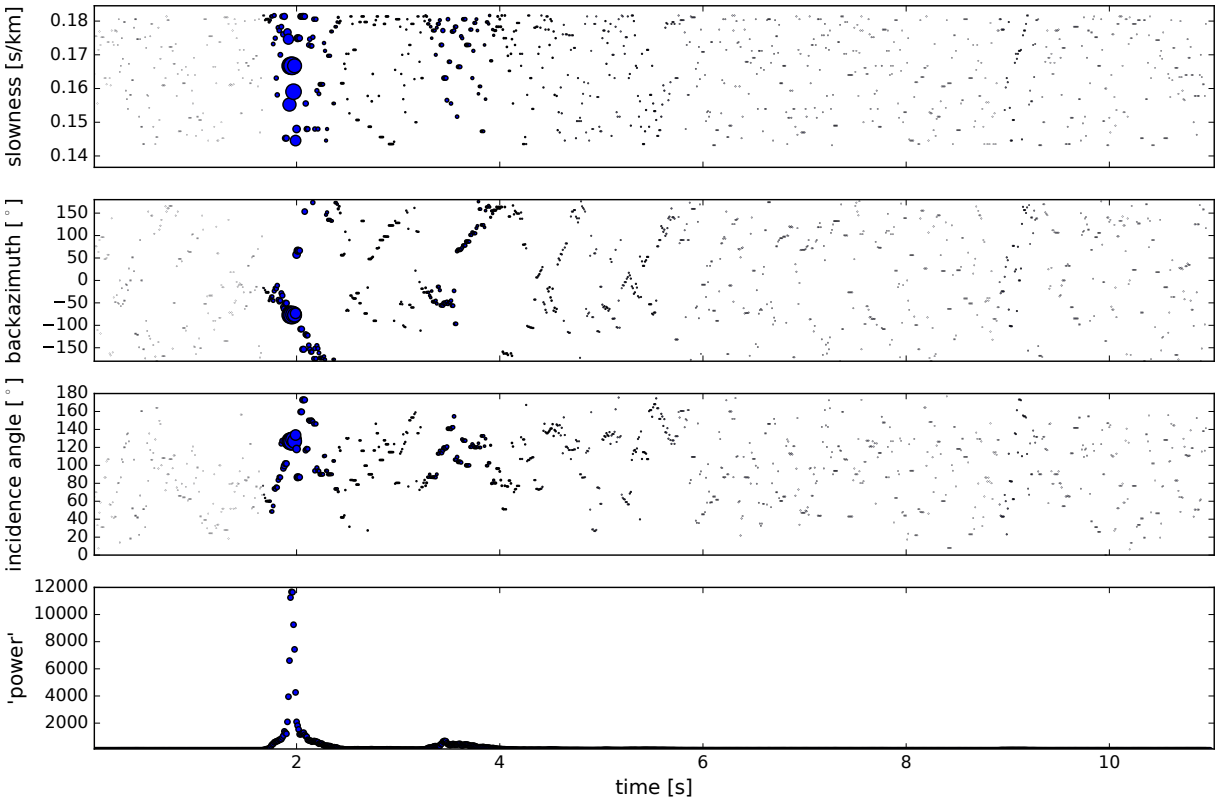


(a) HHZ

Figure 54: Results for station V02 (source array), traces were aligned relative to P amplitude maximum and shifted back according to a theoretical slowness vector prior to beam forming. Time step 0.01 s, window length 0.05 s, bandpass filter 1-60 Hz. (a) HHZ, (b) HHN and (c) HHE component.

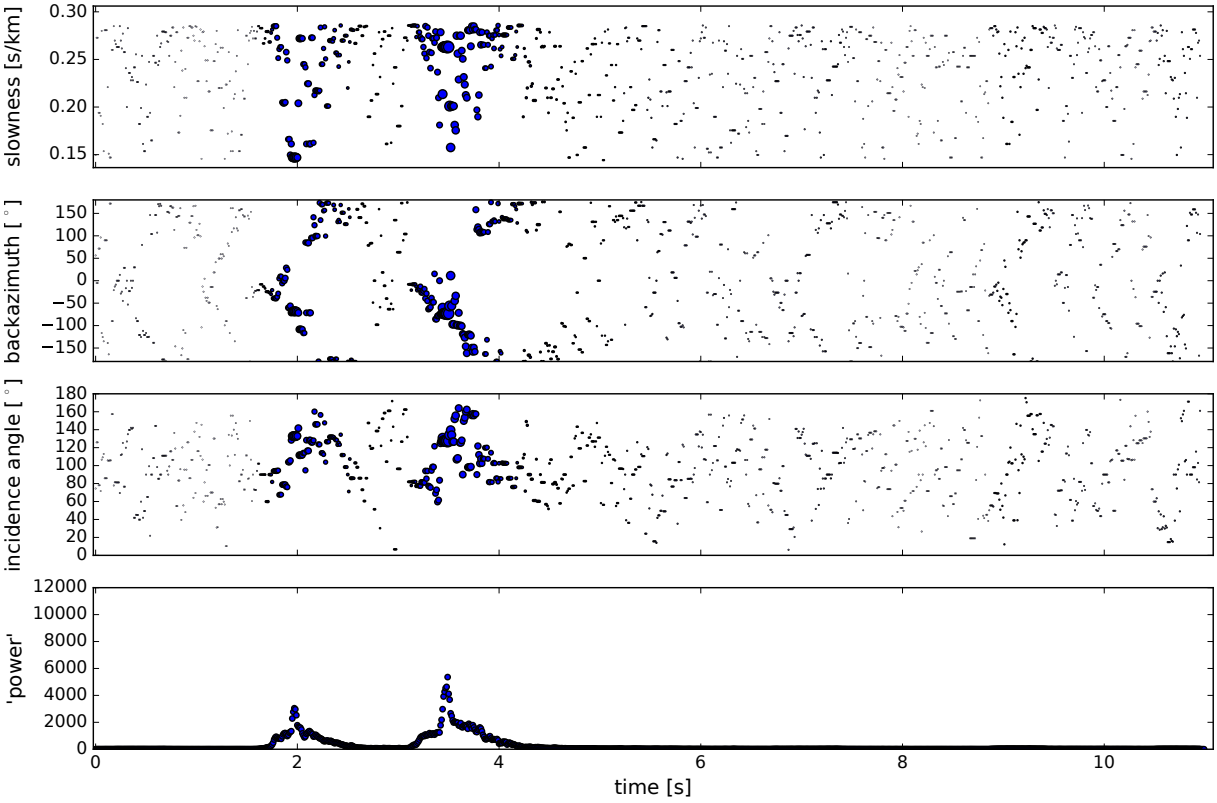


(b) HHN

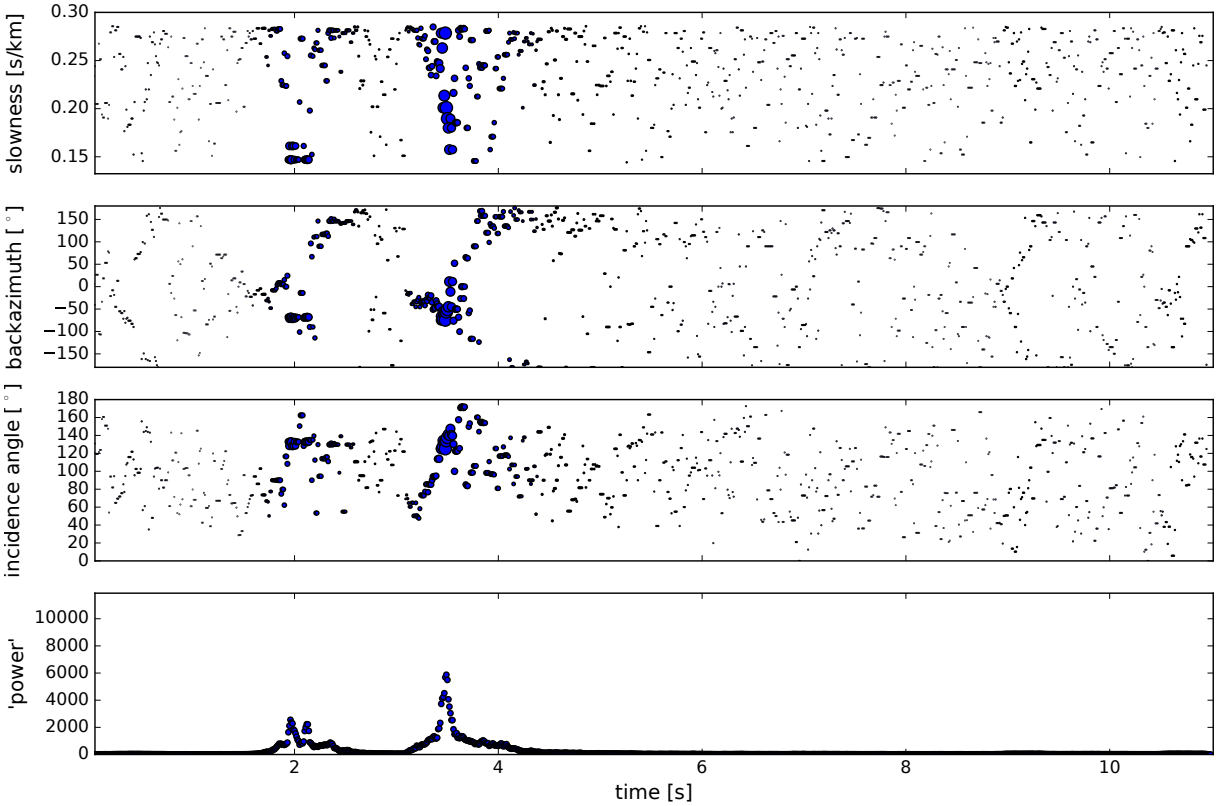


(c) HHE

Figure 54: cont.

### Receiver array

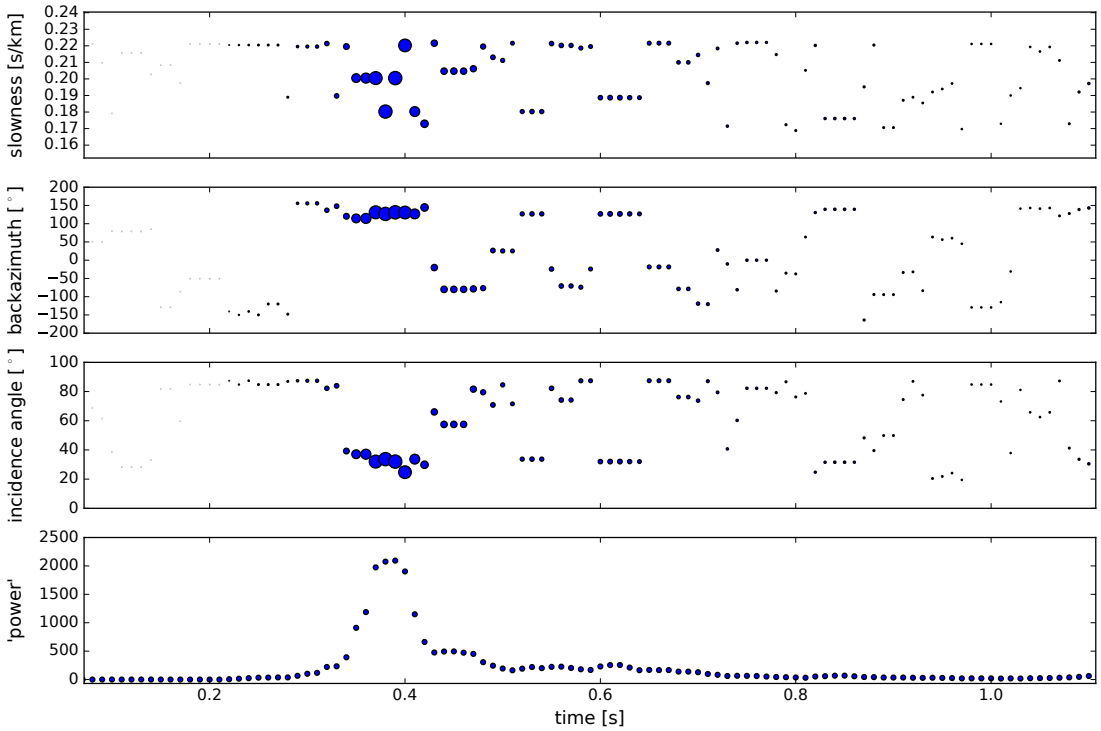


(a)

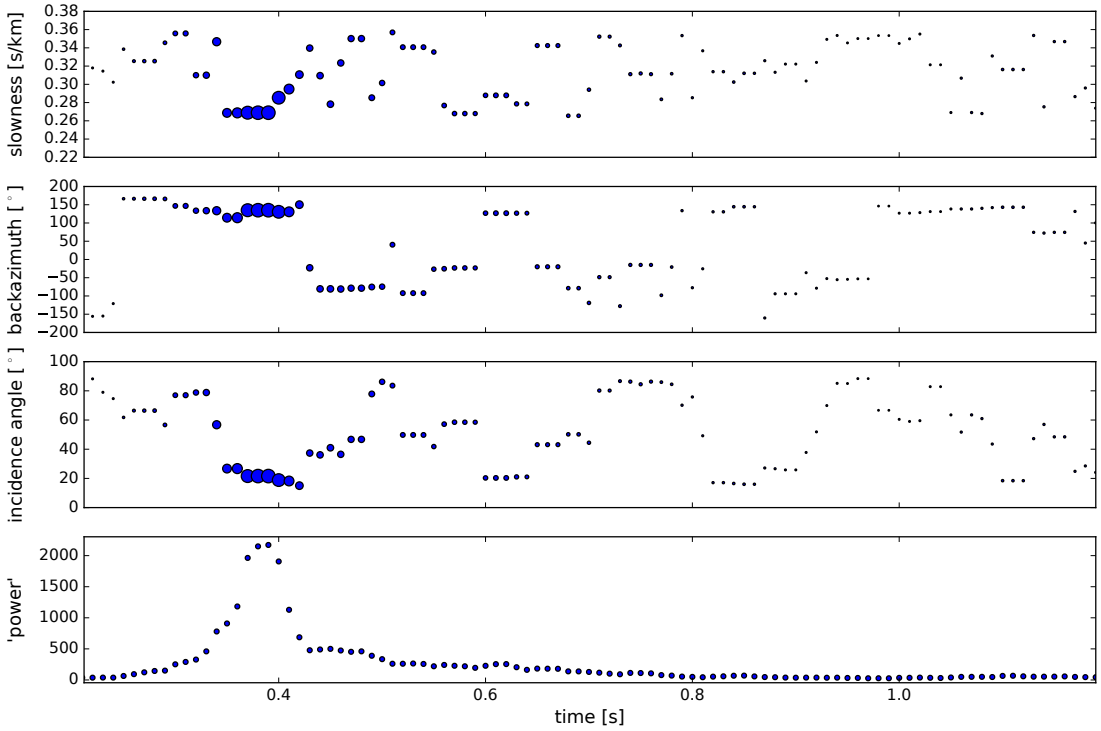


(b)

Figure 55: Beam forming results for event 88004344 (receiver array). Time step 0.01 s, window length 0.05 s. Beam forming with (a) P wave and (b) S wave velocities.

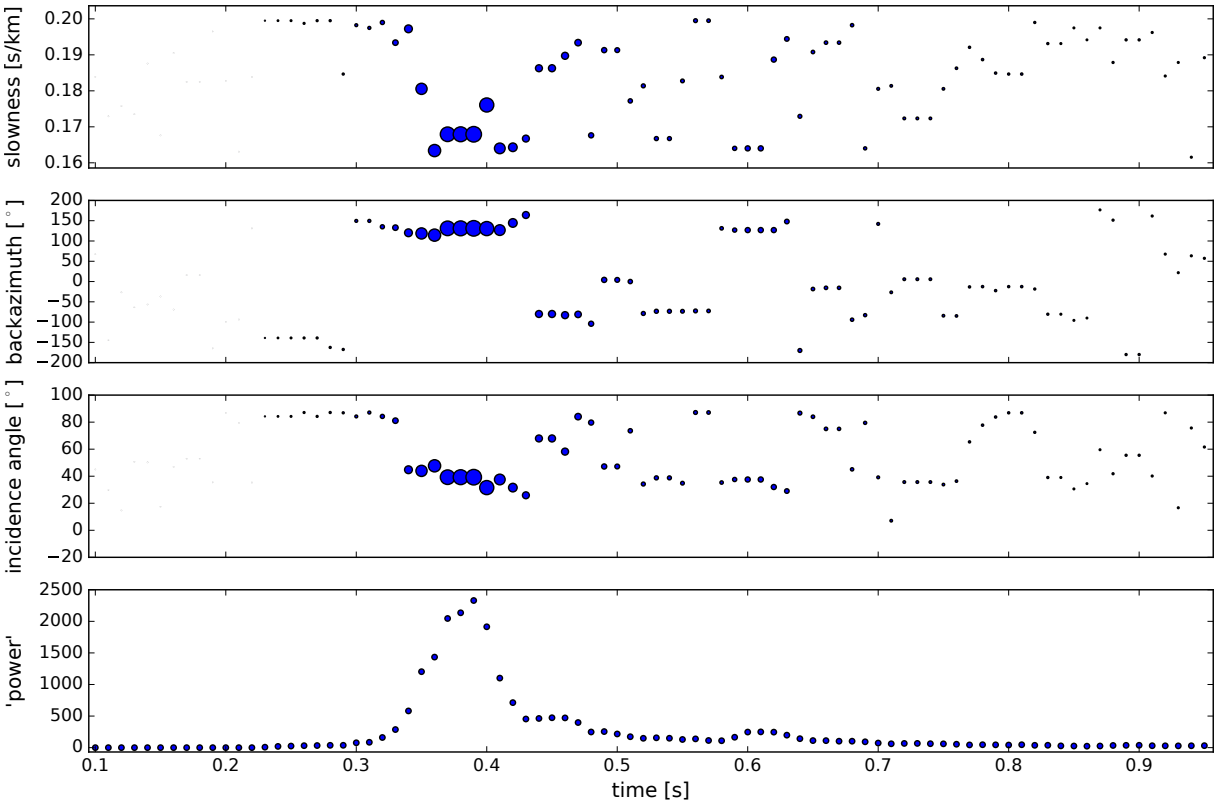


(a)

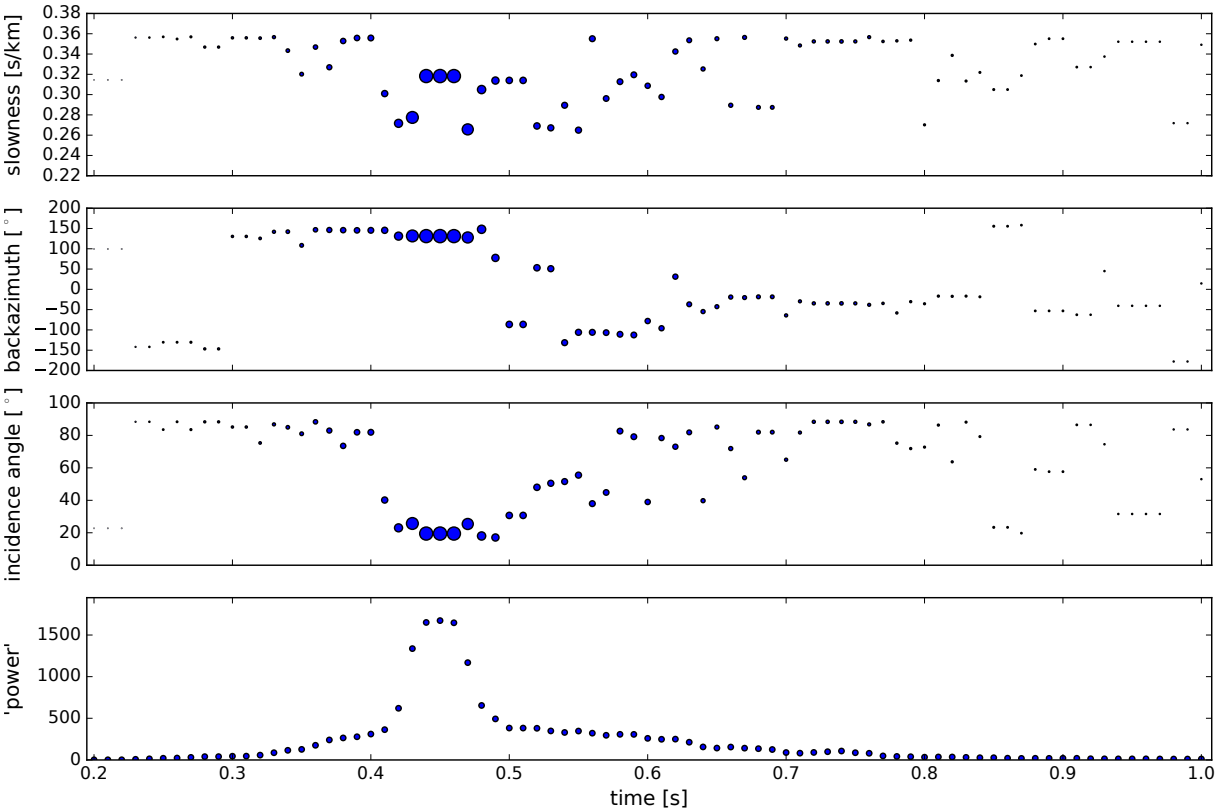


(b)

Figure 56: Beam forming results for event 88004405 (receiver array). Time step 0.01 s, window length 0.05 s. Both plots show P-coda, beam forming with (a) P wave and (b) S wave velocities (for detection of SP phases).

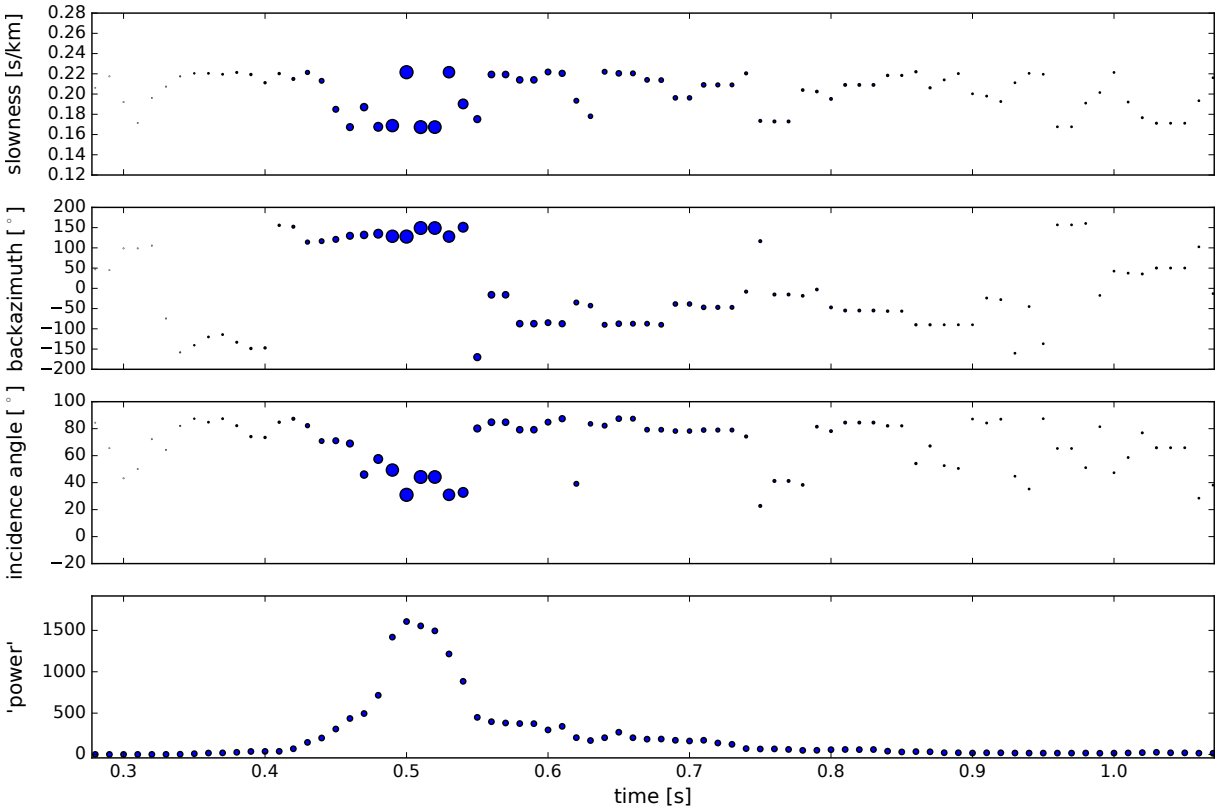


(a)

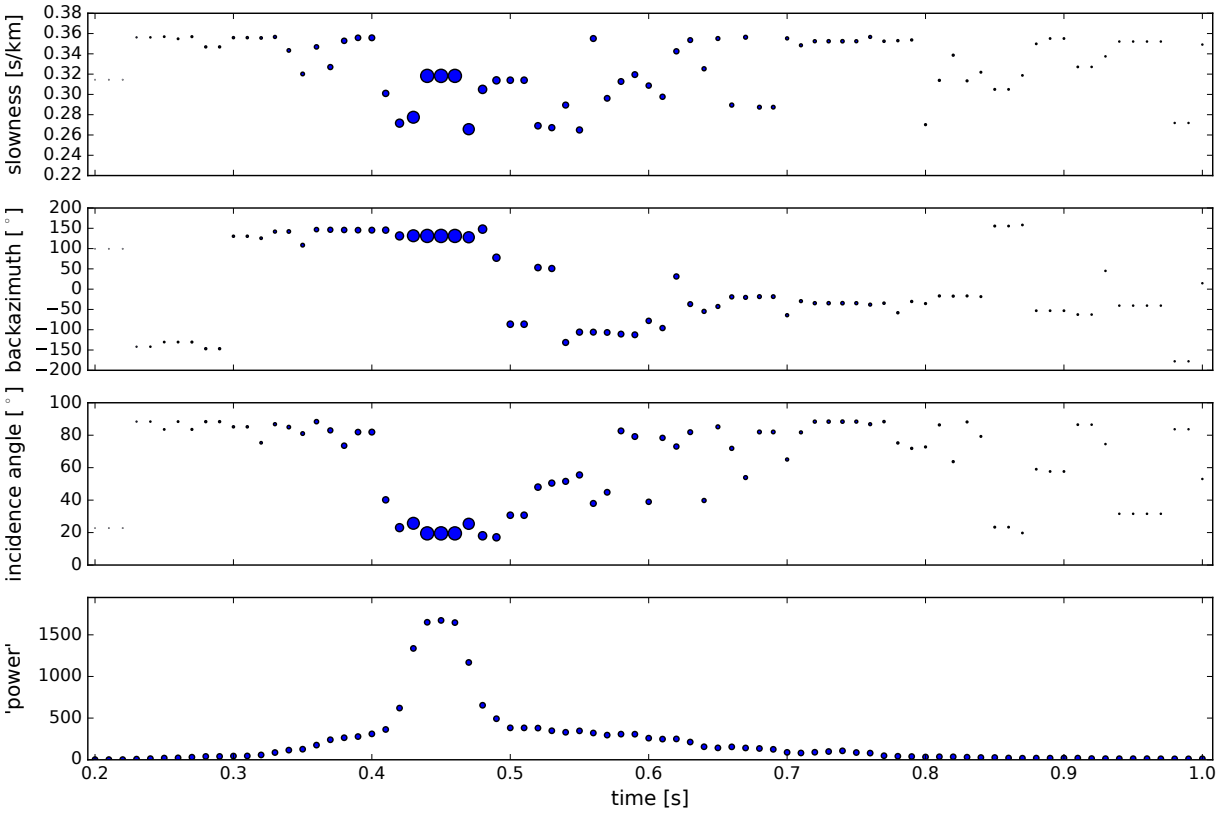


(b)

Figure 57: Beam forming results for event 88004621 (receiver array). Both plots show P-coda, beam forming with (a) P wave and (b) S wave velocities (for detection of SP phases).

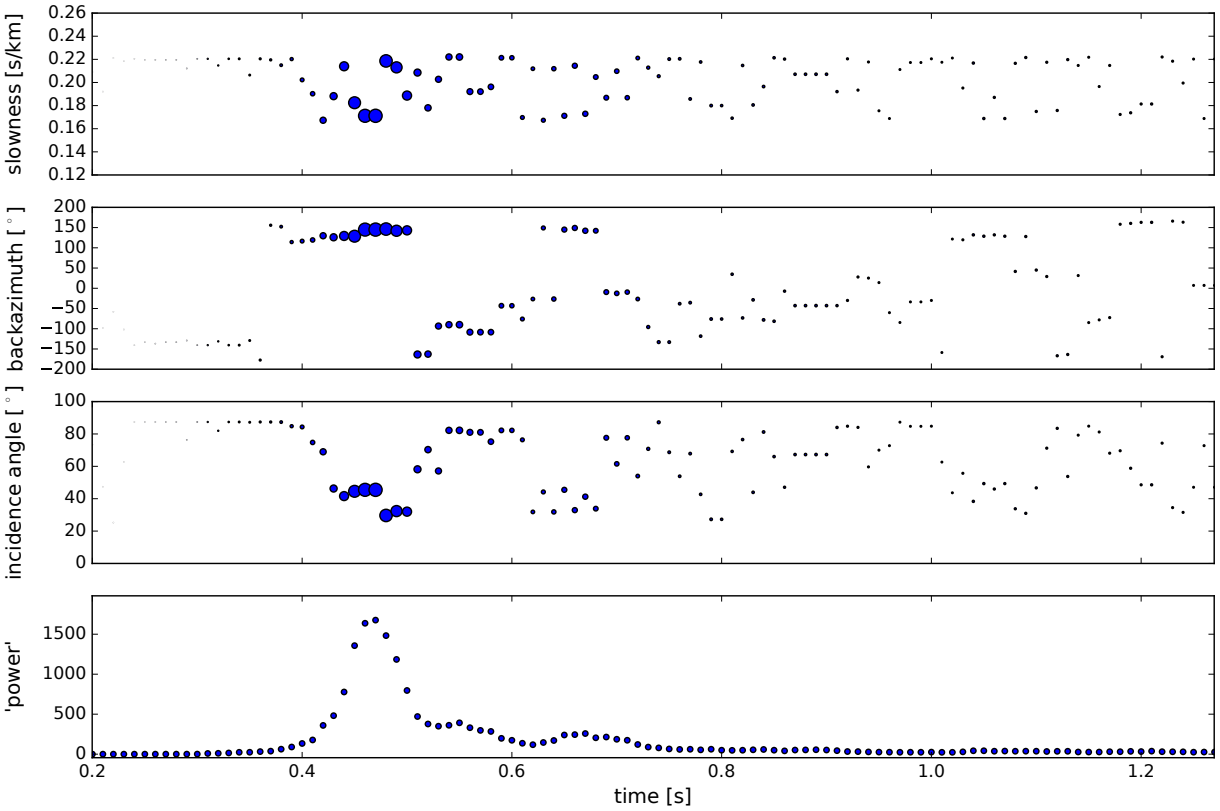


(a)

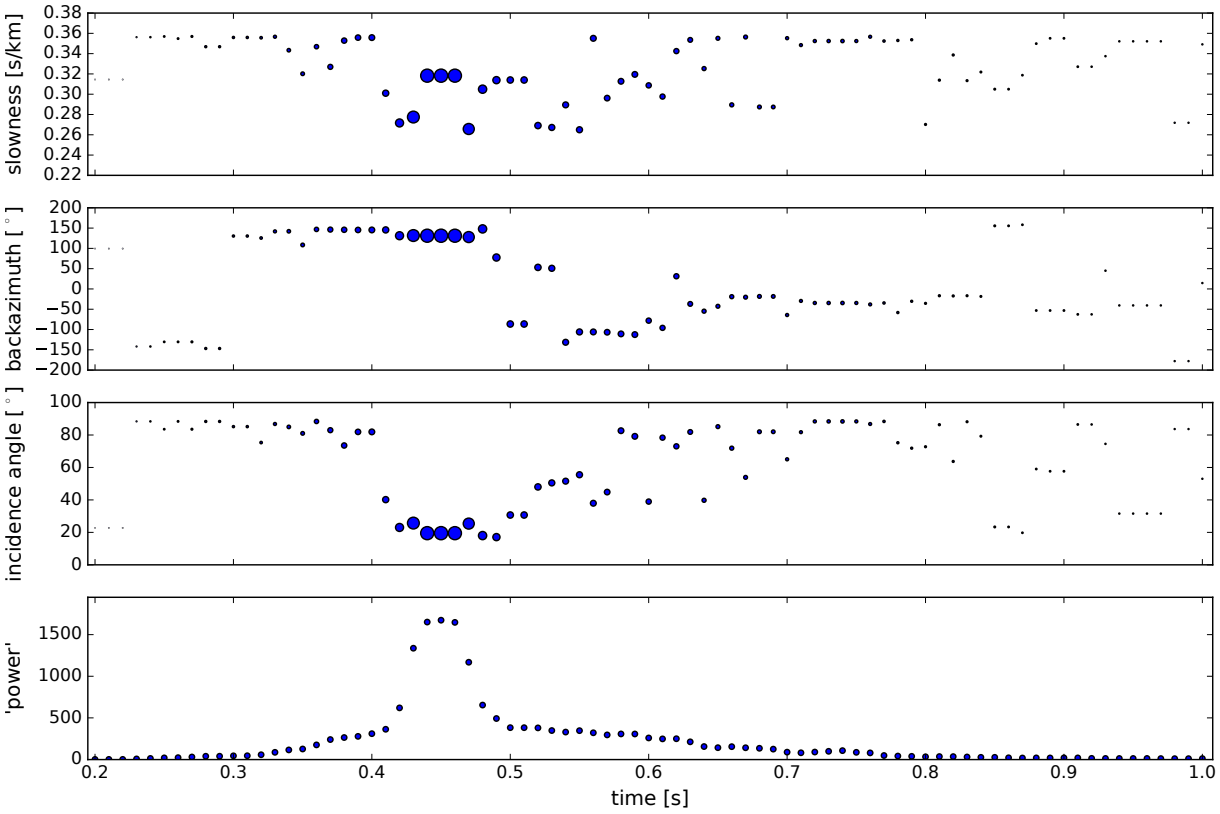


(b)

Figure 58: Beam forming results for event 88004488 (receiver array). Both plots show P-coda, beam forming with (a) P wave and (b) S wave velocities (for detection of SP phases).

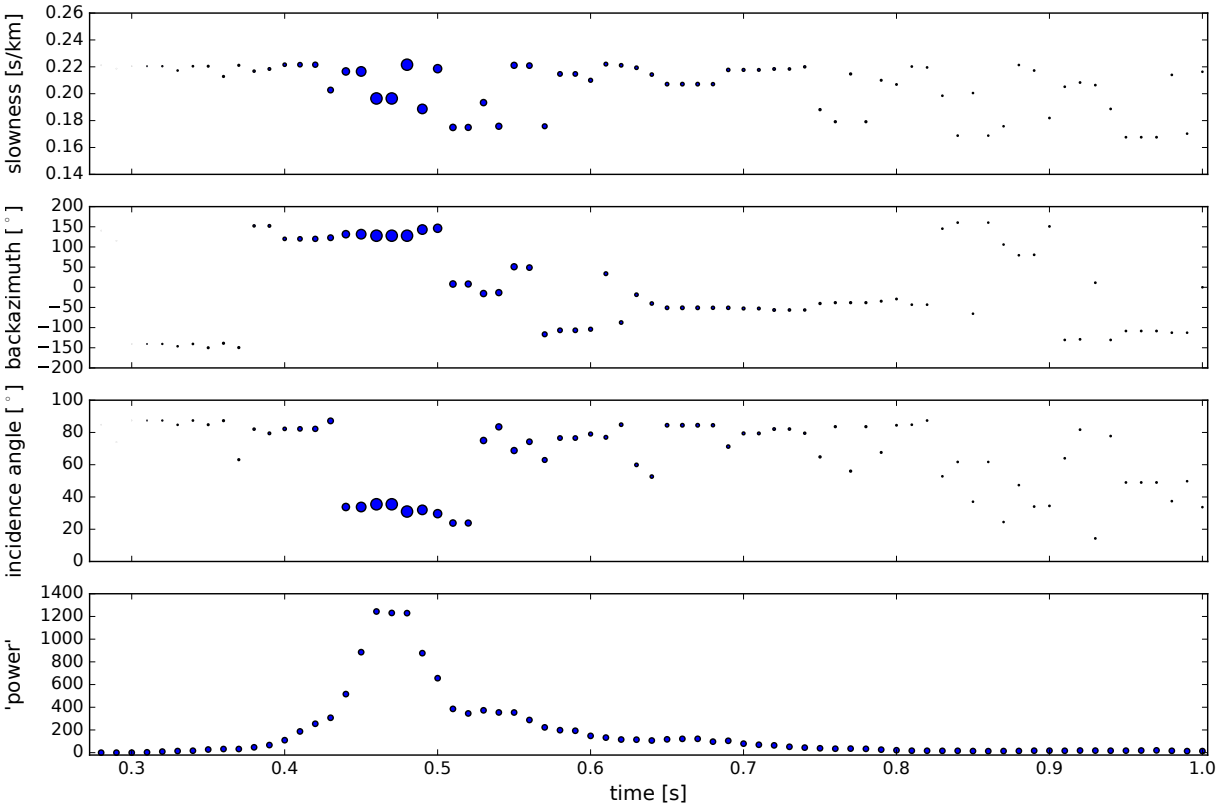


(a)

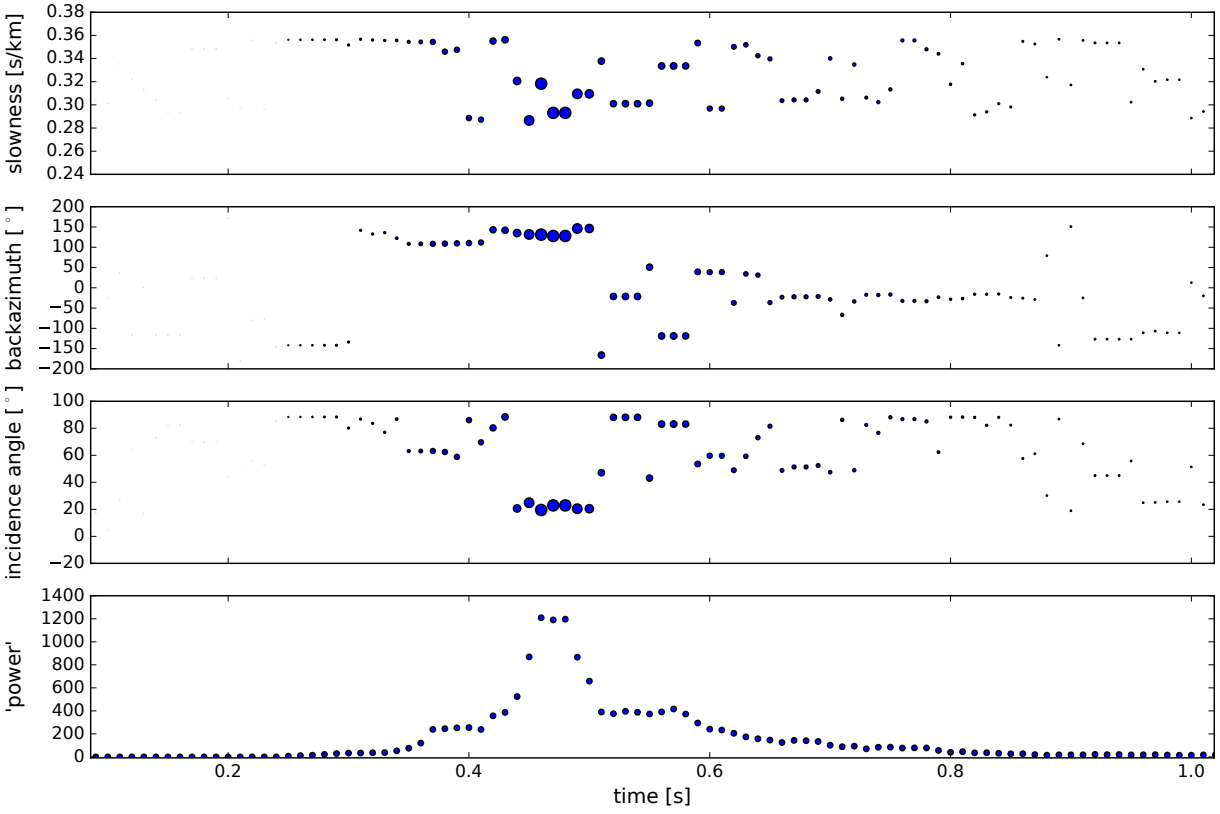


(b)

Figure 59: Beam forming results for event 88005106 (receiver array). Both plots show P-coda, beam forming with (a) P wave and (b) S wave velocities (for detection of SP phases).

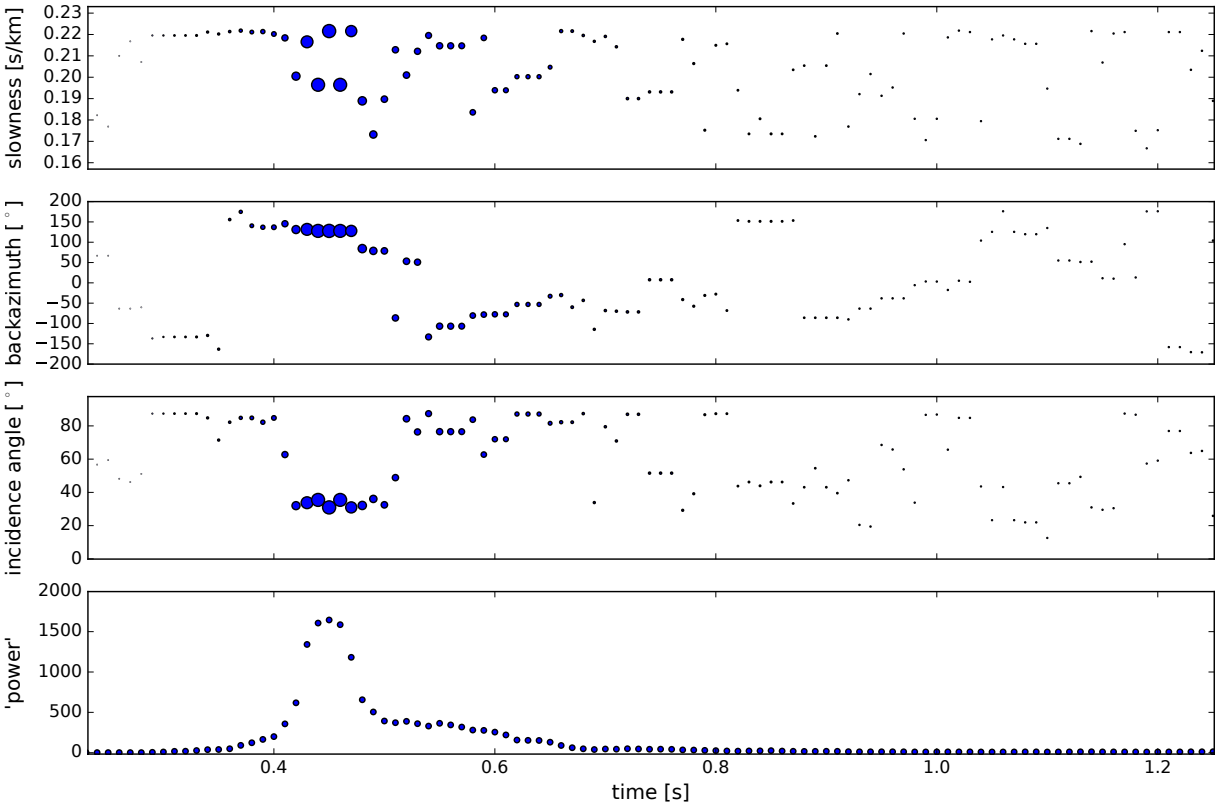


(a)

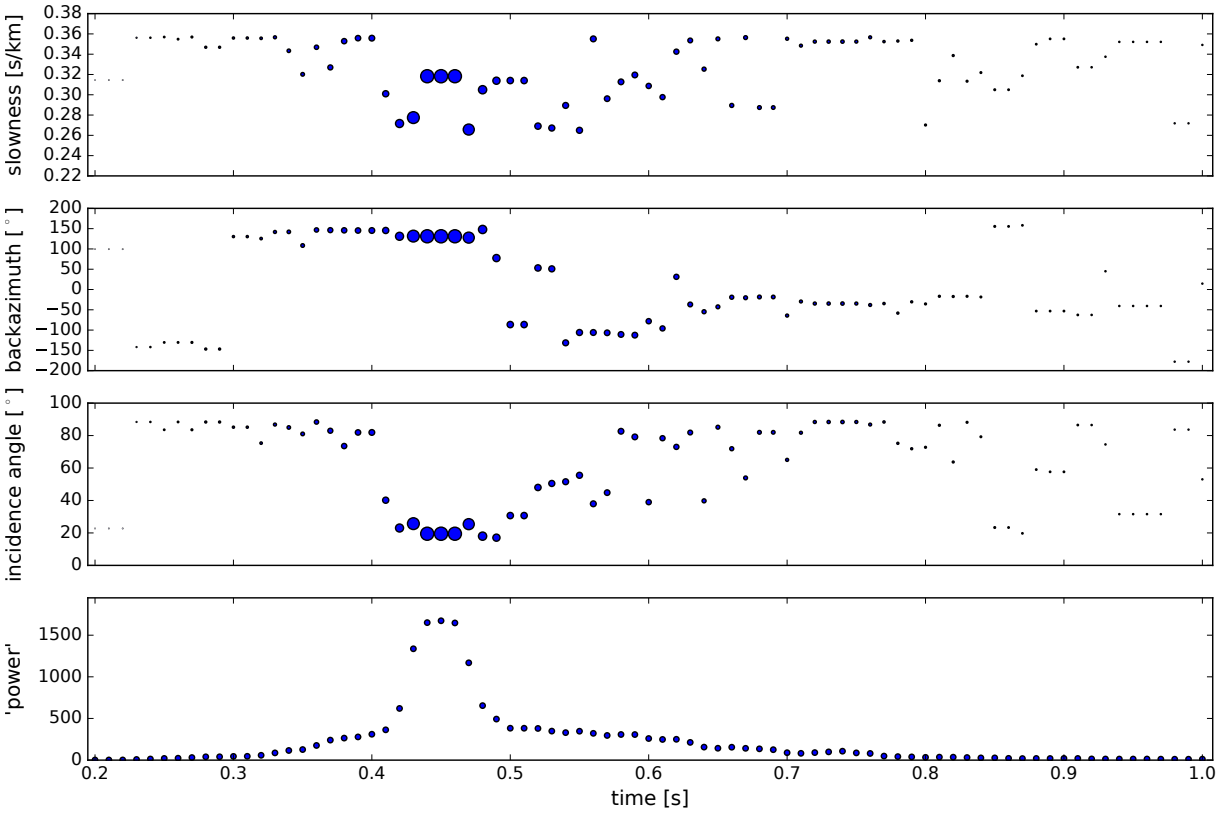


(b)

Figure 60: Beam forming results for event 88005410 (receiver array). Both plots show P-coda, beam forming with (a) P wave and (b) S wave velocities (for detection of SP phases).

## Poster AG Seismologie

The results of this thesis were presented at the annual meeting of the AG Seismologie in Bad Breisig, Sept. 26-28 2017 as a poster presentation. The poster is shown on the next page and in full resolution part of the supplementary material on the CD.

# Source Array analysis of Vogtland earthquake clusters

G. M. Petersen (gpeterse@uni-potsdam.de), F. Krüger, M. Ohrnberger
Inst. für Erd- und Umweltwissenschaften, Universität Potsdam

## Key questions:

- **Can the swarm eathquakes be used for source array analysis of the subsurface?**
- **Are the recorded waveforms similar enough (without deconvolution)?**
- **How sensitive are the beam forming results to location errors and imprecise origin times?**
- **Are structural phases detected?**

## Vogtland

The Vogtland, located at the border region between Czech Republic and Germany, is known for Holocene volcanism, gas and fluid emissions as well as for reoccurring earthquake swarms, pointing towards a high geodynamic acitivity. Since 1985, seismic activity is concentrated at the Nový Kostel focal zone (Fischer et al., 2014). For this study, data of the 2008/2009 swarm was used (Roessler et al., 2008).

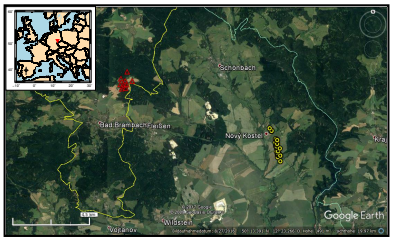


Fig. 1: Location of the Vogtland area (small map) and aerial view of the source array epicentres (yellow circles) and receiver array stations of the Rohrbach array (red triangles).

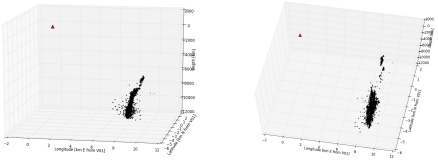

Fig. 1: The hypocentres of the 2008/2009 earthquake swarm are located on a N-S striking fault plane (catalogue by T. Fischer).

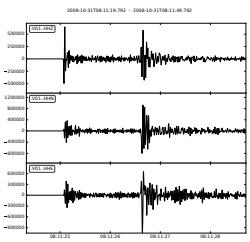

Fig. 2: Example event of the source array, recorded at station V01 (88004906 - 2008-10-31 08:11:22.890, M 1.4). High-pass filterd (1 Hz).

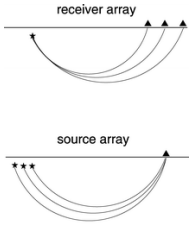


Fig. 3: Sketch of Source and Receiver Array (Rost & Thomas, 2002).

## Source Arrays

Source arrays consist of spatially clustered earthquakes recorded by one receiver station.
Following the reciprocity of the Green's function (Spudich and Bostwick, 1987), source arrays can be analysed similar to receiver arrays:

Precisely known origin times and hypocentral locations as well as resembling waveforms are required to perform beam forming.

$$\dot{\vec{U}}_m(\vec{o},t) := M_0^{-1} \cdot \mu(\vec{f}_0) \cdot \dot{\vec{u}}_m = \vec{d} \cdot T^m(\vec{f}_0,t;\vec{o},0)$$

observer location; normalized by seismic moment; point dislocation at position $f_0$; ground velocity time series; traction experienced at $f_0$ on the fault when a point source is applied at the observer location o

## Set-up of a shallow source array

22 events of the recorded earthquake swarm were selected based on their interevent distance, the data quality and their waveform resemblance to set up a source array. Although aiming for a 3-D array, the resolution of the source array is clearly limited in E-W, because the events occur on a well-defined fault plane.

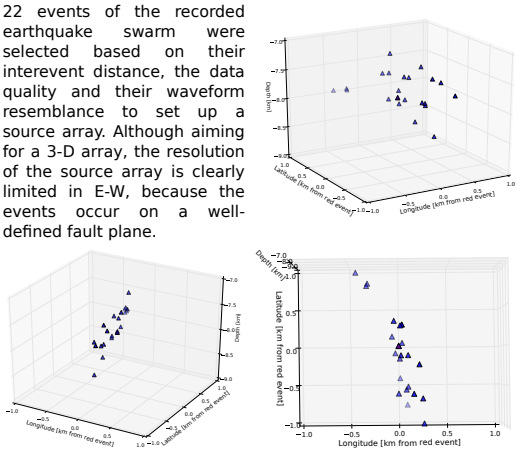


Fig. 4: Source array in three perspectives. The elongated shape results in a limited E-W resolution.

## Source array analysis methods

A time domain source array beam forming method was developed assuming a fictional plane wave travelling from the receiver station to the source array.
Aditionally two methods for the localization of reflection/ conversion points were implemented: An analytical method using a homogeneous velocity along the entrire travel path and a grid search method in which for every grid point in a 3-D volume between the sources and the receiver stations the travel and shift times are calculated using a 1-D velocity model.

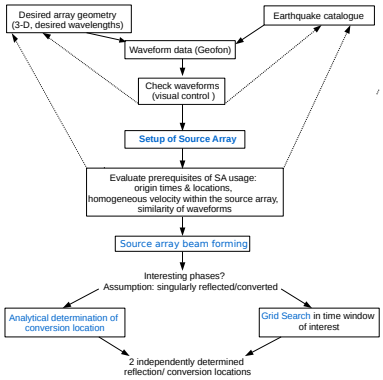


Fig. 5: Workflow of the entire source array beam forming concept.

## Waveform resemblance

To perform source array beam forming similar waveforms are required. Cross-correlation coefficients were calculated for all event pairs and all receiver stations. We observe that the different events recorded at a single station generally show greater resemblances than the recordings of one event at all stations of the receiver array. This indicates a heterogeneous subsurface beneath the receiver array with respect to the resolved frequencies.

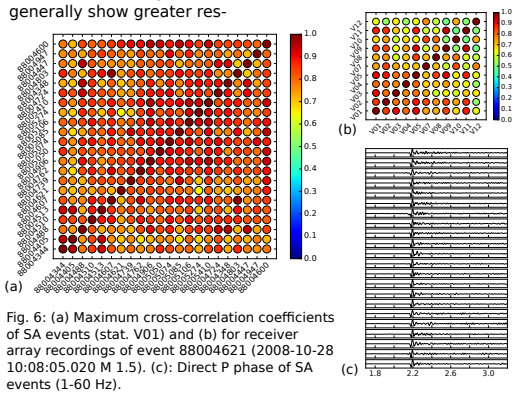


Fig. 6: (a) Maximum cross-correlation coefficients of SA events (stat. V01) and (b) for receiver array recordings of event 88004621 (2008-10-28 10:08:05.020 M 1.5). (c): Direct P phase of SA events (1-60 Hz).

## Beam forming results: shallow SA

Source array beam forming was performed on vertical and horizontal component records of all 11 stations of the Rohrbach array. The stacks are clearly improved by alignment with respect to the P phase maximum amplitude. The direct P phase is very distinct on the vertical component, while the S phase is strongest on E component. On E component, a presumable PS converted phase from about 0.6-0.8 km depth is observed as well as a phase arriving shortly before the direct S phase.

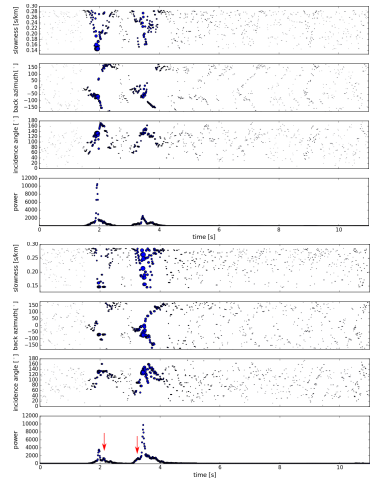


Fig. 7: Beam forming results, shallow SA. (a) HHZ, (b) HHE component.

## Beam forming results: deep SA

A second source array consisting of deeper events was set-up to analyse a structural phase described by Hiemer (2009) and Hrubcová et al. (2016). Beam forming was performed on vertical component records, on which the structural phase is observed about 0.85 s after the direct P phase travelling with P slowness through the source array. The analytical localisation method indicates a reflection in 10.7 km depth, 5.4 km south and 4.8 km west of the source array. The grid search points to a reflector 7 km west and 4.8 km south of the source array in only 4.5 km depth. The grid search method shows that while the latitude of the reflector is well resolved, the longitude and depth are less distinct.
One question remains: Why are the structural phases observed only on recordes of events deeper than 9 km?

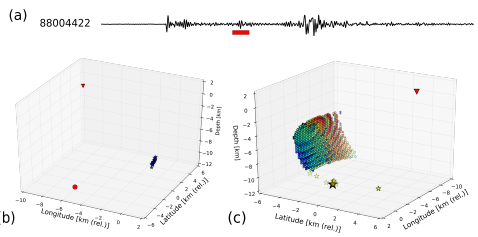


Fig. 8: (a) Example event of deep SA with structural phase arriving 0.85 s after direct P phase. (b) Analytically determined reflector position (red circle) along with stat. V01 (red triangle) and SA events (blue stars). (c) Grid Search result. Power stacks calculated for all travel paths arriving 0.6 to 1.0 s after the direct P phase, grid spacing 250 m. Results with > 50 % power shown.

## Conclusions

- **The waveform resemblance of the SA events recorded at one RA station is higher than the resemblance of single events recorded at all Rohrbach array stations.**
- **The distinct beamforming results along with the waveform resemblence reveal the opportunities of using source arrays consisting of small swarm events for the analysis of crustal structures.**
- **PS conversion in about 0.6 - 0.8 km depth**
- **Structural phase on deep events (PP) traveling south-west of the virtual line between SA and RA**

References:

Seism. data: Roessler et al. (2008): Rohrbach/Vogtland Seismic Array 2008, Univ. Potsdam. GFZ. doi: 10.14470/1N934013.
Fischer, T., Horálek, J., Hrubcová, P., Vavryčuk, V., Bräuer, K., and Kämpf, H. (2014). Intra-continental earthquake swarms in West-Bohemia and Vogtland: A review. Tectonophysics, 611:1–27.
Hiemer, S. (2009). Arrayseismologische und statistische Auswertung des Erdbebenschwarms aus dem Jahr 2008 im Vogtland/NW-Böhmen. PhD thesis, Universität Potsdam.
Hrubcová, P., Vavryčuk, V., Boušková, A., and Bohnhoff, M. (2016). Shallow crustal discontinuities inferred from waveforms of microearthquakes: Method and application to KTB Drill Site and West Bohemia Swarm Area. J Geophys Res: Solid Earth, 121:881–902.
Spudich, P. and Bostwick, T. (1987). Studies of the Seismic Coda Using an Earthquake Cluster as a Deeply Buried Seismograph Array. J Geophys Res: Solid Earth, 92(B10):10526–10546.

AG Seismologie
Jahrestagung,
Sept. 2017